Freie Universität Berlin

Thesis

Rupture Propagation Imaging Across Scales: from Large Earthquakes to Microseismic Events

Vorgelegt von:
Jonas T. Folesky

Dissertation
zur Erlangung des akademischen Grades
Doktor der Naturwissenschaften

Fachbereich Geowissenschaften
Freie Universität Berlin

Berlin
2018

Erstgutachter: Prof. Dr. Serge A. Shapiro
Zweitgutachter: Prof. Dr. Frederik Tilmann

Tag der Disputation: 25.10.2018

„Das Studium und allgemein das Streben nach Wahrheit und Schönheit ist ein Gebiet, auf dem wir das ganze Leben lang Kinder bleiben dürfen.“

Albert Einstein

Summary

Imaging of the rupture process of an earthquake produces valuable insights on the kinematics of earthquakes. In earthquake seismology rupture propagation imaging has been applied impressively to many megathrust events to visualize the rupture process and path. This can help to comprehend the cascade of processes within an ongoing earthquake and consequently it may help to improve hazard mitigation measures. As the coverage of seismic stations and the quality of the instruments has been increasing rapidly in the last years, there is a growing potential to apply similar imaging approaches to medium-sized and small earthquakes, too.

In this thesis, I implement and apply three different rupture imaging techniques to infer rupture properties from events at local and at microseismic scales covering magnitudes of $1 \lesssim M \lesssim 8$: the back projection imaging, the empirical Green's function analysis, and the P wave polarization stacking. I examine two different data sets: the fluid-induced microseismicity from the enhanced geothermal system in Basel, 2006, and the natural occurring seismicity in the vicinity of the rupture area of the 2014 M_W8.1 Iquique earthquake in northern Chile.

In a first study, I carefully adjust, numerically test, and apply the back projection technique in the microseismic reservoir at the Basel EGS. The results demonstrate for the first time that back projection imaging is capable of illuminating the rupture process at scales where events have rupture lengths of only a few hundred meters. To complement this study, I perform a second study based on empirical Green's function analysis in combination with directivity measurements for the smaller magnitude events at this site to estimate corresponding rupture orientations and directions. Based on the combination of the two imaging approaches, I find valuable results for a larger amount of events which cover a broader spectrum of magnitudes compared to a single method approach. The combined results indicate that the rupture behavior at the Basel reservoir appears to be magnitude-dependent and it is strongly influenced by the induced pressure-field from the injection.

At the northern Chilean subduction zone, numerous foreshocks and aftershocks of the 2014 M_W8.1 Iquique event were recorded by the Integrated Plate boundary Observatory Chile, which I use to perform P wave polarization stacking to find rupture orientations of $5 \leq M \leq 8$ events. Although applied to huge teleseismic events before, this is the first successful application of this technique at local scale. My estimated directions are in good agreement with independent back projection studies for the Iquique event itself and its largest foreshock and aftershock. In a second study, I apply empirical Green's function analysis at the same site for events with $2.6 \leq M \leq 5.3$. Again, the combination of the results of the two methods yields important findings: the distribution of orientations of rupture directions shows a preferred direction towards east, which is the

down-dip direction. It is less sharp for the larger magnitude events and it led to the hypothesis that a bimaterial effect at the plate interface could be responsible for the observed preferred rupture direction. The effect appears to be stronger pronounced for smaller events which are not capable to overcome the barriers of the asperity of their nucleation.

In this thesis, three rupture propagation imaging approaches were adjusted in a way that it became possible to analyze events of significantly smaller scale than previously feasible. This thesis shows that the integration of multiple imaging approaches can produce enhanced results for the same data set and how to achieve them. For the further study of the physics of earthquake rupture processes, we need more comprehensive data on the rupture behavior.

Zusammenfassung

Das Abbilden des Bruchprozesses eines Erdbebens liefert wertvolle Erkenntnisse über den charakteristischen Verlauf des Erdbebens und somit auch der diesem zu Grunde liegenden Physik. In der Seismologie wurden hierfür geeignete Abblidungsverfahren bereits mehrfach bei Megathrust-Erdbeben angewandt, um deren teils lang anhaltende und komplizierte Bruchprozesse zu visualisieren. Dadurch wird es möglich die ablaufenden Prozesse besser zu verstehen und daraus Erkenntnisse zu gewinnen, die u.a. bei Gefährdungsstudien und daraus ableitbaren Maßnahmen angewandt werden können. Mit der Verbesserung von Abdeckung und Anzahl seismischer Stationen und deren Qualität besteht inzwischen das Potential ähnliche bildgebende Verfahren auch auf mittelgroße und kleine Erdbeben zu übertragen.

In dieser Arbeit betrachte ich drei verschiedene Abbildungsverfahren zur Visualisierung von Bruchprozessen lokaler und mikroseismischer Ereignisse, welche Magnituden in Größenordnungen von $1 \lesssim M \lesssim 8$ aufweisen. Die angewandten Verfahren sind das „back projection imaging“, die „empirical Green's function analysis“ und das „P wave polarization stacking“. Ich untersuche zwei verschiedene Datensätze: Fluid-induzierte Seismizität des Basel-1 EGS von 2006 sowie natürlich vorkommende Seismizität einer Subduktionszone in der Umgebung des Bruchgebietes des 2014 M_W 8.1 Iquique Erdbebens in Nordchile.

In der ersten Teilstudie dieser Arbeit nutze ich die back projection imaging Technik, welche zunächst sorgfältig angepasst und numerisch getestet wird, um die größten Ereignisse des Datensatzes des Basel EGS abzubilden. Hierdurch weise ich erstmals nach, dass dieses Verfahren geeignet ist Bruchprozesse mit einer Länge von nur wenigen hundert Metern abzubilden. Als komplementäres Verfahren wird in einer weiteren Studie die empirical Green's function Technik genutzt in Kombination mit Directivity Effekt Messungen, um eine Vielzahl kleinerer Ereignisse aus dem gleichen Datensatz auf ihre Bruchrichtungen hin zu untersuchen. Die kombinierten Ergebnisse beider Studien zeigen, dass in Basel das Bruchverhalten magnitudenabhängig erscheint und stark beeinflusst ist durch den Überdruck, der aus der Injektion resultiert.

Am Integrated Plate boundary Observatory Chile wurden die Vor- und Nachbebenserien des großen 2014 M_W 8.1 Iquique Erdbebens in der nordchilenischen Subduktionszone aufgezeichnet. Mit diesen Daten führe ich ein P wave polarization stacking zum Auffinden von Bruchorientierungen von Beben mit Magnituden $5 \leq M \leq 8$ durch. Diese Technik wird hier erstmals mit einem Stationsnetzwerk in lokaler Distanz zu den auftretenden Beben verwendet. Die abgeschätzen Bruchrichtungen für das Iquiue Beben sowie für dessen größtes Vor- und Nachbeben sind in guter Übereinstimmung mit Ergebnissen aus unabhängigen back projection imaging Studien. In einer weiteren Studie nutze ich die empirical Green's function Technik zur Untersuchung von Beben der Stärke $2.6 \leq M \leq 5.3$ im selben Gebiet. Wieder zeigt sich, dass die Kombination zweier Abbildungsverfahren

wesentliche Beobachtungen ermöglicht: Die Verteilung der Orientierungen der Bruchrichtungen zeigt eine Vorzugsrichtung nach Osten in beiden Studien. Dies ist gleichzeitig die Konvergenzrichtung der Platten und die Abwärtsrichtung entlang des Slabs. Die Verteilung ist weniger scharf für größere Ereignisse, was zu folgender Hypothese führte: Ein Effekt des Materialkontrasts an der Plattengrenze könnte verantwortlich sein für die beobachtete bevorzugte Bruchrichtung. Diese erscheint gerade bei kleineren Ereignissen stärker ausgeprägt, was bedeuten könnte, dass deren Brucheigenschaften nicht das Potential bergen die Ränder ihres Nukleationsgbietes zu überwinden.

In dieser Dissertation werden drei Abbildungsverfahren für Bruchprozesse von Erbeben vorgestellt und derart überarbeitet und angewandt, dass sie für Erdbeben deutlich kleinerer Magnitude als bisher üblich verwendbar werden. Die Dissertation zeigt, dass die Integration mehrerer unabhängiger bildgebender Verfahren zu einer deutlichen Verbesserung der Ergebnisse führen kann und sie erklärt, wie dies durchgeführt wurde. Für eine vertiefte Analyse der Physik der Bruchprozesse von Erdeben bedarf es noch vieler weitergehender Studien, welche sich mit Bruchverhalten von Erbeben unter verschiedenen geologischen Bedingungen beschäftigen.

Contents

Chapter 1

Introduction

Seismic sources are complex and still not fully understood. When characterizing an earthquake source commonly the magnitude and the moment tensor are estimated. These are very important quantities, however, they do not describe the kinematic of the earthquake rupture process. In the case of a large event size or a nearby observation system, the kinematic can be resolved with rupture propagation imaging, which can lead to an improved picture of the rupture history and consequently to more precise hazard potential estimates for similar events. Therefore, techniques to assess the rupture propagation characteristics are relevant.

A detailed characterization of the rupture process has become standard for huge earthquakes from the last decades, e.g., Sumatra 2004, Maule 2010, Tohoku 2011, Iquique 2014, and many more. The study of the rupture processes of such earthquakes was one important aspect for the development and installation of early warning systems for the sometimes triggered tsunamis in many regions of the world. Also, building regulations could be significantly improved when the rupture origin, rupture direction, fault parameters, and the corresponding expectable ground movement were known or could be predicted with increasing accuracy. This is also true for medium-sized earthquakes which can be similarly disastrous. In the future, when such measures are taken, the ground motion of events as, for example, the 2009 L'Aquila, 2012 Emilia, or the 2016 Amatrice and Norcia earthquakes in Italy could be predicted more precisely and damage could be reduced.

In addition to natural seismicity, small to medium-sized events recently increased in frequency in man-made georeservoirs, such as geothermal reservoirs, waste water disposal sites, CO_2 - sequestration, mines, or gas and oil fields. For such reservoirs it is absolutely necessary to better understand the conditions and mitigate the possibility of large events, especially if - and this sometimes is the case - the reservoir is located relatively

close to a village, town or city. To date there exist several examples of up to medium-sized ($3 < M < 5$) induced events for each of the types of reservoirs mentioned above. This shows the necessity of developing techniques to analyze the rupture processes of these events.

In this work, three different rupture tracking techniques are applied at two different sites, a geothermal reservoir and a subduction zone, to demonstrate and discuss the feasibility of these tracking approaches in different settings. For every site, there exist a number of dependencies and challenges which need to be addressed and which predetermine the usage of respective imaging methods. Depending on the approach, several rupture features can be illuminated. The rupture imaging procedures in use can be applied to single or multiple events simultaneously. This allows to analyze and interpret single event occurrences and rupture histories and it provides the possibility to combine and compare these findings with those of other events from the same site. In some cases, this leads to important observations concerning rupture nucleation, locations, or rupture directions and their circumstances.

In Chapter 2, a short theoretical introduction to the three rupture imaging techniques applied in this work is given. First, it is demonstrated that propagating ruptures, especially if the rupture mode is unilateral, show signs of directivity in their waveforms and correspondingly in their spectra. Although not easily recoverable, these signatures are the basis of the rupture tracking approaches. Then each technique is introduced and the core ideas and application criteria of the methods are outlined. As the theoretical background for the three approaches was not developed by the author of this thesis, the explanations are kept as short as necessary in order to be able to fully follow the application studies in Chapters 3-6.

The first study is presented in Chapter 3, where the back projection technique is applied to the largest events that occurred at the enhanced geothermal system in Basel 2006. The back projection technique has been developed for the usage in global seismology and was previously applied to data from tectonic megathrust earthquakes. Based on simulated event data, this chapter demonstrates that with a suitable station geometry, a few stations with good azimuthal coverage are sufficient to image earthquakes in microseismic reservoirs, even when they show rupture lengths of only a few hundred meters. In the next step, four events with magnitudes $M_L \gtrsim 3$ are imaged with the back projection approach. This is the first application of back projection imaging to events of such small magnitudes.

The back projection technique is essentially an amplitude stacking approach where the seismograms are back-projected to the original source. In case of the Basel enhanced geothermal system, this is limited to events with $M_L>3$. Consequently, another approach has to be used in order to estimate rupture properties of the smaller events. One alternative is the application of empirical Green's function analysis to compute relative

source time functions and analyze the imprint of the source intrinsic directivity effect on them. This is done in Chapter 4, where rupture directivity estimates for about 200 microseismic events with $1<M_L<3$ are computed. This work makes clear that the signatures of the rupture process, i.e., the rupture directivity and the approximate rupture velocity can be estimated at theses scales, too, and could be considered when characterizing such events, even if they are small. Also, a pattern in the orientation of rupture directivity within the catalog of analyzed events is found. In the vicinity of the injection source, events appear to be randomly oriented and with an increasing distance ruptures are aligned with the overall structure, which is illuminated by the microseismic cloud. Essentially, this work shows that the largest events at this site nucleate at the rim of the reservoir and rupture - in opposition to the prevailing trend of the majority of event directions - toward the injection source. This is a combined result from the outcome of both studies in Chapters 3 and 4.

In Chapter 5, a third technique of rupture imaging is realized, which is the precise measurement of the change of P wave polarization over the P wave train. This is performed for natural seismicity data in the northern Chile subduction zone. The data set was recorded at the Integrated Plate boundary Observatory Chile (IPOC) network and the study region is limited to the rupture area of the 2014 M_W 8.1 Iquique event where a vast number of precursor events and aftershocks occurred. For this work, events with magnitudes $M_L \gtrsim 5$ are analyzed. The minimum magnitude is necessary since this purely geometrical stacking scheme is feasible only for a certain minimum opening angle which depends on the rupture length, rupture orientation, and on the epicentral distance. For 60 events, including the mainshock and largest foreshock and aftershock, the rupture paths are reconstructed and a preferred rupture direction toward east, i.e., down-dip, and southeast is found.

The very rich data set obtained at the IPOC network also gives the opportunity to apply the empirical Green's function approach that was outlined in Chapter 4 to events from the subduction zone in northern Chile. Within this subduction zone, many repeating earthquake families were detected and could then be used for empirical Green's function analysis. This is described in Chapter 6. For 351 EGF-event pairs rupture directions are found. Solutions are produced for events within a magnitude range of $2.6<M_L<5.3$. Almost all of the events show the same rupture directivity orientation. The ruptures are preferably directed down-dip, parallel to the direction of the convergence vector of the Nazca and the South-American plate which is the east-northeast direction. The results are interpreted in comparison to those of Chapter 5 and a strong influence of the repeater-like nature of the used events is deduced.

In the final Chapter a short summary of the results from Chapters 3-6 is given and an outlook to further work is outlined.

Chapter 2

Earthquake Rupture Propagation Imaging

The earthquake rupture is a highly complex process which has attracted geophysicists for more than 50 years. Nowadays a number of different fields of research exists that deal with different aspects of the subject, ranging from laboratory experiments to in situ fault drilling experiments, synthetic and analogue rupture modeling, and also rupture imaging.

The earliest studies that included the propagation aspect of an earthquake rupture were kinematic finite source models by Ben-Menahem [1961, 1962], Maruyama [1963], Burridge and Knopoff [1964], Haskell [1964, 1966] from which Haskell's model became the most influential for the following decades. These models constitute attempts to derive the displacement recorded at an arbitrary point in space and time in the near and far field for different wave types. All models include kinematic spreading of a displacement discontinuity, which is slip or a dislocation along a fault plane.

For unilateral rupture the most widely used model is Haskell's line source model which assumes an uniform displacement discontinuity that spreads at a constant velocity unidirectionally along a rectangular-shaped fault. This is a reasonable approximation for events of long wavelengths compared to their fault size. The line of dislocation (displacement) at $t = 0$ of a width W propagates along the fault at a constant speed v_r until a region of a length L is broken. Following the dislocation, a zone of constant slip D is created. The slip function on a plane can be expressed as given in the review by Madariaga [2007],

$$\Delta\dot{u}_x(x, y, t) = D\dot{s}(t - x/v_r)H(x)H(L - x), \tag{2.1}$$

for $-W/2 < y < W/2$, where $\dot{s}$ is the slip rate function, H is the Heaviside function. This model implicitly contains the propagation of the rupture in the time delay term x/v_r. Despite non-physical features like the non-propagation toward the y-direction and the slip jump at the model boundaries which violate continuum mechanics, the model is a first order approximation to seismic slip, fault finiteness and finite rupture speed from which the seismic moment can be computed as $M_0 = \mu DLW$, where μ is the shear modulus. The displacement field can be expressed using the far field approximation of a point source:

$$u_c(\overline{x}, t) = \frac{1}{4\pi\rho c^3}\frac{\mathcal{R}_c(\theta,\phi)}{R}\Omega(t - R/c), \tag{2.2}$$

where $R = |\overline{x} - \overline{x}_0|$ is the distance from the source to the observer, c is a place holder for either v_p or v_s for P or S waves and $\mathcal{R}_c$ is the term describing the radiation pattern, a function of the takeoff angle of the ray at the source. To introduce a finite source in time and space rather than a point source, the new source time function reads

$$\Omega(\theta,\phi,t) = \mu\int_0^t\int_{S_{x_0}} \Delta\dot{u}_j(x,y,t-\tau+\frac{\overline{e}_r\cdot\overline{x}}{c})n_k\mathrm{d}x\mathrm{d}y\mathrm{d}\tau, \tag{2.3}$$

where $\overline{x} = (x, y)$ is a position on the fault with respect to the hypocenter, $\overline{n}$ is the normal to the fault and S is the broken area. The integral's value now depends on the radiation direction due to the term $\overline{e}_r \cdot \overline{x}$, creating the so-called directivity effect. For the Haskell model, the slip function $\Delta\dot{u}$ is replaced and one obtains

$$\Omega(\theta,\phi,t) = \mu\int_{-W/2}^{W/2}\mathrm{d}y\int_0^L D\dot{s}(t-\frac{x}{v_r}+\frac{x}{c}\cos\phi\sin\theta+\frac{y}{c}\sin\phi\sin\theta)\mathrm{d}x. \tag{2.4}$$

Evaluating this for an observer situated along the fault axis with $\phi = 0$, one obtains

$$\Omega(\theta,0,t) = M_0\frac{1}{T_M}\int_0^{min(t,T_M)}\dot{s}(t-\tau)\mathrm{d}\tau, \tag{2.5}$$

with $T_M = \frac{L}{v_r}(1 - \frac{v_r}{c}\sin\theta)$, an integral over time of the source slip rate function. In other directions, the source time function is more complex, but it can be computed by the method of isochrones; see Madariaga [2007]. Using this model, one finds two fundamental properties of the associated seismic radiation: the finite duration of the rupture is given by T_M, and directivity, i.e., the duration and amplitude of seismic waves depend on the azimuthal angle of radiation. Also, the magnitude of the effect depends on the ratio of rupture velocity to the velocity of the given wave type.

These two parameters, directivity and rupture velocity are the most simple expansion of the point source model, when moving to more realistic earthquake source descriptions. Even when assumed constant they are usually not easily observable or even extractable from real waveform data due to the more pronounced effects of source radiation pattern,

ray path, and instrument response. Both parameters, however, are important components when progressing toward a more thorough earthquake rupture understanding.

In recent years this has become increasingly clearer and research on source directivity of earthquakes from different fields has been performed. Not only large megathrust events have been imaged, to illuminate their rupture histories, but also other events are analyzed for directivity as, e.g., deep focus earthquakes in Park and Ishii [2015]. Recently, also smaller events have come into focus. For instance Kaneko and Shearer [2014, 2015] show the variability of seismic source spectra, stress-drop, and radiated energy in dependence of different source models. These models include circular and elliptic fault shapes and symmetric and asymmetric activation of these faults, while rupture speed remains constant. The obtained spectra show for some cases azimuth dependent variations of corner frequencies resulting in stress-drop differences up to a factor of 8. The study emphasizes that knowledge on the rupture behavior is highly useful when interpreting event properties obtained from spectral analysis. Boatwright [2007] shows that this is valid for large seismic events as well as for small events.

For the estimation of earthquake rupture properties multiple different techniques are available. In this work only direct imaging methods are considered, i.e., I use techniques that are applied directly to the seismic data with a minimum necessity of a priori knowledge of the rupture nature or rupture conditions at the sites. This excludes indirect methods that require source inversion or forward rupture modeling, which are important and powerful techniques to isolate and understand rupture features, however, they often require a suite of assumptions for being applicable besides their computationally advanced requirements. In the following sections the three imaging approaches will be introduced which are applied in the subsequent chapters. As the theory for these imaging approaches is already described thoroughly elsewhere, I outline the idea and functionality for each technique as far as it is needed to complement the application studies in the Chapter 3–6.

2.1 Back Projection Imaging

The idea of back-projecting radiated seismic energy obtained at an array or a network of stations back to the source of radiation was introduced by Spudich and Cranswick [1984] and Ellsworth [1992]. It was extended and impressively applied at the 2004 M_W9.1 Sumatra megathrust event by Ishii et al. [2005, 2007] and Krüger and Ohrnberger [2005]. Since then it has been applied to multiple large earthquakes [e.g., Kiser and Ishii, 2011]. The technique is basically a simplified reverse time migration scheme, where theoretical travel times between a potential source grid and the seismic stations are computed in

order to correct and stack the received seismograms such that a coherent stack is achieved only at the source location.

Mathematically, the seismograms $u_k(t)$ recorded at n receivers are stacked for every ith potential source grid point, corrected by the independently obtained source-receiver travel time, i.e., for the P wave the stacking scheme reads

$$s_i(t) = \sum_{k=1}^{n} \omega_k |u_k(t + t^p_{ik} + \delta t^p_k)|, \tag{2.6}$$

where $s_i(t)$ is the stack at the ith source grid point, ω_k is a possible station specific weighting factor at the kth station and t^p_{ik} is the predicted P wave travel time between the ith potential grid point location to the kth receiver location. δt^p_k is an additional time shift that corrects for the unmodeled velocity perturbations along the ray path to receiver k such as, e.g., station terms. When performing the stacking procedure for all possible source points and time steps, a seismogram-like trace for every grid point is obtained, containing the stacked values for each time step. Simultaneously the spatial distribution of stacks of back-shifted amplitudes for each time step are obtained. The squared amplitudes of the stack (s_i^2) can be used as a seismic energy proxy, referred to as brightness. For an unilateral rupture ideally a well defined maximum of brightness is expected for each time step, which is considered to be the rupture front at one specific point in time. The peak migrates in time as the rupture progresses. In this way, the brightness distribution potentially provides estimates for the rupture path, i.e., the direction, length, duration, and speed. Also, with a well defined imaging criterion the rupture area can be approximated [Ishii et al., 2005].

Back projection imaging has been applied to most large events of the recent years and it has been performed by many groups. Examples are the 2010 M_W8.8 Maule earthquake [Kiser and Ishii, 2011], the 2011 M_W9.0 Tohoku earthquake [Kiser and Ishii, 2012], the 2014 M_W Iquique earthquake [Schurr et al., 2014] including its largest foreshock and aftershocks [Meng et al., 2015], just to name some.

The technique has been refined by different authors introducing, e.g., the stacking of multiple seismic phases simultaneously [Kiser et al., 2011] or the additional limitation to specific frequency bands [Meng et al., 2012] combined with a special weighting approach, both in order to enhance resolution and mitigate the swimming artifact, the fact, that the migration of the back-projected images are biased by the station geometry of the observer network and its location.

Today applications range from teleseismic, to regional, to local , and even to microseismic scale. The exact specifications and preconditions for an application in a micro-seismic

reservoir are elaborated further in Chapter 3 for the example of the Basel-1 enhanced geothermal system.

2.2 Empirical Green's Functions

In the last decades empirical Green's functions (EGFs) have been increasingly used for example in attenuation studies, ground motion studies, rupture modeling, and source studies. In the seismological context the Green's function constitutes the impulse response of the medium which is generally not exactly known. One way to approximate this response function for a given location-receiver-pair is the empirical Green's function. For this usually the recorded waveforms of one or more smaller earthquakes are used which are colocated to the larger earthquake that is being analyzed. Included in a seismic record are generally information on the earthquake source, the ray path, the station site response and the instrument itself. In the framework of source studies, the EGF is that part of the recorded seismogram which has to be removed in order to obtain a clear record of the source time function, i.e., the EGF resembles the other prior mentioned aspects. Although the Green's function could be modeled, the EGF method more accurately covers those parts of the medium response that require a high frequency resolution. In seismology this would be crustal features, structures, or heterogeneities imprinted especially in the high frequency part ($> 1\,Hz$) of the seismogram. The EGF is, however, not a perfect impulse response but includes a contribution of the source time function of the small event, i.e., the EGF has to satisfy the criterion of being valid for the frequency range of interest. That is, the spectrum of an EGF for a given earthquake has to have a flat displacement spectrum for the entire frequency range where it is applied, i.e., the EGF is only valid below its own corner frequency.

The so called EGF method was theoretically described in many publications [e.g., Hutchings and Viegas, 2012]. We recall the derivation from Vallée [2004], who starts with the fundamental representation relation [Aki and Richards, 2002], which expresses the displacement of an earthquake originating from a displacement discontinuity across an internal surface. The spectral displacement $\mathrm{U}_i(\overline{x},\omega)$ reads

$$U_i(\overline{x},\omega) = \iint_S m_{pq}(\overline{\xi},\omega) G_{ip,q}(\overline{x},\overline{\xi},\omega) d^2\xi, \tag{2.7}$$

where $m_{pq}(\overline{\xi},\omega)$ is the moment tensor density and $G_{ip,q}(\overline{x},\overline{\xi},\omega)$ is the spatial derivative of the Green's function. When ξ_0 is the hypocenter location and G_{ip} is equal for all points of the fault except for a phase shift $(\overline{k}\cdot(\overline{\xi}-\overline{\xi}_0))$ due to the variation of distance between source and receiver, one can reformulate to

$$U_i(\overline{x},\omega) = -ik_q G_{ip}(\overline{x},\overline{\xi}_0,\omega)\iint_S m_{pq}(\overline{\xi},\omega)e^{-i\overline{k}\cdot(\overline{\xi}-\overline{\xi}_0)}d^2\xi. \tag{2.8}$$

For an equal time dependence, i.e., a constant mechanism along the fault, one can simplify

$$m_{pq}(\overline{\xi},\omega) = M_0\hat{M}f(\overline{\xi},\omega) \tag{2.9}$$

where M_0 is the seismic moment, $\hat{M}$ is a unit tensor independent of $\overline{\xi}$ and ω, and $f(\overline{\xi},t)$ (the Fourier inverse of $f(\overline{\xi},\omega)$) is a causal, positive scalar function, monotonically increasing over $[0,\tau_r]$ and constant elsewhere, where τ_r is the duration of the dislocation process. With the use of M_0 we imply the following property for $\dot{f}: \int_\infty^\infty \iint_S \dot{f}(\overline{\xi},t)d^2\xi dt = 1$. For a given earthquake (1) with a moment M_0^1 it is then possible to write

$$U_i^1(\overline{x},\omega) = -M_0^1\hat{M}ik_q G_{ip}(\overline{x},\overline{\xi}_0,\omega)\iint_S f(\overline{\xi},\omega)e^{-i\overline{k}\cdot(\overline{\xi}-\overline{\xi}_0)}d^2\xi. \tag{2.10}$$

If at the same location a smaller event (0) of moment M_0^0 and similar mechanism can be found, one can approximate

$$f(\overline{\xi},\omega) = \delta(\overline{\xi}-\overline{\xi}_0)H(\omega) = \frac{\delta(\overline{\xi}-\overline{\xi}_0)}{i\omega}, \tag{2.11}$$

with $H(\omega)$ being the Fourier transform of the Heaviside function ($H(t)$) for $\omega > 0$, resulting in

$$U_i^0(\overline{x},\omega) = -\frac{M_0^0}{i\omega}\hat{M}ik_q G_{ip}(\overline{x},\overline{\xi}_0,\omega). \tag{2.12}$$

It is therefore possible to obtain the so called relative source time function (RSTF) S' of the larger event by deconvolution:

$$S'(\omega) = \frac{M_0^1}{M_0^0}i\omega\iint_S f(\overline{\xi},\omega)e^{-i\overline{k}\cdot(\overline{\xi}-\overline{\xi}_0)}d^2\xi \tag{2.13}$$

or with $\overline{k} = \frac{\omega}{c}\overline{u}$, with c being the phase velocity and $\overline{u}$ as the wave propagation direction, written in the time domain it reads

$$s'(t) = \frac{M_0^1}{M_0^0}\iint_S \dot{f}(\overline{\xi},t-\overline{u}\cdot(\overline{\xi}-\overline{\xi}_0)/c)d^2\xi. \tag{2.14}$$

For the validity of this equations it is important to recall that the second earthquake (the EGF-event) has to be smaller than the first, such that one can assume a step function for $f(\overline{\xi}, t)$. Also the mechanism of the event pair must be the same, and the main event must have a constant mechanism for the entire rupture area.

The above, mathematically exact considerations can be accompanied by the following, but less precise description of the problem, which nevertheless is often stressed (as in Mueller [1985], Li et al. [1995], Jost et al. [1998]) as it is instructively describes the EGF method in a comprehensive way. In general each seismogram can be expressed as a convolution of four contributions:

$$u(t) = s(t) * p(t) * r(t) * i(t), \tag{2.15}$$

where $u(t)$ is the recorded seismogram, $s(t)$ is the source time function, $p(t)$ is the impulse response of the path, $r(t)$ is the influence of the recording site, and $i(t)$ is the instrument response. Comparing this to equation 2.10 we see that $G = p(t) * r(t) * i(t)$ and the remaining terms resemble the source time function of the larger event. For the smaller event we have equation 2.12, where only a constant remains, which equals a delta pulse in the time domain. This means here, the source time function can be expressed as $s(t) \approx \delta(t)$ (which is equal to a Heaviside function for $t > 0$). Then the spectrum of the smaller event $U^0(\omega)$ is deconvolved from the spectrum of the larger event $U^1(\omega)$ to obtain the relative source time function.

$$\frac{|U^1(\omega)|}{|U^0(\omega)|} \approx \frac{|S(\omega) \cdot P(\omega) \cdot R(\omega) \cdot I(\omega)|}{|\delta(\omega) \cdot P(\omega) \cdot R(\omega) \cdot I(\omega)|} = \frac{|S(\omega)|}{|\delta(\omega)|} = |S'(\omega)|, \tag{2.16}$$

where $U^0(\omega)$ is the EGF spectrum, $S(\omega)$ is the source time function of the large event, $\delta(\omega) = const$ is the source time function of the EGF, and $S'(\omega)$ is the RSTF. Note that according to equation 2.14 the scaling factor is M_0^1/M_0^0 since $\int\int_S \dot{f} d^2\xi dt = 1$.

Although the obtained RSTFs do not depend on radiation pattern and mechanism of the events anymore they are still affected by source directivity, which is the fact that for a propagating rupture the RSTF exhibits variations of amplitudes and duration as a function of the rupture-receiver geometry. Savage [1965] explicitly described the influence of directivity on seismic phases and derived the following formula

$$F = \frac{A}{K} = \frac{i \cdot v_r}{1 - (v_r/c)^i \cdot cos^i(\phi - \phi_0) \cdot sin^i(\theta - \theta_0)}, \tag{2.17}$$

where F describes the variation of the expected amplitude A at a given station, scaled by an unknown constant K. v_r is the rupture velocity and c is the phase velocity, respectively. ϕ is the station azimuth relative to the hypocenter and θ is the station plunge. ϕ_0 is the azimuthal orientation of the rupture plane and θ_0 describes the tilt

of the rupture direction inside that rupture plane. The formula describes unilateral ruptures for $i = 1$ and bilateral ruptures for $i = 2$. A similar expression is given for the modulation of the source duration

$$T = \frac{L}{i \cdot v_r} \cdot (1 - (v_r/c)^i \cdot cos^i(\phi - \phi_0) \cdot sin^i(\theta - \theta_0)), \tag{2.18}$$

which additionally includes the parameter T and L are the apparent rupture duration and the rupture length, respectively. Thus, it is theoretically possible to reconstruct rupture direction, rupture speed, length, and duration for a given event using the EGF approach, if there is a sufficient number of measurements for a given event. That is why the EGF method is considered as an important tool to observe rupture properties in this work. In principle it is applicable to very small events as long as suitable empirical Green's functions - even smaller events - can be found, that fulfill the upper mentioned criteria. This simultaneously limits the EGF method to those events where indeed EGFs exist.

The capability of the EGF approach to compute rupture directions of small events is exploited in the two studies presented in Chapter 4 and Chapter 6, where the EGF technique gives reliable results for multiple events with magnitudes below the applicability threshold of the back projection technique and the P wave polarization stacking.

2.3 P wave Polarization Stacking

The idea of P wave polarization stacking is simple: Because the rupture process emits the largest amount of seismic radiation at the rupture front, the radiated P waves will change their polarization direction relative to the recording stations as the rupture propagates. Hence the results from simultaneous particle motion analysis at multiple stations can be stacked and the best fitting point for each time step can be considered as the center of the migrating rupture front. This imaging approach was introduced by Bayer et al. [2012] who demonstrated its applicability to large scale earthquake ruptures, namely the 2004 M_W9.1 Sumatra event and the 2008 M_W8.0 Wenchuan earthquake.

P wave polarization stacking is a geometry based rupture tracking approach. For the most simple case of a constant velocity model all polarization vectors at all stations would point exactly toward the event hypocenter at the initiation of rupture. The corresponding ray paths were straight lines and would intersect at the hypocenter. The analysis window for the polarization estimation is then shifted sample wise along the P wave train. For each consecutive time step, the rupture has propagated and the origin of the radiation is measured at slightly different back-azimuths. In this way, the rupture propagation

can be traced. For more realistic settings, it is convenient to constrain the rupture to a fixed plane or to neglect the information from the depth-component. The P phase polarization is determined by covariance matrix analysis [e.g., Jurkevics, 1988, Rentsch et al., 2006]. For a single station the covariance matrix analysis yields estimates for back-azimuth, dip, and wavefield linearity from a predefined time window from the three-component seismogram. Local polarization variation induced by, e.g., rock heterogeneity or anisotropy are site specific and are compensated by averaging over a sufficient number of well distributed stations. The stacking scheme reads as follows: the minimum of the function E is determined for each time step t after the P onset time [Bayer et al., 2012],

$$E(x, y, z, t) = \sum_{i=1}^{n_{station}} d_i^2(x, y, z, t) \cdot l_i^2(t), \tag{2.19}$$

where $d_i(x, y, z, t)$ is the shortest (orthogonal) distance between the back-azimuthal direction measured at station i for time t after P onset and the grid point (x, y, z) (usually x,y, and z are the longitude, latitude and depth values, respectively). $l_i(t)$ is the linearity of the particle motion for the given time step. Having values of $0 \leq l_i \leq 1$ it works as a weighting factor. The temporal migration of the minimum of E represents the progressing rupture front. The smaller the value of E_{min}, the better is the consistency of the measured back-azimuth estimates. In practice the back-azimuth estimates are often statically corrected, such that the estimate of first analysis time window is pinned toward the event hypocenter. Also the rupture plane is often predefined, such that, for example, the depth-component (z) is neglected, entirely.

The advantage of this approach is the fast and relatively easily obtained rupture track estimate. For a complex rupture pattern, e.g., a bilateral rupture, however, no constructive result can be expected. The approach becomes more reliable when many stations are azimuthally well distributed around the source and relative to the source-receiver distance, the rupture extent is in the order of at least a few degrees. The approach is limited to the duration of the P wave train before S wave onset, i.e., a tradeoff between a nearby station with potentially large back-azimuth variation and a long P minus S travel time must be accepted. For a suitable observation system this method is capable to recover rupture properties for events of intermediate size and below.

For example, in Folesky et al. [2018b] I used P wave polarization stacking in a comparative study of the 2016 Amatrice and Norcia earthquake sequence in central Italy in an attempt to recreate the results of the EGF study by Calderoni et al. [2017]. For the suitable events in this data set, i.e., the unilateral events with M≥5 both studies found concurring rupture directions in all cases. Here, the polarization-based approach had the advantage that the rupture directions were computed without a priori constraints on the fault orientation, in contrast to Calderoni et al. [2017]. On the other hand the P wave

polarization stacking cannot produce results for any event with a more complex rupture behavior.

In Chapter 5 the application of the P wave polarization stacking to locally obtained data from northern Chile, namely for the 2014 M_W8.1 Iquique event as well as its largest fore and aftershock is demonstrated, including an expansion to smaller events down to events of magnitude M_L=5 at that site.

Chapter 3

Microseismic Rupture Propagation Imaging

Key points:

- The back projection technique which was originally introduced in global seismology is adopted to microseismic scale in order to trace rupture propagation at a microseismic reservoir.
- Finite difference simulations of the ruptures suggest the feasibility of the approach for the enhanced geothermal system Basel-1.
- Rupture propagation and rupture paths for four $M_L \gtrsim 3$ events are obtained.
- The rupture process is directed from outside the stimulated volume toward its center for all four events.

This article has been published in GEOPHYSICS:
Folesky, J., Kummerow, J., & Shapiro, S. A. (2015). Microseismic rupture propagation imaging. Geophysics, 80(6), WC107-WC115, https://doi.org/10.1190/geo2014-0572.1

GEOPHYSICS, VOL. 80, NO. 6 (NOVEMBER-DECEMBER 2015); P. 1–9, 9 FIGS.
10.1190/GEO2014-0572.1

Microseismic rupture propagation imaging

Jonas Folesky[1], Joern Kummerow[1], and Serge A. Shapiro[1]

ABSTRACT

We have developed a method for tracing the rupture propagation of microseismic events. We referred to it as *microseismic rupture propagation imaging* (MRPI), which is an adaptation of the back projection technique from global seismology. Hence, we shifted back recorded waveforms to a grid of possible source locations and obtained a coherent phase stack that migrated according to the migration of the rupture front. Using synthetic ruptures and the corresponding waveforms obtained by finite-difference modeling, we tested the viability of the approach for a reservoir model with the properties and geometry of the monitoring system of the Basel-1 geothermal reservoir. First, we found that an estimation of the rupture location, orientation, direction, and length was feasible in this environment. The method was then applied to the four largest events ($M_L = 3.1$–3.4) recorded at the Basel-1 reservoir. We found that the obtained rupture lengths and orientations were reasonably consistent with independent estimates from seismic moments, stress drops, and fault-plane solutions. MRPI allowed us to solve the ambiguity between the actual fault plane and the auxiliary plane. The derived fault planes and rupture directions for the three best-determined events indicated that the failure process was directed preferentially from the periphery toward the injection source. This agreed with the observation that hypocenters of large-magnitude-induced events tend to occur on the edges of the stimulated volume. The results also corroborated the recently proposed idea that induced events were more probable to occur on preexisting faults if the potential rupture surface lay within the stimulated volume.

INTRODUCTION

In global seismology, tracking the rupture fronts of earthquakes with magnitudes from large ($M > 6$) to megathrust ($M > 8$) has recently become rather common. The most prominent applications are, e.g., the 2004 Sumatra-Andaman earthquake, the 2010 Maule, Chile, earthquake, or the 2011 Tohoku, Japan, earthquake (e.g., Krüger and Ohrnberger, 2005; Kiser et al., 2011, 2012; Bayer et al., 2012). A frequently used technique is to backproject the teleseismic P-wave seismograms recorded at an array or at a seismic network to a grid of possible source locations. This method is referred to as the *back-projection technique* (e.g., Ishii et al., 2007; Walker and Shearer, 2009) or the source-scanning algorithm (Kao and Shan, 2007) and is built on the constructive and destructive stack of seismic signals. It provides information on the energy release and yields estimates of rupture properties, such as direction, speed, and duration. To improve the precision, usually, coherent phases recorded by dense and large arrays are used so that different array-based time-correction techniques can be applied. A slightly different approach is followed by Allmann and Shearer (2007), who stack local S-wave records during the $M6.0$ Parkfield earthquake, 2004, to identify a high-frequency subevent. Using back projection is a direct and elegant way to obtain independent information on the characteristics of an earthquake. One main advantage of the method is to produce an estimate of the rupture geometry without the assumption of a rupture model. To date, there is, to our knowledge, no method of imaging the rupture geometry of microseismic events. Usually, the characteristic rupture dimensions are inferred indirectly from the measured body-wave spectra, and the results depend on a specific theoretical model (e.g., Brune, 1970; Madariaga, 1976). Few studies have used the empirical Green's function method to estimate the rupture direction and rupture velocity of clustered microseismic events (e.g., Jost et al., 1998).

Here, we modify the global back-projection technique and introduce the microseismic rupture propagation imaging (MRPI). Although the key idea of MRPI is similar to back projection, it dif-

Manuscript received by the Editor 3 December 2014; revised manuscript received 1 June 2015.
[1]Freie Universität Berlin, Institute of Geophysics, Berlin, Germany. E-mail: jonas.folesky@geophysik.fu-berlin.de; joern@geophysik.fu-berlin.de; shapiro@geophysik.fu-berlin.de.

fers in one important aspect. In the microseismic domain, one often works with monitoring systems consisting of azimuthally distributed receivers, which impedes the exploitation of the waveform coherency between different receivers. Sometimes, however, one knows quite accurately the velocity structure of the reservoir and can perform high-precision event locations with arrival-time residuals as small as the sample rate (e.g., 1–3 ms in the Basel case study, Kummerow et al., 2011). This then allows very accurate stacking of seismic signals recorded by well-distributed receivers, which constitutes a condition for the MRPI method.

In this paper, we show the application of the MRPI technique to synthetic and real data at reservoir scale. Our motivation is the occurrence of relatively large, induced seismic events at several geothermal reservoirs or waste disposal sites, having magnitudes of $M_L = 3$ and greater, thus yielding rupture length estimates of up to several hundred meters (e.g., Majer et al., 2007). The quantification of source parameters, as well as their relation to injection properties might be valuable for improved hazard assessment. The largest event observed during the stimulation of the Basel-1 geothermal reservoir in 2006 was a $M_L = 3.4$ event (Häring et al., 2008). We use the configuration of the monitoring system and the reservoir properties of the Basel geothermal experiment for synthetic modeling of several ruptures and their respective wave fields. We then apply the MRPI technique to the modeled results. We finally use the MRPI to image the ruptures of the four largest real events that occurred at the Basel site. This sequence of working steps allows us to examine the general influence of station geometry and station weighting, to compare synthetic and real imaging results, and to assess the limitations of our approach.

The estimation of the source parameters, such as rupture direction and length and their relation to the injection source, will not only help to better quantify the hazard potential of reservoirs, but it will also contribute to a better understanding of rupture processes at the microseismic scale and provide a link between laboratory scale studies and regional and global-scale studies.

MICROSEISMIC RUPTURE PROPAGATION IMAGING

Methodology

Back projecting recorded waveforms from all receivers to a grid of possible source locations is a simple and very straightforward approach to unravel some of the source properties. The mathematical idea is to stack all seismograms $u(t)$ recorded at n receivers as a function of time for every ith potential source grid point, corrected by the source-receiver travel time; i.e., for the P-wave

$$s_i(t) = \sum_{k=1}^{n} \omega_k |u_k(t + t_{ik}^p + \delta t_k^p)|. \quad (1)$$

Here, $s_i(t)$ is the stack at the ith source grid point, ω_k is a possible station specific weighting factor at the kth station, and t_{ik}^p is the predicted P-wave traveltime between the ith potential grid point location to the kth receiver location. The predicted traveltime represents the theoretical time that is needed for a seismic phase to reach the receiver depending on the actual location of the source, and it only leads to a high-amplitude stack of all contributing receivers if the respective grid point is indeed the location of the rupture front. The value δt_k^p is a time shift that corrects for the unmodeled velocity perturbations along the raypath to receiver k. Here, it is assumed to be constant for all grid points. By iterating this stacking procedure for all possible source points and time steps, one obtains a seismogramlike trace for every grid point, containing the stacked values for each time step. One also obtains a spatial distribution of stacks of back-shifted amplitudes for each time step. The squared amplitudes of these stacks (s_i^2) are related to the released seismic energy of the source, but due to normalization and weighting at the stations, they can only be used as a proxy. This stack function will be referred to as *brightness*. For an unilateral rupture, one ideally expects to have a well-defined maximum of brightness for each time step. This peak of brightness is considered to be the rupture front at one specific point in time. The peak migrates in time as the rupture progresses in one direction. In this way, the brightness distribution potentially provides estimates for rupture orientation, direction, length, duration, and speed.

In global studies, errors of the velocity model accumulate along the travel paths from the source to the receivers at teleseismic distances. To mitigate this effect, usually, the high waveform coherency of dense array data is exploited. This allows us to determine differential traveltimes of coherent phases between the array sensors, and these are used to modify the traveltime terms in the stacking procedure in equation 1 (e.g. Ishii et al., 2007).

In microseismic monitoring with distributed receivers, waveform similarity between recorded seismograms from different receiver locations is generally not high, and one has to apply equation 1 directly. Very accurate theoretical traveltimes are required to stack the signals from different receivers correctly. This availability of accurate theoretical traveltimes is, first, a precondition for the MRPI and, second, the most significant difference to global back-projection studies. Depending on the availability and performance of the given velocity model, it may be necessary to correct the traveltimes by using station correction terms δt_k^p in equation 1. These adjustments compensate mainly for unmodeled velocity heterogeneity along the path from the microseismic event cloud to the individual receivers.

In the Basel case, we use a two-layer velocity model (Häring et al., 2008) and the station correction terms calculated from averaging the residuals of the whole microseismic event cloud (Kummerow et al., 2011). Using those in combination with high-precision P- and S-arrival times leads to average arrival time residuals of the order of 1–3 ms for the observed microseismic events (Kummerow et al., 2011). Hence, the corrections are sufficiently precise to apply the stacking according to equation 1.

We must also correct for the influence of the specific station geometry of the microseismic monitoring system. This is achieved by a weighting scheme that defines the ω_k in equation 1. In our case, a straightforward way to address this is the computation of the relative azimuth between each contributing station and the hypocenter location. The weighting assigned to each single station is the sum of half of the azimuth differences to its respective neighbor stations. In this way, the influence of an asymmetric receiver distribution with respect to the hypocenter location can be decreased significantly. For each station, we compute the Euclidean sum from the three seismogram components for the P-phase window, and we then normalize the sum trace by its maximum. Next, we apply the station-dependent time shift using static station corrections. We also include an additional phase shift for each trace, which corrects

the first location of the focus of brightness depending on an a priori hypocenter location, obtained from P- and S-wave arrival-time inversions. The maximum allowed phase shift is given by the difference of the P-pick time and the first amplitude peak in the P-phase. In our case study in Basel, this difference is up to a few tens of milliseconds. The stacking is performed using equation 1 including the weighting factors explained above. As described, we track the peak of the brightness for each time step and define it as the track of the migrating rupture front. Using the P-phase and considering the relatively small aperture layout of the receivers with respect to the source, the depth resolution is not sufficient to resolve the depth migration of ruptures of microseismic dimension, especially as we cannot make use of waveform coherency as in e.g., Ishii et al. (2007). Hence, we restrict the MRPI to the horizontal plane fixed at hypocenter depth, which means that we recover the rupture projection on this plane. This approach is also supported by the predominantly strike-slip mechanisms found for the largest earthquakes at Basel by Deichmann and Giardini (2009).

SYNTHETIC DATA

Modeling

We use the finite-difference code Evamod (Saenger et al., 2000) to model seismic sources and their respective wavefields. Evamod allows us to place different sources at different times in a defined model space. To simulate a small event (point source), we define one location and a source type and compute the elastic wavefield, which is recorded by synthetic receivers. To model a propagating rupture, we put a straight line of sources in short horizontal distances next to each other, firing one after another. The resulting wavefield of a 200-m-long, unilateral, west–east-breaking rupture is shown in Figure 1. Note the strong directivity character.

Our model grid consists of 800^3 points and a grid spacing of 10 m. Multiple geophones can be placed at any location within the grid. We use a homogeneous, isotropic model with $V_P = 5940$ m/s, $V_S = 3450$ m/s, and $\rho = 3000$ kg/m^3, which are averaged values for the geothermal reservoir at Basel, Switzerland (Häring et al., 2008). The source time functions are Gaussian pulses with a central frequency of 20 Hz for each single source. The source type is explosion. This is sufficient for our rupture modeling. A more complex radiation pattern would be eliminated by trace normalization and station weighting (compare equation 1). To model a 200-m-long rupture, 11 explosion-type sources are used, which are horizontally offset by 20 m.

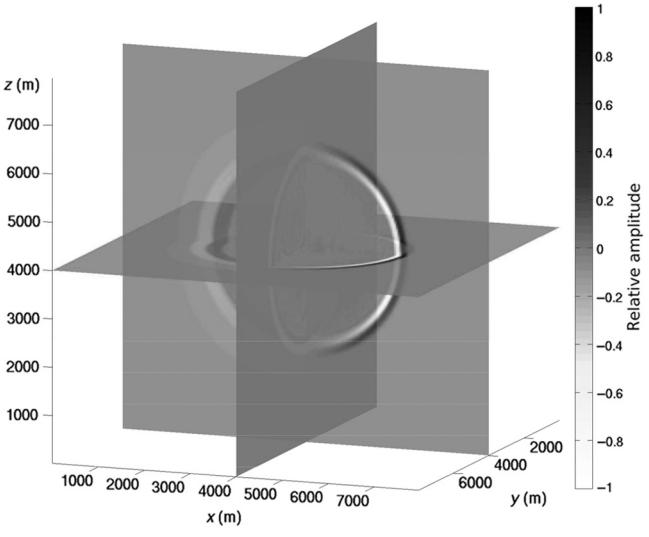

Figure 1. Snapshot of the x-component of the wavefield of an unilateral 200-m-long rupture, breaking from the west toward the east (corresponds to increasing x-values), illustrating the modeled directivity effect: The phase length and amplitude values vary strongly with the angle relative to the rupture direction (compare to the Doppler effect).

Rupture models

We first show synthetic tests for two horizontal ruptures imaged with full azimuthal coverage and then for three synthetic events imaged with the irregular Basel station configuration (cf. Figure 2). The events are placed at a depth of 4000-m below the surface, which corresponds to the open-hole section of the borehole and to the center of microseismicity in the reservoir (Häring et al., 2008). Because the analysis is restricted to a fixed depth (i.e., the hypocenter depth), we only model horizontal ruptures.

Full-azimuthal coverage

The first set of ruptures is surrounded azimuthally by 16 evenly distributed stations, which are located at a horizontal distance of 2500 m at 1000-m depth. The first rupture is unilateral and breaks horizontally from west to east and has a length of 200 m. The sec-

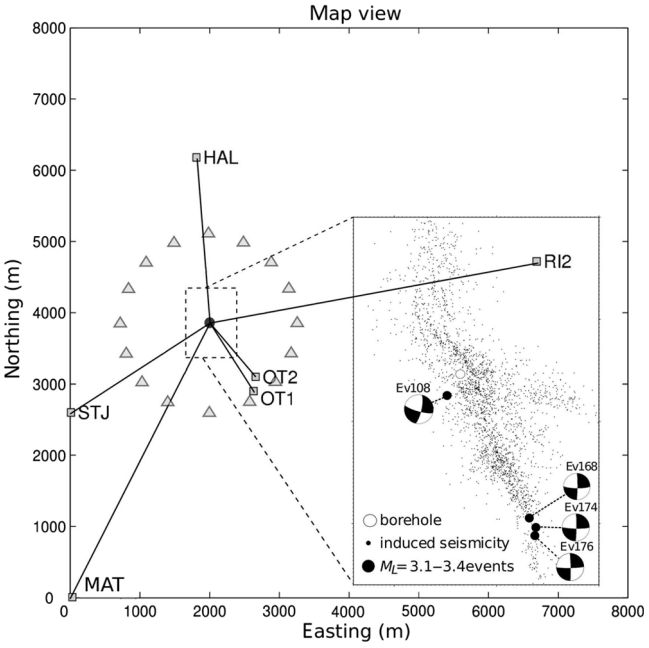

Figure 2. Basel station configuration with the borehole location in the center and study area indicated by the dashed square. The stations are weighted according to their relative azimuth coverage with respect to the source. The enlarged view shows the borehole location, the seismicity cloud, and the fault-plane solutions for the four largest events from the Basel site. The triangles illustrate a perfect station layout for some of the synthetic ruptures. However, receiver-station distances are shortened in the figure by a factor of two for visual composition.

ond rupture is a bilateral rupture nucleating at its center. It ruptures in the west and east directions, where each rupture leg is of 100 m length. MRPI snapshots of both ruptures for different time steps are shown in Figure 3. The brightness maxima are tracked as described and shown in Figure 4. The points with the highest brightness values at each time step represent the rupture path and are color coded with respect to their temporal occurrence.

The unilateral rupture is well recovered by the MRPI. The results show the rupture origin at the true location (black star in Figure 4, top left) and an eastward rupture migration at a length of 200 m. The hypocenter matches exactly with the modeled hypocenter location, and the direction of the rupture and its length are also precise. It should be mentioned, however, that the estimate of the rupture length is sensitive to the threshold value used (here, we use 66% of the maximum value for the synthetic models; see Figure 4). From all our synthetic models, we find that the rupture length tends to be underestimated.

The second rupture is bilateral. Again, we get the exact hypocenter and rupture orientation (Figure 4). The rupture directions and the lengths of the two rupture legs are correctly imaged to be 100 m in the east and west directions, respectively. Because the modeled rupture speed of both models was set as equal and the rupture dimensions are the same as for the unilateral rupture, the brightness stacks are very similar. A much shorter high-coherency phase (width of the brightness track) for the smaller bilateral rupture could be expected. However, the smearing due to the opposite directivity of the two rupture legs widens the time window of high coherency. Note that the final track of the bilateral event (Figure 4) is accurate, but it shows no migration of the center of brightness until about half of the rupture duration. Hence, the dynamic is not captured accurately, but the orientation and dimension are well resolved.

Realistic azimuthal coverage

In the next step, we consider a realistic station distribution. We use the Basel station distribution shown in Figure 2 with six distributed receivers to model three different microseismic events (a point source, a north–south-breaking rupture, and a west–east-breaking rupture).

The resulting rupture tracks are displayed in map view in Figure 5. The black points represent the time steps, when the brightness maximum exceeds the threshold value, and the gray points are

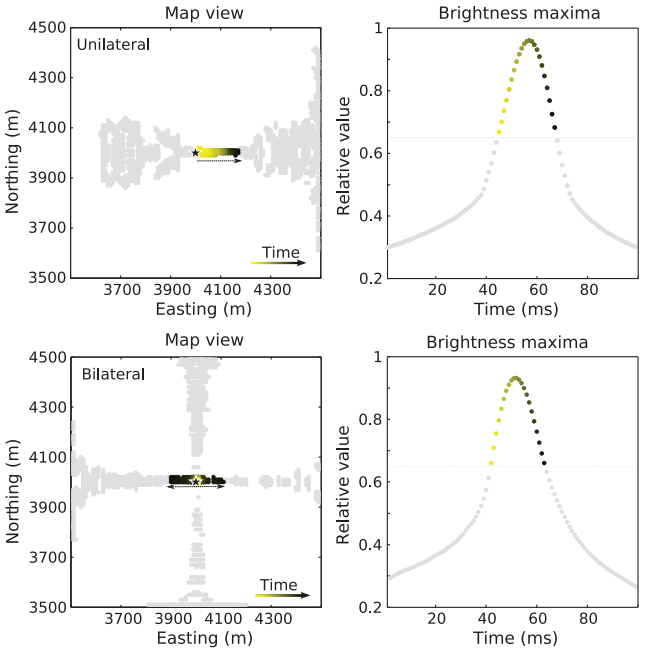

Figure 4. (Top) Rupture track and brightness maximum values over time corresponding to a 200-m west–east-breaking unilateral rupture. The color coding left and right correlates. The star is the nucleation point. The arrow shows the rupture direction. Time snapshots for that rupture are shown in Figure 3a. For the color-coded points, the amplitude of the stacked phases is above the threshold and the rupture is tracked. (Bottom) Track of a bilateral rupture and brightness maxima. The corresponding snapshots are shown in Figure 3b.

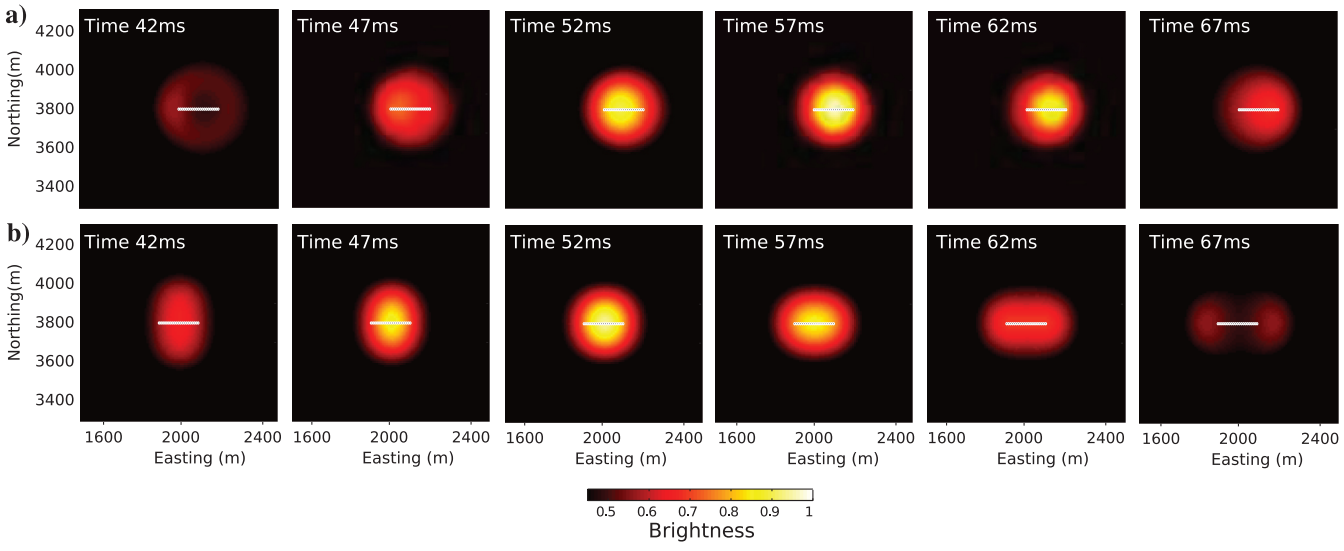

Figure 3. MRPI snapshots for six time steps for a west–east-breaking unilateral rupture (a) at the top, and a bilateral rupture (b) at the bottom. The white dots represent the modeled rupture path. The migration of the center of the bright spot represents the migration of the rupture front.

associated with small brightness values. The brightness level before and after the rupture, i.e., the coincidental summation of the projected amplitudes, is related to the site-specific geometric distribution of the receivers. The threshold is an empiric value, and it relies on several factors such as the number of contributing stations and the signal-to-noise ratio (S/N) of the seismogram traces.

The first of the modeled events (Figure 5a) is a point source, which simulates a very small microseismic event. The rupture track shows no artificial migration and is limited to the true hypocenter location (the black star in Figure 5a).

The second event (Figure 5b) is a north–south-breaking rupture of 200-m length. The MRPI technique works stably and clearly distinguishes the rupture trend from the rest of the stacked energy in the target area. The location of the rupture nucleation almost coincides with the modeled hypocenter location. The estimated rupture size of 180 m is close to the value of the model (200 m). The orientation, however, varies by approximately 25° from the original model as a consequence of the irregular and sparse station layout.

Figure 5c shows the third rupture, which breaks from the west toward the east. The difference to the north–south-breaking rupture is clearly resolved. In this case, the hypocenter is found precisely at the modeled position. The imaged rupture length is again slightly underestimated (180 m compared with 200 m in the model). The orientation also deviates by approximately 25° from the true orientation.

The comparison shows that the rupture parameters are recovered reasonably well in all three cases, but the rupture orientation is biased due to the limited azimuthal station coverage.

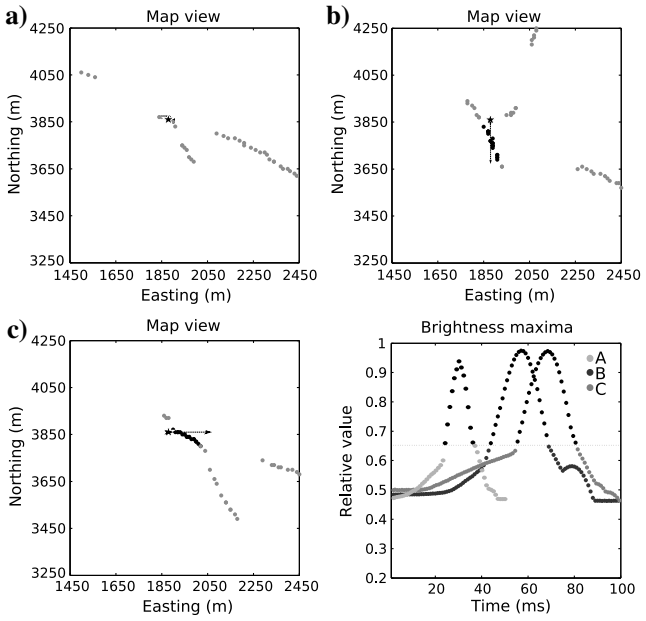

Figure 5. Horizontal rupture tracks and the corresponding brightness histories for three different synthetic ruptures using the sparse network geometry of the Basel case study. (a) MRPI results for a point source, (b) for a 200-m-long north–south-breaking rupture, and (c) for a 200-m-long west–east-breaking rupture. The black points show the spatiotemporal migration of the maximum brightness, which is interpreted as the migration of the rupture front. The gray points represent pre- and postrupture brightness. The black star is the independently obtained hypocenter location. The arrow indicates the rupture direction.

REAL DATA

The Basel enhanced geothermal system (EGS) data set has been described in detail by Häring et al. (2008). The microseismic cloud consists of more than 2800 located events, which are recorded by six downhole receivers distributed as shown in Figure 2. Different location studies based on the inversion of P- and S-wave arrival times consistently found a subvertical, north–northwest/south–southeast orientation of the seismicity distribution, which coincides with the direction of the maximum horizontal stress, SH_{max} (e.g., Häring et al., 2008; Dyer et al., 2010; Kummerow et al., 2011). The largest events occurred during and after the late phase of the injection experiment and finally led to its termination. Deichmann and Giardini (2009) find that nearly all of the large events were situated at the outer rim of the actual extent of the microseismic cloud and that they show mainly strike-slip mechanisms.

For this work, we have analyzed the waveforms of the four largest, $M_L = 3.1$–3.4 events. We have also tested the method for smaller ($M < 3$) events, but we did not obtain coherent results. The rupture lengths become too small to be resolvable. In the Basel case, the minimum magnitude for applying our imaging method is approximately $M = 3$, and this value is clearly related to the setup (the source-receiver distance, aperture, frequency band of the waveforms, and S/N).

The respective fault-plane solutions and locations of the four events are shown in Figure 2. We use the same two-layer velocity model and static station corrections as in the studies by Häring et al. (2008) and Kummerow et al. (2011). The hypocenter locations

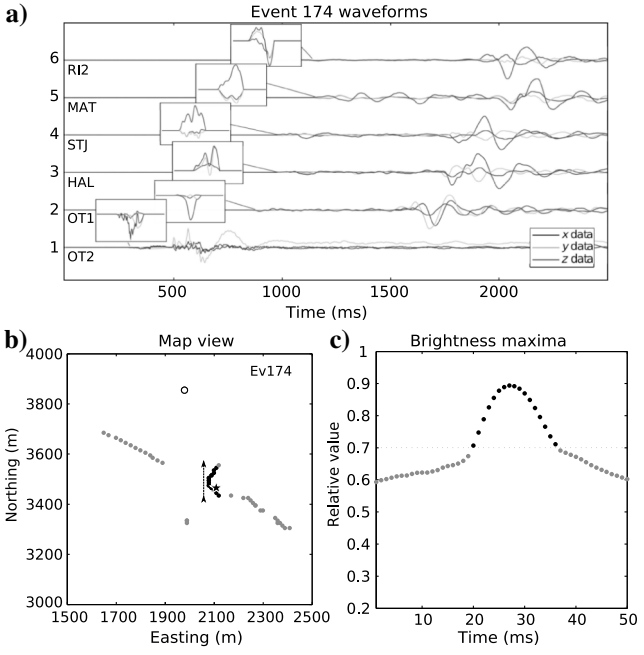

Figure 6. (a) Displacement waveforms for the Basel event Ev_{174} ($M_L = 3.2$) recorded at six downhole instruments at the locations shown in Figure 2. The P-phase display is increased. Station OT2 is situated in the crystalline basement, and it shows a higher frequency content. (b) Rupture track. The black track points represent the rupture path. The star is the hypocenter and the circle is the borehole. (c) Temporal evolution of the maximum value of brightness for the same event.

found therein are taken as reference hypocenters. The waveforms for an exemplary event Ev_{174} are shown in Figure 6a (using the event nomenclature of Deichmann and Giardini, 2009).

Results

We apply the MRPI technique to the four largest events from the Basel experiment, and we show the complete results for the event Ev_{174} ($M_L = 3.2$) in greater detail. The large events in the Basel reservoir show unilateral behavior, and we only track a single maximum per time step and define this as the rupture front at this particular time step. The threshold, whose excess defines the rupture length, is now chosen manually at a value of 0.7, where the slope of the brightness function steepens abruptly. If the brightness does not focus as clearly as it does here, the picking of a threshold value may become impossible or involve large uncertainties of the derived rupture parameters. One reason for such an observation could be, for example, a more complex rupture behavior than unilateral or bilateral. In our case, however, the rupture of event Ev_{174} is well defined by the brightness function appearing between the imaging time steps of 18 and 38 ms (Figures 6c and 7). The corresponding positions are shown in the map view of Figure 6b. The first location is the black point that lies farthest in the south, and the rupture front then migrates from south to north. The rupture nucleation point matches the hypocenter location. The length of the rupture is approximately 150 m. The gray tracking points, before and after

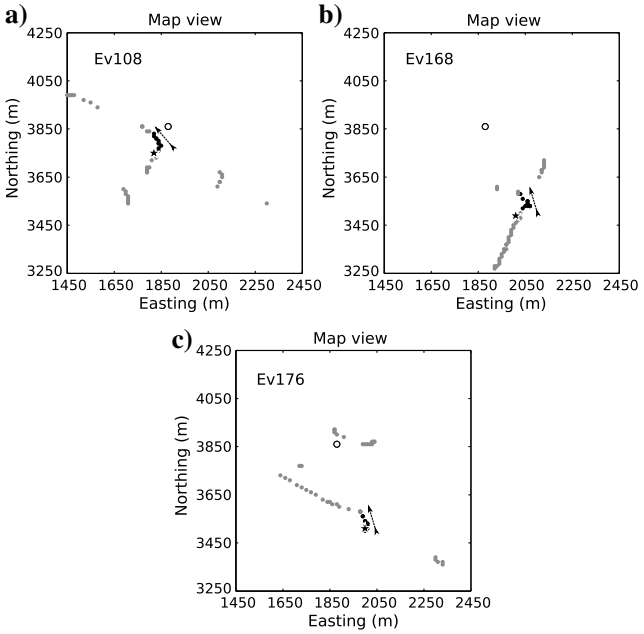

Figure 8. Same as Figure 6b, but for events (a) Ev_{108}, (b) Ev_{168}, and (c) Ev_{176}. Estimated rupture direction for events Ev_{168} and Ev_{176} is south–southeast to north–northwest and for event Ev_{108} southeast to northeast.

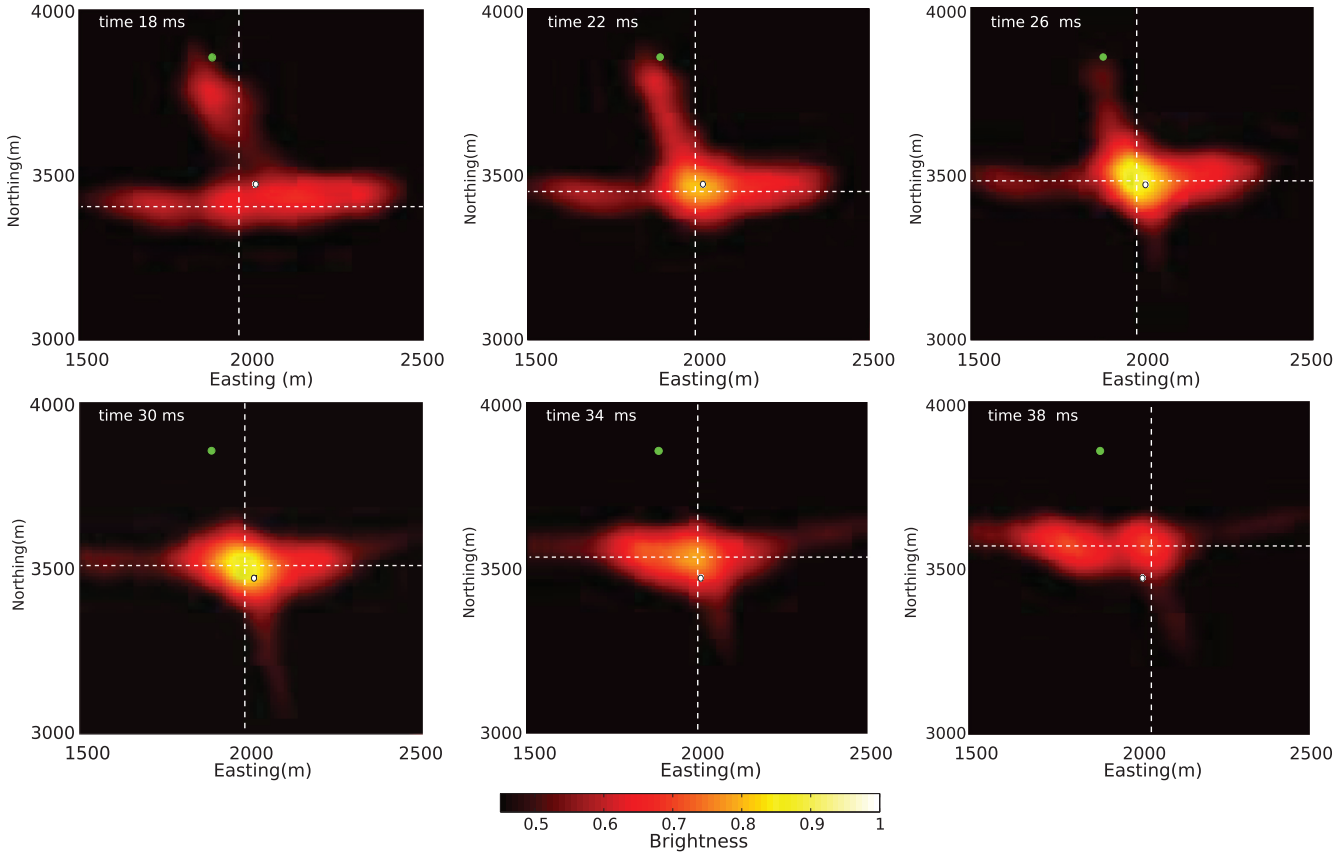

Figure 7. MRPI snapshots for the times 18–38 ms for Ev_{174}. The brightness focus position is indicated by the crossing of the white dotted lines. Its motion is considered to be the migration of the rupture front. The green circle is the borehole, and white is the (first-arrival based) hypocenter location. The corresponding rupture path is shown in Figure 8.

the defined rupture time interval, show a general trend that strongly depends on the station geometry of the site and is not related to the physical rupture. For the Basel setup, this track mostly starts in the south–southeast and migrates toward the north–northwest. The trend changes when the backshifted phases of the different receivers start to coincide, and the brightness value exceeds the threshold value. Figure 8 shows that the results for the other ruptures are generally similar. We find south–north rupture directions for the events Ev_{168} and Ev_{176} with rupture lengths of 120 m. Event Ev_{108} seems to have a slightly different rupture orientation (southeast to northwest).

For all four ruptures, we find coherent brightness maxima for a similar duration localized close to the hypocenter location covering an area of similar size. The consistency of the results for the four events with similar magnitudes and source mechanisms increases our confidence in the validity of the method.

DISCUSSION

The imaged rupture nucleation points for the synthetic ruptures coincide with the true positions of the modeled hypocenters almost perfectly. In the real data case, the offset between the imaged nucleation points and the reference hypocenters (from the arrival-time-based location study by Kummerow et al., 2011) is in the range of tens of meters. We address the offset primarily to the differences of the location method and the MRPI. Although the first method uses the first onset of the seismic phases, the MRPI is more sensitive to the higher amplitudes following the first onsets.

Using MRPI, the rupture orientation is very well recovered for a good azimuthal station coverage and it loses precision when a sparse monitoring network is used (compare Figures 4 and 5). For the Basel case, we find deviations of up to 25° in the synthetic analysis. For the real ruptures shown in this study, the imaged orientations are in the south–southeast/north–northwest direction, close to the north–south-striking nodal planes found by Deichmann and Giardini (2009) from fault-plane solutions for the same events (Figure 2). Thus, the MRPI results suggest that the north–south-striking nodal planes are the actual fault planes.

In this study, we find approximate rupture lengths of 120–150 m. We compare this with estimates computed assuming a circular fault (Eshelby, 1957) and a rectangular fault (Knopoff, 1958). Taking the stress drop value of 10 MPa, which was found (by Goertz-Allmann et al. (2011a)) to be representative for the region of the largest events at the rim of the microseismic cloud at Basel, and using the conversion relation by Goertz-Allmann et al. (2011b) for local to moment magnitudes, we obtain rupture radii of approximately

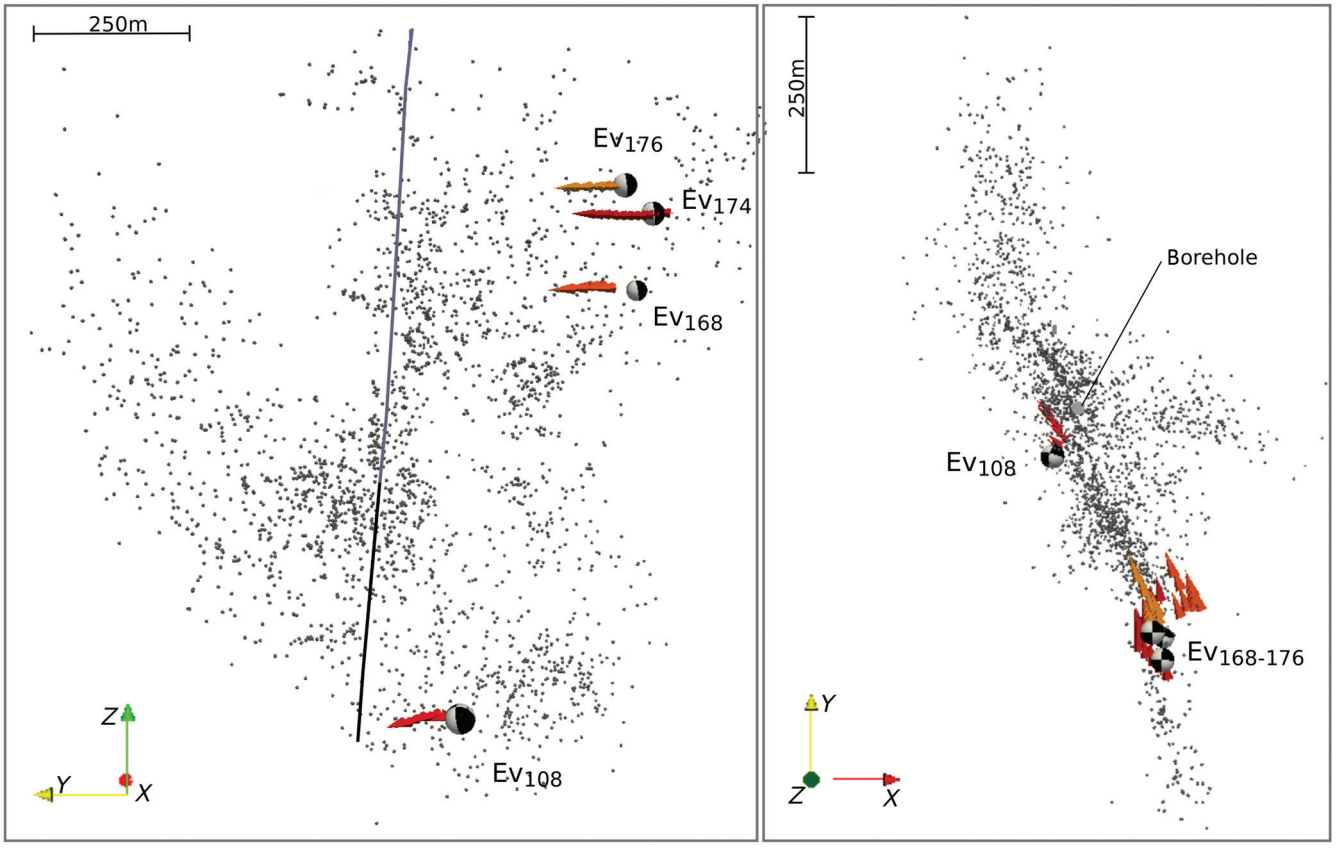

Figure 9. Basel microseismic cloud from (left) side and (right) map view. The borehole is the thin blue line, and the open hole section is black. The small gray dots represent microseismic event locations. The fault-plane solutions by Deichmann and Giardini (2009) for the four largest events are shown at their hypocenter locations. The respective rupture tracks are shown as arrows in reddish colors. Notice that the rupture tracks for all events are consistent with the shape of the seismic cloud. The rupture directions match the fault-plane solutions reasonably. Only Ev_{108} shows a deviation between the rupture orientation and the orientation of the possible fault plane of approximately 25°. The others fit significantly better. Notice that with the application of MRPI, the ambiguity of the fault-plane solutions can be solved. Also, note that all rupture directions point toward the injection well.

100–150 m and rupture lengths of approximately 130–350 m, respectively. The estimates found by MRPI are at the lower end of this range. One should, however, keep in mind that the dimensions by the rupture models are only rough estimates. Furthermore, varying stress drop values within the reservoir may produce differences in rupture lengths. Note also, that MRPI is limited to the horizontal projection of each event. Hence, the MRPI provides a lower bound estimate of the rupture length.

An interesting observation following from our results is derived from the direction of rupture propagation. The four analyzed ruptures from the Basel reservoir show unilateral behavior and break mainly from the southeast toward the northwest. This is the direction from the periphery of the stimulated volume toward the open borehole (see Figure 9). They are also the largest events that occurred during the experiment. These findings are consistent with the observation that in EGSs, large-magnitude events tend to occur on the edges of the stimulated volume (Majer et al., 2007). Goertz-Allmann and Wiemer (2013) propose a geomechanical model that explains this observation based on the inverse relationship between the seismic *b*-value and differential stress.

The observations mentioned above (by Majer et al. [2007] and ours) seem to corroborate the recently proposed idea that induced events are more probable to occur on preexisting faults if the potential rupture surface lies nearly completely within the stimulated volume (Shapiro et al., 2011). The authors derived this hypothesis from observing an underrepresentation of large-magnitude induced events in the frequency-magnitude statistics. They propose a simple physical justification of the hypothesis based on a balance of the surface-integrated friction force and tangential traction acting along the complete potential rupture surface. This hypothesis includes the possibility of large rupture surfaces spanning a range from an internal region to the far periphery of the stimulated volume. Such rupture surfaces would be sufficiently perturbed by a fluid injection at the moment when a sufficient pressure variation has reached potential rupture domains farthest from the injection source. It is very probable that such a far-distant domain of the potential rupture surface would then correspond to the hypocenter of a large induced event (because the rupture could start immediately after this domain has been perturbed). Thus, the rupture would be highly probable to propagate backward to the injection source. Our results on the rupture propagation at the Basel location agree well with this model. Moreover, our observations and the described scenario are in good agreement with one more known observation reported by Majer et al. (2007): The largest events tend to occur at the end of the injection period or even after its termination. It is clear that exactly this must be the case for large ruptures propagating from the rim of the stimulated volume toward the injection source.

Note, however, that there are also publications reporting a broad spatial distribution of large-magnitude events in microseismic clouds (i.e., Asanuma et al., 2005; Mukuhira et al., 2013).

CONCLUSIONS

We show the capability of the MRPI technique to image rupture processes in microseismic reservoirs for relatively large events and to distinguish between synthetic events such as point sources and unilateral and bilateral ruptures of different rupture directions.

The rupture parameters nucleation point (hypocenter), rupture orientation, direction, and length can be estimated. However, using a realistic, sparsely distributed monitoring system, the rupture orientation is biased.

Based on an adequate velocity model, we image the rupture of the four largest, $M_L = 3.1–3.4$ microseismic events at Basel and estimate their rupture parameters. The rupture orientations found here are reasonably consistent with the orientations of one of the nodal planes of the fault-plane solutions obtained independently by Deichmann and Giardini (2009). Moreover, our method allows to resolve the ambiguity of the nodal planes and determine the actual fault plane. The rupture dimensions we find are in the same range as the estimates obtained by using stress-drop estimates for Basel by Goertz-Allmann et al. (2011a).

Additionally, our results indicate that the rupture nucleation points lie further away from the well than the rupture termination points, which suggests that the largest induced events at Basel tend to rupture toward the injection point.

ACKNOWLEDGMENTS

We are very grateful to M. Häring and H. Asanuma for providing us with the waveform data. We thank the sponsors of the PHASE Consortium for supporting the research presented in this paper.

REFERENCES

Allmann, B. P., and P. M. Shearer, 2007, A high-frequency secondary event during the 2004 Parkfield earthquake: Science, **318**, 1279–1283, doi: 10.1126/science.1146537.

Asanuma, H., H. Nozaki, H. Niitsuma, and D. Wyborn, 2005, Interpretation of microseismic events with larger magnitude collected at Cooper Basin, Australia: Transactions of the Geothermal Resource Council, **29**, 87–91.

Bayer, B., R. Kind, M. Hoffmann, X. Yuan, and T. Meier, 2012, Tracking unilateral earthquake rupture by P-wave polarization analysis: Geophysical Journal International, **188**, 1141–1153, doi: 10.1111/j.1365-246X.2011.05304.x.

Brune, J., 1970, Tectonic stress and the spectra of seismic shear waves from earthquakes: Journal of Geophysical Research, **75**, 4997–5009, doi: 10.1029/JB075i026p04997.

Deichmann, N., and D. Giardini, 2009, Earthquakes induced by the stimulation of an enhanced geothermal system below Basel (Switzerland): Seismological Research Letters, **80**, 784–798, doi: 10.1785/gssrl.80.5.784.

Dyer, B. C., U. Schanz, T. Spillmann, F. Ladner, and M. O. Häring, 2010, Application of microseismic multiplet analysis to the Basel geothermal reservoir stimulation events: Geophysical Prospecting, **58**, 791–807, doi: 10.1111/j.1365-2478.2010.00902.x.

Eshelby, J. D., 1957, The determination of the elastic field of an ellipsoidal inclusion, and related problems: Proceedings of the Royal Society of London: Series A, **241**, 376–396.

Goertz-Allmann, B. P., A. Goertz, and S. Wiemer, 2011a, Stress drop variations of induced earthquakes at the Basel geothermal site: Geophysical Research Letters, **38**, L09308, doi: 10.1029/2011GL047498.

Goertz-Allmann, B. P., B. Edwards, F. Bethmann, N. Deichmann, J. Clinton, D. Fäh, and D. Giardini, 2011b, A new empirical magnitude scaling relation for Switzerland: Bulletin of the Seismological Society of America, **101**, 3088–3095.

Goertz-Allmann, B. P., and S. Wiemer, 2013, Geomechanical modeling of induced seismicity source parameters and implications for seismic hazard assessment: Geophysics, **78**, no. 1, KS25–KS39, doi: 10.1190/geo2012-0102.1.

Häring, M. O., U. Schanz, F. Ladner, and B. C. Dyer, 2008, Characterization of the Basel 1 enhanced geothermal system: Geothermics, **37**, 469–495, doi: 10.1016/j.geothermics.2008.06.002.

Ishii, M., P. M. Shearer, H. Houston, and J. E. Vidale, 2007, Telseseismic P wave imaging of the 26 December 2004 Sumatra-Andaman and 28 March 2005 Sumatra earthquake ruptures using the Hi-net array: Journal of Geophysical Research, **112**, B11307, doi: 10.1029/2006JB004700.

Jost, M. L., T. Büsselberg, Ö. Jost, and H.-P. Harjes, 1998, Source parameters of injection-induced microearthquakes at 9-km depth at the KTB deep drilling site, Germany: Bulletin of the Seismological Society of America, **88**, 815–832.

Kao, H., and S.-J. Shan, 2007, Rapid identification of earthquake rupture plane using source-scanning algorithm: Geophysical Journal International, **168**, 1011–1020, doi: 10.1111/j.1365-246X.2006.03271.x.

Kiser, E., and M. Ishii, 2011, The 2010 Mw 8.8 Chile earthquake: Triggering on multiple segments and frequency-dependent rupture behavior: Geophysical Research Letters, **38**, L07301, doi: 10.1029/2011GL047140.

Kiser, E., and M. Ishii, 2012, The March 11, 2011 Tohoku-oki earthquake and cascading failure of the plate interface: Geophysical Research Letters, **39**, L00G25, doi: 10.1029/2012GL051170.

Knopoff, L., 1958, Energy release in earthquakes: Geophysical Journal of the Royal Astronomical Society, **1**, 44–52, doi: 10.1111/j.1365-246X.1958.tb00033.x.

Krüger, F., and M. Ohrnberger, 2005, Spatio-temporal source characteristics of the 26 December 2004 Sumatra earthquake as imaged by teleseismic broadband arrays: Geophysical Research Letters, **32**, L24312, doi: 10.1029/2005GL023939.

Kummerow, J., S. A. Shapiro, H. Asanuma, and M. Häring, 2011, Application of an arrival time and cross correlation value-based location algorithm to the Basel 1 microseismic data: 73rd Annual International Conference and Exhibition, EAGE, Extended Abstracts, P193.

Madariaga, R., 1976, Dynamics of an expanding circular fault: Bulletin of the Seismological Society of America, **66**, 639–666.

Majer, E. L., R. Baria, M. Stark, S. Oates, J. Bommer, B. Smith, and H. Asanuma, 2007, Induced seismicity associated with enhanced geothermal systems: Geothermics, **36**, 185–222, doi: 10.1016/j.geothermics.2007.03.003.

Mukuhira, y., H. Asanuma, H. Niitsuma, and M. O. Häring, 2013, Characteristics of large-magnitude microseismic events recorded during and after stimulation of a geothermal reservoir at Basel, Switzerland: Geothermics, **45**, 1–17, doi: 10.1016/j.geothermics.2012.07.005.

Saenger, E. H., N. Gold, and S. A. Shapiro, 2000, Modeling the propagation of elastic waves using a modified finite-difference grid: Wave Motion, **31**, 77–92, doi: 10.1016/S0165-2125(99)00023-2.

Shapiro, S. A., O. Krüger, , C. Dinske, and C. Langenbruch, 2011, Magnitudes of induced earthquakes and geometric scales of fluid-stimulated rock volumes: Geophysics, **76**, no. 6, WC55–WC63, doi: 10.1190/geo2010-0349.1.

Walker, K. T., and P. M. Shearer, 2009, Illuminating the near-sonic ruptur velocities of the intracontinental Kokoxili M_w 7.8 and Denali fault M_w 7.9 strike-slip earthquakes with global P wave back projection imaging: Journal of Geophysical Research, **114**, B02304, doi: 10.1029/2009JG000990.

Chapter 4

Rupture Directivity of Fluid-Induced Microseismic Events: Observations from an Enhanced Geothermal System

- Out of 2800 fluid-induced microseismic events with of $0 \leq M_L \leq 3$ rupture directivity could be estimated for 195 applying an empirical Green's functions approach.
- A persistence of unilateral rupture behavior, rupture directivity and source complexities for events down to $M_L \approx 1$ is demonstrated.
- At this EGS site rupture directivity shows dependencies on location and magnitude.
  - Small events in vicinity of the borehole show random oriented directivity.
  - Small events located further away from the injection point show rupture orientation approximately parallel to the presumed fault structure.
  - Events with $M_L \geq 1.8$ are located at the rim of the stimulated volume and rupture inward the microseismic cloud.

This article has been published in Journal of Geophysical Research - Solid Earth:
Folesky, J., Kummerow, J., Shapiro, S. A., Häring, M., & Asanuma, H. (2016). Rupture directivity of fluid-induced microseismic events: Observations from an enhanced geothermal system. Journal of Geophysical Research: Solid Earth, 121(11), 8034-8047, https://doi.org/10.1002/2016JB013078

AGU PUBLICATIONS

JGR

Journal of Geophysical Research: Solid Earth

RESEARCH ARTICLE
10.1002/2016JB013078

Key Points:
- Comprehensive directivity study on fluid-induced microseismic events applying an EGF technique
- Rupture directivity is predominantly unilateral and shows dependencies on distance and magnitude
- Largest microseismic events nucleate at the reservoir rim and rupture back toward the borehole

Correspondence to:
J. Folesky,
jonas.folesky@geophysik.fu-berlin.de

Citation:
Folesky, J., J. Kummerow, S. A. Shapiro, M. Häring, and H. Asanuma (2016), Rupture directivity of fluid-induced microseismic events: Observations from an enhanced geothermal system, *J. Geophys. Res. Solid Earth*, *121*, doi:10.1002/2016JB013078.

Received 8 APR 2016
Accepted 8 OCT 2016
Accepted article online 12 OCT 2016

Rupture directivity of fluid-induced microseismic events: Observations from an enhanced geothermal system

Jonas Folesky[1], Jörn Kummerow[1], Serge A. Shapiro[1], Markus Häring[2], and Hiroshi Asanuma[3]

[1]Department of Geophysics, Freie Universität Berlin, Berlin, Germany, [2]Geo Explorers Ltd., Liestal, Switzerland, [3]North Japan Research Institute for Sustainable Energy, Hirosaki University, Aomori, Japan

Abstract The rupture process of fluid-induced microseismic events is still poorly understood, mainly due to usually small magnitudes and sparse monitoring geometries. The high-quality recordings of the earthquake sequence 2006–2007 at the enhanced geothermal system at Basel, Switzerland, constitute a rare exception, allowing a systematic directivity study of 195 events using the empirical Green's function method. We observe clear directivity signatures for about half the events which demonstrates that rupture directivity persists down to small magnitudes ($M_L \sim 1$). The predominant rupture behavior is unilateral. We further find evidence that directivity is magnitude dependent and varies systematically with distance from the injection source. Whereas pore pressure seems to play the dominant role close to the injection source and no preferred rupture direction is observable, directivity aligns parallel to the event distribution with increasing distance ($\gtrsim$100 m) and is preferably oriented away from the injection point. The largest analyzed events ($M_L \sim 2$) show a distinct behavior: They rupture toward the injection source, suggesting that they nucleate in the vicinity of the pressure front and propagate backward into the perturbed volume. This finding is of particular relevance for seismic hazard assessment of georeservoirs, since it implies that maximum event size is related to dimension of the fluid-perturbed volume. Our study also resolves rupture complexities for a small group of events. This shows that small fault heterogeneities exist down to a scale of a few tens of meters. The observation of directivity and complexity in induced microseismic events suggest that future source studies account for these phenomena.

1. Introduction

For numerous large- and moderate-sized earthquakes rupture directivity has been retrieved successfully from azimuthal variations of seismic pulse length, amplitude, and source spectra [e.g., *Ben-Menahem*, 1961; *Boatwright and Boore*, 1982; *Frankel and Kanamori*, 1983]. *Boatwright* [2007], *Dreger et al.* [2007], *Kane et al.* [2013], and *Taira et al.* [2015] found evidence for rupture directivity of small ($2 \leq M \leq 5$) natural earthquakes. Observations of directivity effects from fluid-induced microseismic events ($M \leq 2$), however, are to date only sparse and restricted to few events [*Li et al.*, 1995; *Jost et al.*, 1998], and particularly, their rupture processes have remained poorly understood. In contrast to large earthquakes, where unilateral ruptures seem to prevail [*McGuire et al.*, 2002], simple circular fault models [*Brune*, 1970; *Madariaga*, 1976; *Boatwright*, 1980] are generally invoked in the microseismic context when source parameter studies are performed [e.g., *Goertz-Allmann et al.*, 2011]. These studies implicitly assume ideal circular and hence symmetric ruptures which exhibit no rupture directivity, although a reliable empirical knowledge on spatiotemporal rupture characteristics is missing due to the poor resolution and sparse geometries of microseismic monitoring systems.

But what should be considered if clear signatures of directivity are indeed identified also in fluid-induced microseismic data? This will then require more complex rupture models that comprise directivity [e.g., *Madariaga*, 1976; *Kaneko and Shearer*, 2015], or it could suggest the application of models like unilateral or bilateral ruptures [e.g., *Haskell*, 1964]. A distinction between the different models within a source study would allow to improve the characterization of microseismic source parameters (e.g., fault size and stress drop) and could also be valuable for an enhanced hazard assessment of fluid-induced microseismicity. In fact, several studies of natural [*Dreger et al.*, 2007; *Taira et al.*, 2015] and mining-induced seismicity [*Yamada et al.*, 2005; *Kwiatek et al.*, 2011] found indications for rupture complexity of microearthquakes. *Dreger et al.* [2007] and *Taira et al.* [2015] identified complex slip behavior, high stress drop, and directivity for small natural events in California. *Yamada et al.* [2005] analyzed the source parameters of small events at the Mponeng gold mine,

South Africa, and observed values typical for larger natural seismicity. For the same gold mine *Kwiatek et al.* [2011] deduced self-similar behavior of seismic events even down to magnitudes as small as $M_W \sim -4$.

The objective of this study is to perform for the first time a comprehensive, empirical study of rupture directivity for fluid-induced microseismicity. Additionally, we describe examples of complex rupture behavior for microseismic sources. We use high-quality waveforms of microseismicity recorded at the Basel-Enhanced Geothermal System, Switzerland, during and after the stimulation in 2006–2007 [*Häring et al.*, 2008]. The event magnitude range is $0.0 \leq M_L \leq 3.4$. Using multiplet analysis, we select pairs of colocated events with similar source mechanisms and perform an empirical Green's functions (EGF) analysis [*Mueller*, 1985; *Li et al.*, 1995] in order to reconstruct the relative source time functions (RSTFs) of the seismic events for each station. Rupture directivity is then inferable from systematic variations of amplitude or duration of the RSTFs with station azimuth [*Savage*, 1965]. We subsequently examine the spatial and temporal distribution of the obtained rupture orientations and directivity and analyze possible controlling factors. Specifically, we find a dependence of rupture directivity on event size and distance from the injection source.

2. Data: The Induced Microseismicity at the Basel EGS

In this study we use about 2800 microseismic events which were induced during the stimulation of the Basel-1 geothermal site, Switzerland, in December 2006 and also during several months of the postinjection phase until June 2007 [*Häring et al.*, 2008]. The microseismicity was monitored by a network of six azimuthally well distributed three-component downhole receivers within a distance of up to 5 km from the injection source (Figure 1). Sampling rate for all receivers was 1 kHz. The located microseismic event cloud centers at a depth of about 4.5 km and extends about 1 km in horizontal and also about 1 km in vertical direction. The seismicity shows a subvertical, north-north-west to south-south-east orientation which almost coincides with the direction of the maximum horizontal stress, S_{Hmax} [*Häring et al.*, 2008; *Dyer et al.*, 2010]. We use refined event locations, based on multiplet analysis and optimized *P* and *S* phase arrival times [*Kummerow et al.*, 2011; *Reshetnikov et al.*, 2015]. The event magnitudes range between $0.0 \leq M_L \leq 3.4$, and the largest events occurred during and after the late phase of the injection experiment. The predominant source mechanisms of the Basel events are strike-slip and oblique faulting [*Deichmann and Giardini*, 2009; *Kraft and Deichmann*, 2014].

Deichmann and Giardini [2009] found that nearly all large events were situated at the outer rim of the actual extent of the microseismic cloud. Studies by *Catalli et al.* [2013] and *Goertz-Allmann et al.* [2011] indicate that seismicity attributes at Basel correlate with the pore pressure, which itself decreases with the distance from the injection source [*Dinske and Shapiro*, 2010]. *Goertz-Allmann et al.* [2011] found an increase of average stress drop with increasing radial distance and decreasing pore pressure, and *Catalli et al.* [2013] observed that the performance of their Coulomb model improves progressively with increasing distance (i.e., decreasing influence of the pore pressure). *Kummerow et al.* [2014] also noted that the distribution of repeating earthquakes at Basel is particularly sensitive to the pore pressure.

3. Method: Empirical Green's Functions and Directivity Effect

A recorded seismogram can be described as the convolution of four time series, e.g.,

$$u(t) = s(t) * p(t) * r(t) * i(t), \tag{1}$$

where $u(t)$ is the recorded seismogram, $s(t)$ is the source time function, $p(t)$ is the impulse response of the path, $r(t)$ is the influence of the recording site, and $i(t)$ is the instrument response. The aim of the empirical Green's function (EGF) method is to compute a relative source time function (RSTF) for a larger event, assuming that it is colocated with a smaller event with a similar focal mechanism [e.g., *Mueller*, 1985; *Frankel et al.*, 1986; *Mori*, 1993]. Then, the source time function of the smaller event is approximately a delta pulse, $s(t) \approx \delta(t)$, and the seismogram of the smaller event is deconvolved from the seismogram of the larger event to obtain the relative source time function. In the frequency domain, this can be expressed as

$$\frac{|U(\omega)|}{|\mathrm{EGF}(\omega)|} \approx \frac{|S(\omega) \cdot P(\omega) \cdot R(\omega) \cdot I(\omega)|}{|\delta(\omega) \cdot P(\omega) \cdot R(\omega) \cdot I(\omega)|} = \frac{|S(\omega)|}{|\delta(\omega)|} = |S'(\omega)|, \tag{2}$$

where $\mathrm{EGF}(\omega)$ is the spectrum of the smaller event and $S'(\omega)$ is the RSTF (relative to the seismic moment of the smaller event), since the effects of path, receiver site, and instrument response are equal and can be

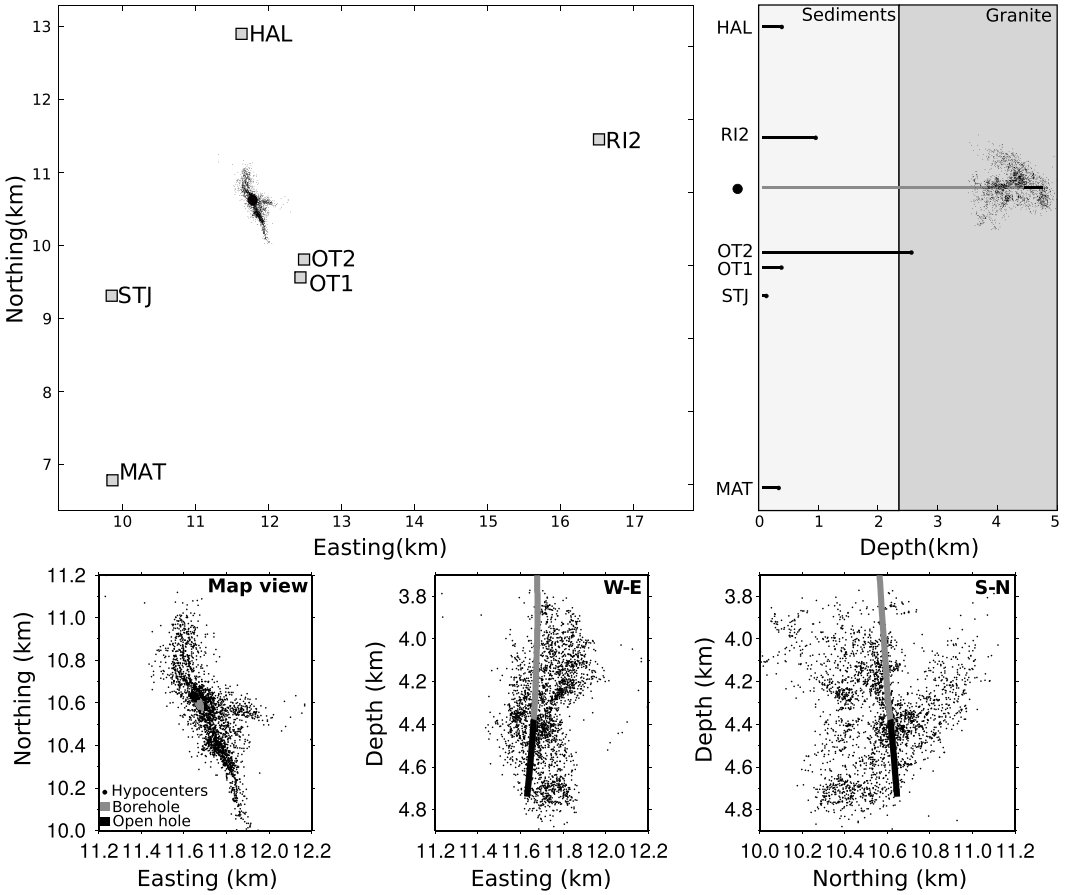

Figure 1. (top row) Station distribution and microseismic event cloud at the Basel EGS. The station geometry is displayed in map view and in a schematic depth view. (bottom row) The microseismicity is shown in map and depth views together with the borehole and open hole section.

eliminated. The technique of spectral division is described by, e.g., *Mueller* [1985], *Li et al.* [1995], and *Vallée* [2004]. This deconvolution is only valid for frequencies below the corner frequency of the EGF spectrum, where the delta pulse assumption of the EGF holds (this means that $\delta(\omega)$ is a constant). In practice the procedure sometimes needs stabilization, e.g., by a water level correction [*Mueller*, 1985] or a Gaussian filter for both numerator and denominator [*Li et al.*, 1995] or the application of the Projected Landweber Method [*Vallée*, 2004].

For propagating ruptures the RSTF exhibits variations of amplitudes and duration as a function of the rupture-receiver geometry. *Savage* [1965] derived the following formula

$$F = \frac{K}{A} = \frac{i \cdot v_r}{1 - (v_r/c)^i \cdot \cos^i(\phi - \phi_0) \cdot \sin^i(\theta - \theta_0)}, \tag{3}$$

where F describes the reciprocal of the expected amplitude A at a given station, scaled by an unknown constant K. v_r is the rupture velocity and c is the phase velocity, respectively. ϕ is the station azimuth relative to the hypocenter and θ is the station plunge. As the rupture plane is assumed to be vertical, the angles ϕ_0 and θ_0 are sufficient to describe the rupture geometry. ϕ_0 is the azimuthal orientation of the rupture plane and θ_0 describes the tilt of the rupture direction inside that rupture plane. The coordinate system is illustrated in Figure 2. The formula describes unilateral ruptures for $i = 1$ and bilateral ruptures for $i = 2$. A similar expression is given for the modulation of the source duration

$$T = \frac{L}{i \cdot v_r} \cdot \left(1 - (v_r/c)^i \cdot \cos^i(\phi - \phi_0) \cdot \sin^i(\theta - \theta_0)\right), \tag{4}$$

where all arguments are the same as in equation (3) and T and L are the apparent rupture duration and the rupture length, respectively. The difference in observed rupture duration, e.g., for unilateral rupture can be

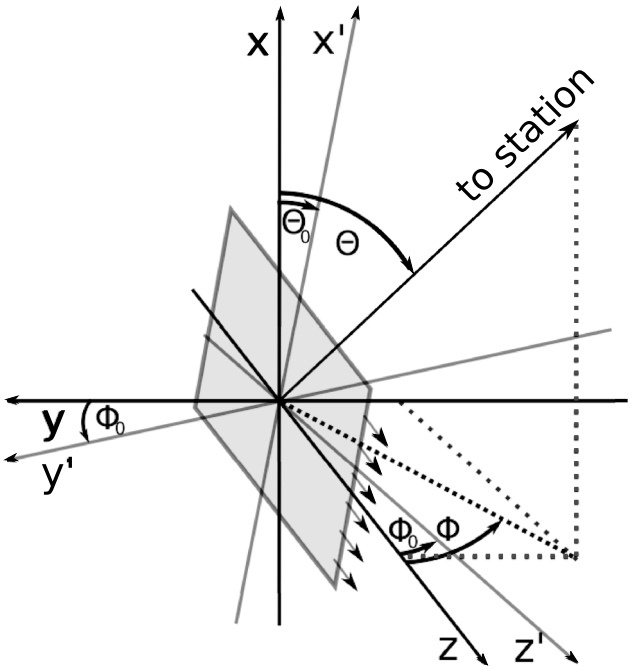

Figure 2. Coordinate system after *Savage* [1965] which was used to describe a propagating rupture for strike-slip and dip-slip dislocations. The vertical axis (X) is the depth axis. The small arrows depict the rupture direction on the fault plane (gray). The primed axes describe the orientation of the rupture plane. ϕ_0 is the rotation around the X axis, and θ_0 is the rotation around the plane normal, the Y' axis. Note that although ϕ is defined counterclockwise in the original publication, as it is drawn here, equation (3) also allows to use the azimuth instead.

substantial. Assuming a rupture velocity of $v_r = 0.8 \cdot c$ and defining a rupture duration $T_0 = L/v_r$, one obtains possible apparent rupture durations between $T = T_0 \cdot (1 \pm 0.8)$ for stations in backward and forward direction of the rupture, respectively.

4. Processing

We first identify pairs of events which are suitable for the EGF analysis by calculating their waveform similarity and interevent distance. We restrict our similarity analysis to the deepest borehole sensor (OT2) which is closest to the induced seismicity cloud and most sensitive to minor variations of seismic waveforms. Waveform similarity is determined for all possible combinations of event pairs by calculating maximum normalized cross-correlation coefficients, *cc*, for a seismogram window of 0.6 s length which includes both the *P* and the *S* phase at OT2, in the frequency band 1–60 Hz. We use the arithmetic mean of the cross-correlation coefficients on all three sensor components and only consider event pairs with $cc > 0.8$. For the application of the EGF method we additionally require a minimum magnitude difference between events of each event pair of $\Delta M = 0.6$ allowing on the one hand the identification of a sufficient number of event pairs and on the other hand to uphold the delta pulse assumption. This results in a selection of 195 suitable event pairs whose larger event partners show a magnitude range of $0.90 \leq M_L \leq 2.35$.

In a second step we apply an EGF analysis procedure which is similar to the one described in *Li et al.* [1995]. We first cut 2 s time windows of the *S* phase from the three-component displacement seismograms. In the next step zeroes are added before and after the signal and a Fourier transform is performed. In the spectral division the smaller EGF events are used in the denominator, and thus, we high cut all spectra at 100 Hz to reduce the effect of high-frequency noise. The spectra are slightly smoothed by a Gaussian filter to further ensure the stability of the spectral division [*Mueller*, 1985; *Li et al.*, 1995]. Next, the amplitude spectra of the two partner events are divided, and their phase spectra are subtracted. The resulting spectrum is then back transformed into time domain. Ideally, the procedure is stable on all three components at each record; however, to ensure good quality, we compare the three componentwise reconstructed RSTFs and in case of a good match they are averaged to enhance stability further [cf. *Dreger et al.*, 2007; *Harrington and Brodsky*, 2009]. If one of the

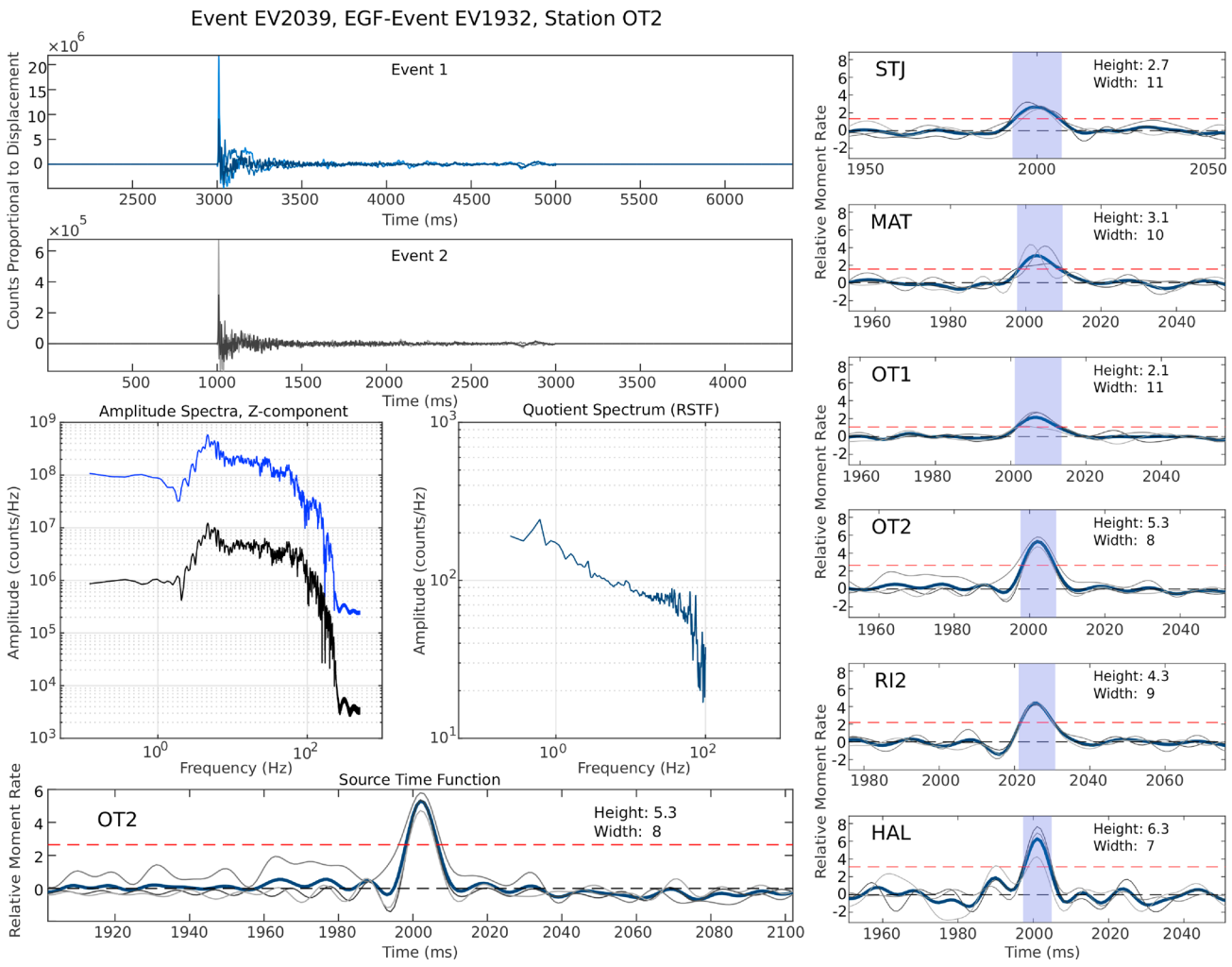

Figure 3. (left column) Reconstruction of the relative source time function (RSTF) for the event Ev_{2039} and its EGF event Ev_{1932} for station OT2. The two top panels show the three-component records of the corresponding *S* phases (note the amplitude difference). Below, the *z* component amplitude spectra and their quotient are shown in respective colors. At the bottom, RSTFs in time domain for each component (gray) and their average (blue) is shown in units of relative moment rate. Dashed lines represent the background amplitude level and the value of half the maximum height at which the pulse width is measured (FWHM). (right column) RSTFs at all six Basel stations. Note the consistent variation of width and height due to the directivity effect, indicated by the blue bar.

RSTF components cannot be properly reconstructed it is discarded. Thus, at least two components contribute to the result. Amplitude and width of the resulting RSTF are then computed. A data example illustrating the processing and the systematic variation of amplitude and width of the RSTFs with station azimuth is shown in Figure 3.

A rough estimate using both *Eshelby* [1957] (circular) or *Knopoff* [1958] (rectangular, unilateral) rupture models, and assuming stress drops of 1–10 MPa [e.g., *Goertz-Allmann et al.*, 2011], yields source time function widths (durations) of a few tens of milliseconds, suggesting that the sampling rate of 1 kHz is sufficient to resolve directivity at this scale ($0.90 \leq M_L \leq 2.35$). In spite of the fact that the variation of pulse width is in principle resolvable, we follow the approach of *Jost et al.* [1998] who found that the fit using the RSTF amplitudes (equation (3)) rather than the durations (equation (4)) produces the more reliable results. The measured amplitude values at all stations are compared, and unreasonable small and large data points are removed by neglecting values smaller than one fifth of the mean of all measured amplitudes, which is approximately the minimum expected amplitude based on a rupture velocity of 0.8 times the *S* wave velocity. The upper limit is empirically set to 5 times the mean amplitude. We require a minimum number of five RSTF amplitude values for the fit. We fit both the unilateral and the bilateral implementations of equation (3), and we choose the result with the lower RMS. Since we consider a multivariable problem with only few measurement values, we assume that the fault plane is subvertical and that the rupture within this plane propagates horizontally

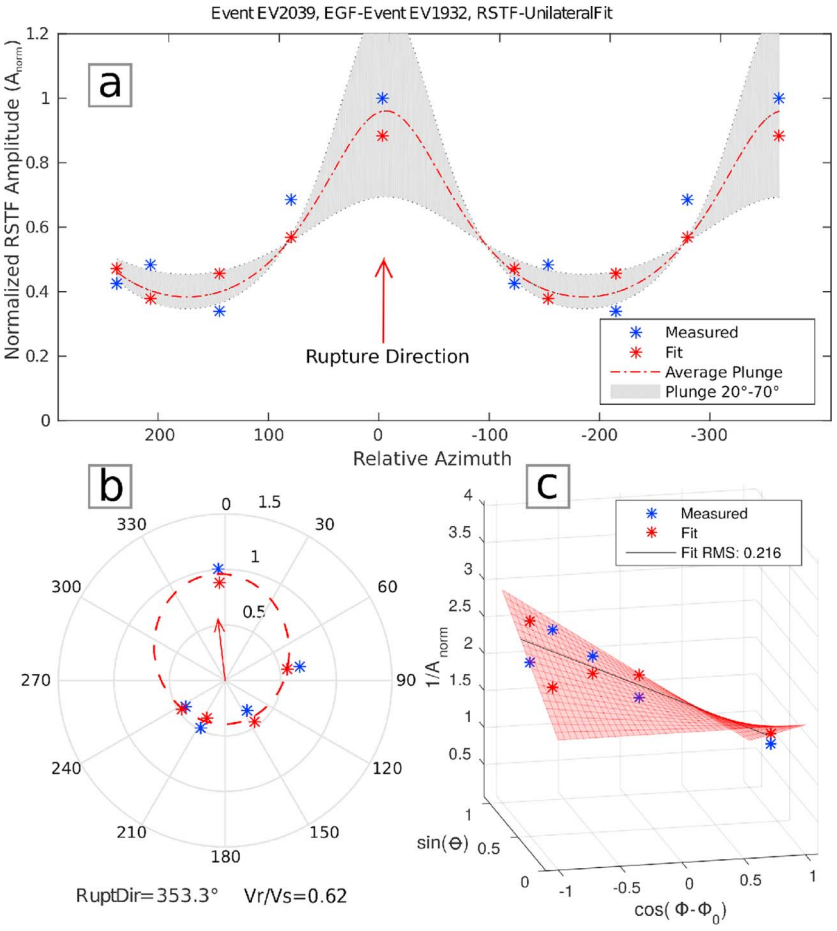

Figure 4. Graphical representations of the amplitude-directivity fit. For the fit formula (3) is rearranged in the following way: $[1/A_i = a_i - b_i(\cos^i(\phi - \phi_0) * \sin^i(\theta))]$. Further is $b^i/a^i = (v_r/v_s)^{1/2}$. Measured values are blue. Red asterisks show fitted amplitude values including the respective station plunge correction. For a simplified graphical representation a hypothetical average plunge is computed for all stations, allowing a representation of the fitted data as the (a) red curve or in (b) planar view. The strong influence of the plunge is indicated by a gray corridor of plunge values of 20° – 70°. Since all stations have individual plunges, the red asterisks do not lie on the curve. (c) The fitting result can alternatively be visualized by a surface through the red data points.

(cf. Figure 2); hence, θ_0 is set to zero. This is a reasonable assumption, since the predominant mechanisms in the reservoir are strike-slip and oblique events close to strike slip [*Kraft and Deichmann*, 2014], which implies that the fracture growth is due to shear stress and that the rupture propagates in the direction of slip (fracture mode II). As the directivity effect is a 3-D phenomenon, we must account for the take off angle of the ray at the source, the plunge θ, between individual stations and the rupture. For this reason we use the take off angle from the localization study, performed using the grid search-based, probabilistic earthquake localization code *NonLinLoc* [*Lomax et al.*, 2000]. Subsequently, the fitting procedure from *Li et al.* [1995] must be extended in order to comprise the individual station plunges. For this multivariable minimization problem we use the nonlinear problem solver fmincon provided in MATLAB®. It minimizes the misfit between measured data and the given model of amplitude variation and yields the rupture directivity direction. Graphically, the problem can be represented as a surface through the amplitude data (cf. Figure 4). In the teleseismic context the impact of the plunge is often ignored [e.g., *Kanamori and Anderson*, 1975] because of the large epicentral distances between stations and events and the comparatively small source depth. The fit then yields the rupture velocity ratio v_r/v_s and the direction of the rupture ϕ_0. It is difficult to quantify the uncertainty of even single EGFs and subsequently the quality of the direction estimates. In a detailed study *Abercrombie* [2015] concluded that a minimum of five records or stations per event are sufficient for a reasonable source parameter reconstruction with less than 10% uncertainty. In our case this issue was addressed by testing our algorithm using

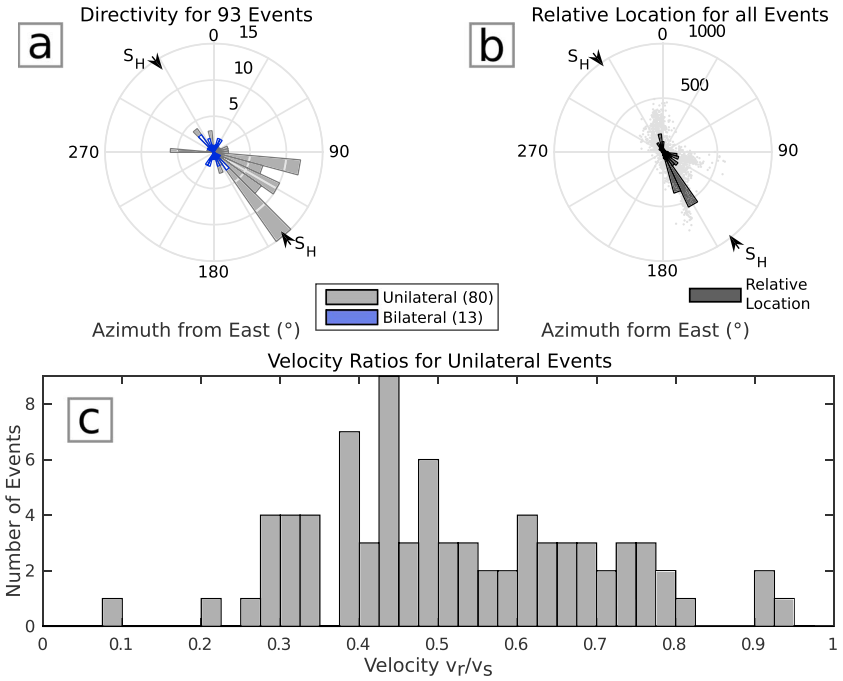

Figure 5. (a) Distribution of rupture directivity estimates. Note that the unilateral solutions predominate. There exists a clear trend in southeast direction. S_H is the direction of the maximum horizontal stress. (b) Diagram of number of event locations relative to the borehole. (c) Velocity estimates relative to *S* wave velocity. Note the broad variation of velocities. Note also that the velocity estimates only represent the horizontal rupture velocity.

synthetic Haskell-type ruptures which were modeled using a FD algorithm [*Saenger et al.*, 2000]. For the tests we first used a circle of 12 azimuthally evenly distributed stations which produced results with directivity estimates with less than 2% error. In a second step we modeled the station-event geometry of the Basel EGS and found that rupture directivity and velocities were reconstructed reliably with estimates that showed less than 5% deviation from the modeled rupture directions.

5. Results

For 93 out of 195 events we find robust signatures of azimuth-dependent amplitude variations which allow to compute rupture directivity and rupture speed. A statistical overview of the distribution of events with directional behavior is shown in Figure 5. Unilateral behavior seems to prevail (80 events), and only a small group of events (13 events) is best fit as bilateral. Therefore, we decided to focus here on the events with unilateral directivity estimates. We observe that the rupture directivity estimates show a clear and dominant trend in southeast direction (Figure 5a). Only few events rupture in the opposite direction (toward northwest), and contributions of other directions are also relatively small. For comparison Figure 5b shows the distribution of hypocenters of all event locations at Basel. Both distributions in Figures 5a and 5b are partly consistent. The fit routine also produces rupture velocity estimates (for further details see *Li et al.* [1995]). We find values for rupture velocities normalized to the *S* wave speed, v_r/v_s, that range from 0.1 to 0.9. Note, however, that the velocities are true velocities only if the rupture direction is horizontal. The spatial overview of the estimated directivity for the 80 unilateral events is given in Figure 6, where rupture directivity is indicated by an arrow at the hypocenter location of each event. In the vicinity of the open hole section of the borehole (red line), the rupture directivity follows no clear trend, and rupture directions different from southeast or northwest are observed. At a greater distance directivity shows a preferred orientation and is directed mainly toward the southeast direction. In the spatiotemporal event domain (Figure 7), the seismicity can be separated into two phases. No clear trend in the rupture directivity is observed during the first 3 days. Here rupture directivity varies broadly and shows an only weak tendency toward northwest or southeast. Events in this phase are located close to the borehole. The second phase, starting at day 3, covers events that show directivity almost exclusively toward southeast. This phase includes the majority of the events used in this study. It is notable

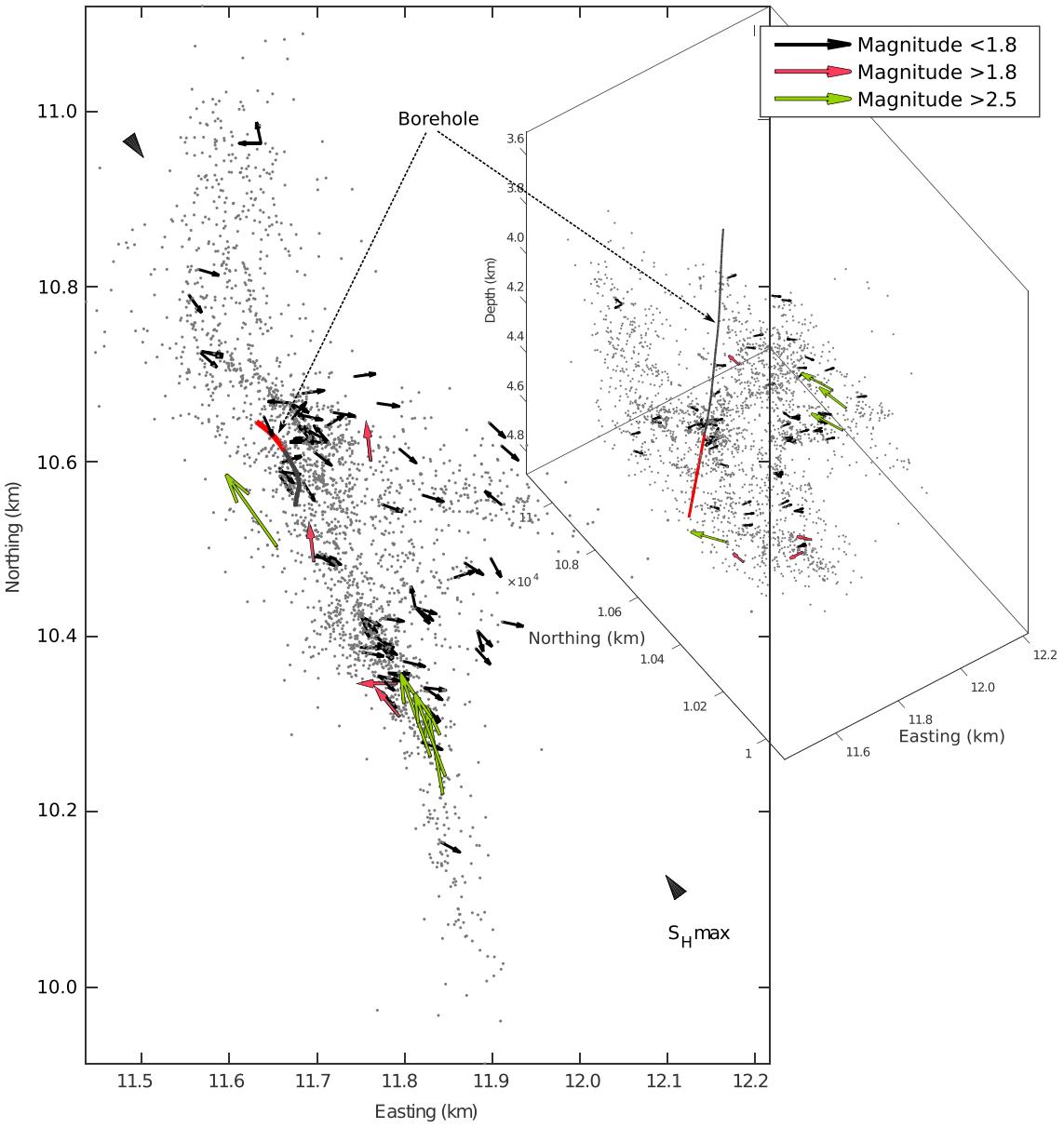

Figure 6. Rupture directivity and microseismic cloud in map view and in side view. Arrows represent rupture directivity estimates. Location of nucleation (hypocenter) is at the tail of each arrow. Events with $M_L < 1.8$ are colored black. Events with $M_L \geq 1.8$ are color coded red. These are the largest events within this study, showing stable solutions under EGF analysis. Using Back Projection Imaging *Folesky et al.* [2015] reconstructed the paths of the largest events in the reservoir ($3.1 \leq M_L \leq 3.4$). The respective rupture directions are shown in green. Note that the rupture directions of the large events do not follow the main direction trend but rather point inward the microseismic cloud and toward the borehole.

that the largest events from this study ($M \geq 1.8$) occurred during a short period slightly before and after the shut-in of the Basel stimulation. The rupture directions of these events do not follow the main trend but point in the opposite direction, i.e., back inside the reservoir and toward the injection source. The spatial distance of the largest events from the borehole is relatively large (about 230 m–450 m). The map and side view in Figure 6 reveal that all four large events (red) are located close to the boundaries of the stimulated volume, which was even smaller than displayed by the time of their occurrence.

The second half of events that were analyzed in this study do not show significant or consistent enough attributes for a directivity estimate. This could be due to one of the following reasons:

1. The rupture process is not strongly directional. This is the case for circular faults rupturing in all directions within the fault plane almost simultaneously, or alternatively an instantaneous rupture on a fault plane.

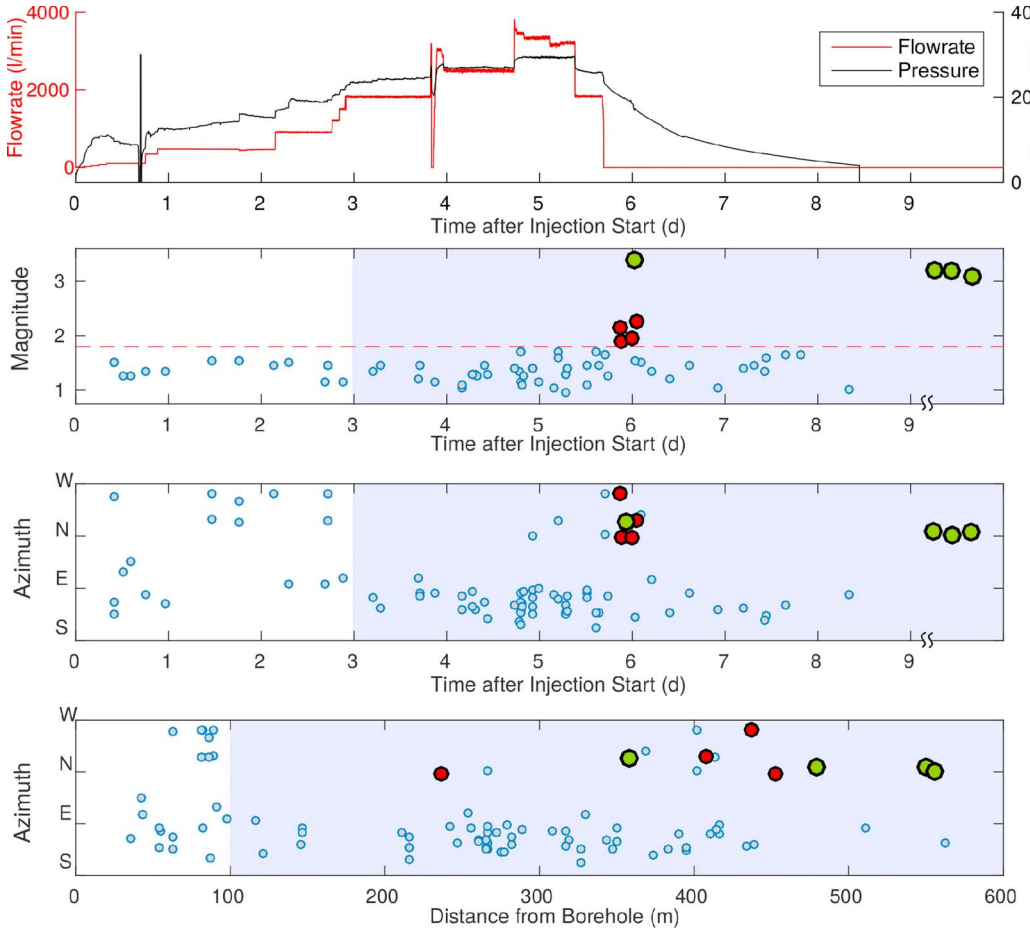

Figure 7. Magnitude and rupture directivity for 80 events with stable directivity estimates. The observed directivity can be divided into two phases. First (white) is the injection phase until day 3, where no significant trend of directivity is found. Second (blue) is the phase after day 3, where a clear trend of directivity toward the southeast is observed. Spatial partitioning corresponds to the temporal phases one and two. In the vicinity of the open hole no clear trend of directivity is found. Beginning at 100 m distance a clear southeast trend occurs. The four largest events ($M > 1.8$) from this study are color coded in red. Green are the largest events at Basel ($M > 3.2$, directivity from a Back Projection study by *Folesky et al.* [2015]). All eight large events do not obey the prevalent directivity, and their distance from the borehole is relatively large (230–560 m).

2. The directivity is not resolvable with our approach due to noise or inadequate receiver-rupture geometry. In our case a vertically propagating rupture on a vertical fault would constitute such a scenario.
3. If several subsequent events interfere the rupture becomes complex. Each subevent may be directional, but their superposition cancels out or disturbs the observation of the directivity.

Most of the nondirectional events fall into the above categories 1 and 2, but we also found events which clearly exhibit rupture complexities. Their RSTFs are shown for four azimuthally well distributed seismic receivers in Figure 8. All RSTFs exhibit complexities, which clearly shows they are not single pulse-like functions. Instead, they are characterized by two or even three distinct pulses, which are consistently observed at all stations. Time separation between individual pulses is of the order of 15 ms and is constant for each subevent from station to station, which is an unambiguous indication for colocation of the subevents. The corresponding seismograms for event EV0983 at stations OT2 and RI2 are shown in Figure 9. At receiver OT2, which is located at 2.7 km depth (cf. Figure 1), closest to the microseismic event cloud and therefore records the highest frequencies, the individual subevents are well discernible in the seismograms. The remaining receivers are installed at shallower depths at 320–1200 m below the surface in sedimentary layers, which is why individual subevents are barely identifiable in the waveforms at RI2. The complexity of the rupture process is only resolved by the RSTF at those stations. In all four cases the largest subevent shows a systematic variation of amplitude and duration. For event EV2537, the smaller subevents (blue in Figure 8) exhibit a

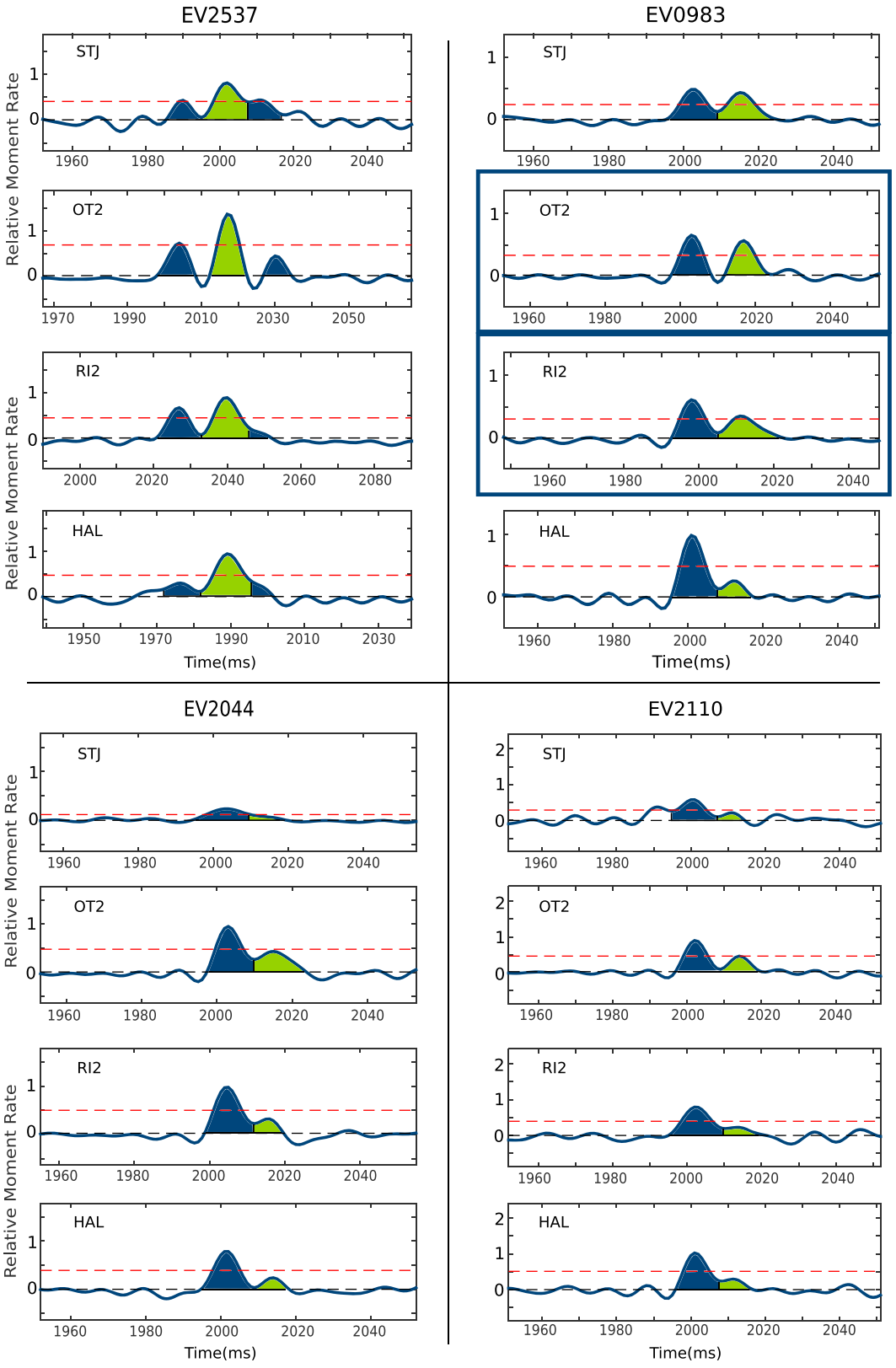

Figure 8. RSTFs of four events at the Basel EGS site at four different receivers, respectively. The RSTFs show complex forms, consistently. Distinct pulses are color coded for enhanced visibility. Each pulse can be interpreted as a rupture or one phase of rupture. Multiple pulses would then constitute either multiple ruptures or one complex, multiphase rupture. The variation of amplitudes indicates a directivity in the rupture process but can be divergent between pulses.

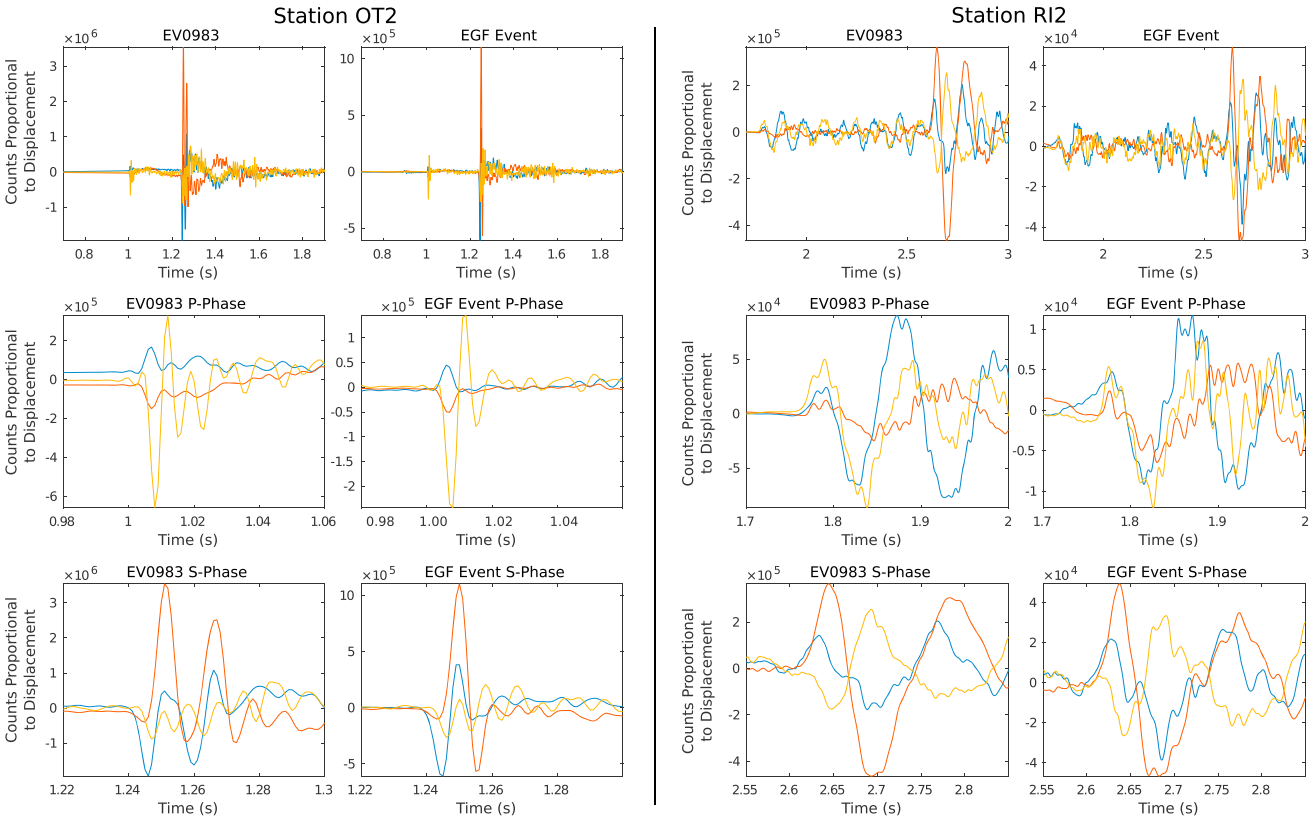

Figure 9. Seismograms for the event EV0983 and its EGF as observed at the two stations (left columns) OT2 and (right columns) RI2. The corresponding RSTFs are framed in blue in Figure 8. (top row) The three-component displacement waveforms. (middle row) A zoom in on the *P* phase. (bottom row) The *S* phase is shown. Note that the EGF waveform at OT2 consist of one pulse or sinusoid per phase. In contrast, the larger event shows a superposition of two wave trains of similar type. At receiver RI2, which resembles lower frequency content, this effect is much harder to identify; however, the RSTF reconstruction in Figure 8 reliably identifies the same two distinct pulses as for station OT2.

similar station-dependent variation of amplitude as the main pulse (green in Figure 8). In the other examples subevents are not coherent with the largest pulse (see especially EV0983 in Figure 8). Given the small time delay between the subevents of about 15 ms, and estimated rupture radii for the examined $M_L \sim 1$ events in the order of tens of meters (assuming stress drop values in the range of 1–10 MPa [*Goertz-Allmann et al.*, 2011]), the subevents probably rupture different parts of the same fault patch and are separated no more than a few tens of meters. Variations of rupture directivity, as evidenced by the RSTF, then indicate small-scale heterogeneity, i.e., asperities, along the ruptured segment. Complexities in the rupture process are principally known to exist in large and medium-sized earthquakes [*Velasco et al.*, 1994; *Li et al.*, 1995], and *Dreger et al.* [2007] and *Taira et al.* [2015] also found evidence for complex rupture processes, i.e., heterogeneous slip distribution and rupture directivity in small natural earthquakes. However, this has rarely been observed for fluid-induced microseismic events.

6. Discussion

The observation of unilateral and bilateral directivity and the resolution of rupture complexities at Basel demonstrate that not only directivity persists in microseismic events but also that heterogeneities can be relevant for small-scale ruptures. These observations contradict the customary approach in microseismic studies which assumes a nondirectional rupture process, where circular rupture models [*Brune*, 1970; *Boatwright*, 1980] are invoked to infer source properties including stress drop or source radius. These models often ignore the influence of rupture directivity by averaging over the entire focal sphere [*Kaneko and Shearer*, 2014].

In the following we discuss the observed directivity and its spatiotemporal characteristics at the Basel EGS in more detail. Figures 6 and 7 show that rupture directivity of events in the close vicinity of the open hole

section follows no preferential direction. Here the event-density is generally highest, and we find the same trend for events occurring in the early phase of the experiment, before day 3. We consider the decrease of effective normal stress by the increase of the pore pressure due to injection as the controlling mechanism for the rupture process at the early stage. Close to the borehole the stress perturbation is largest, possibly causing preexisting cracks of arbitrary orientation to fail. Starting with day 3 and a distance of about 100 m, the rupture directivity exhibits a different but clear trend: The events rupture preferably toward the southeast. Only few events rupture in the exact opposite direction. Almost no event exhibits directivity toward northeast or southwest. Figure 5 illustrates that this behavior corresponds to the shape of the microseismic cloud, which itself shows the most hypocenter locations and its largest extend in south-south-east direction, relative to the borehole. It seems that the increased number of event occurrences toward south-south-east and the distribution of rupture directivity could be associated.

The direction of maximum horizontal stress, derived by borehole breakouts [*Häring et al.*, 2008], is in direction 144°, and thus, only a small part of rupture directions is well oriented for optimal shear failure conditions (approximately 22° – 30° relative to S_{Hmax}). It seems that the orientation and extension of the microseismic cloud is strongly influenced by the preexisting faults and structures at the site, which are reported to be a network of small substructures rather than one main fault [*Kraft and Deichmann*, 2014]. We observe not only an increasingly clearer trend of orientation but also of directivity of the ruptures with distance to the borehole, suggesting that it is probable that either stress field or structure overtake the control over the rupture process at larger distances from the borehole, as the influence of the increased pore pressure due to the water injection decreases [*Catalli et al.*, 2013].

A different and important observation relates to the largest ($M \geq 1.8$) events within this data set (red colored in Figures 6 and 7). These events do not follow the rupture direction trend of south-south-east but point in the opposite direction, back inside the microseismic cloud. *Folesky et al.* [2015] analyzed the rupture behavior of the four largest ($3.2 \leq M_L \leq 3.4$) induced events at the Basel EGS site, using the method of microseismic rupture propagation imaging. Their results are inserted in both figures in green. Unfortunately, it is impossible to apply the EGF method to these events, because they are isolated and no corresponding EGF events could be found. The observations of both studies coincide nicely. The large events at the Basel reservoir appear to rupture from their nucleation point, close to the rim of the microseismic cloud, back inside into the stimulated volume and toward the injection source. The occurrence time corridor of most of the relatively large events is shortly before and after the stop of injection. The occurrence of relatively large events close to the edges of the stimulated volume has been reported previously for other enhanced geothermal systems [*Majer et al.*, 2007]. To explain such a behavior, e.g., *Goertz-Allmann and Wiemer* [2012] proposed a geomechanical model based on an inverse relationship between *b* value and differential stress. A corresponding observation is made in a local seismicity study on aftershock distribution by *Elst and Shaw* [2015]. They report that larger aftershocks tend to occur farther away from the centroid of previous activity than smaller aftershocks which is interpreted as a feature of stress relaxation on the main rupture patch. The direction of rupture, however, is not included in these studies.

An explanation of the observed inward pointing rupture directions of the largest events at Basel is provided by *Shapiro et al.* [2011]. They found that the maximum expected magnitude is related to the geometry of the rock volume and that a fault is more probable to rupture if its surface is located mostly inside the stimulated volume. This concept anticipates that ruptures are orientated mainly in direction toward the injection source — exactly what we observe for the largest induced events at Basel.

7. Conclusions

Based on the well-balanced azimuthal coverage of the seismic monitoring system at the Basel-enhanced geothermal system and the high quality of the recorded seismograms, we have performed a comprehensive study on rupture directivity of microseismic events in the magnitude range $0.90 \leq M_L \leq 2.35$. Using an empirical Green's function method, we observe clear signatures of directivity by systematic amplitude variations of the relative source time functions for about half of the event pairs suitable for this study. This demonstrates that rupture directivity persists down to small, $M_L \sim 1$ fluid-induced events. For few events we identify complex rupture behavior indicating the existence of asperities and heterogeneities at a scale of a few tens of meters, similar to the observations from natural seismicity in California by *Dreger et al.* [2007] and *Taira et al.* [2015]. This implies that the exact estimation of source properties is more complex than generally

assumed since rupture complexity and directivity influence the radiation pattern and spectra significantly [*Kaneko and Shearer*, 2015]. Our results are also consistent with the observations of rupture complexities for mining-induced microearthquakes [*Yamada et al.*, 2005; *Kwiatek et al.*, 2011], supporting the concept of self-similar behavior of the rupture process.

The computed rupture directions show a dependence on distance from the injection source and size of the events. The relative diversity of rupture directions close to the injection source and the increasing alignment of rupture directions with larger distances coincide with the decreasing effect of the pore pressure with larger distances, which also seems to control the observed stress drop [*Goertz-Allmann et al.*, 2011] and role of Coulomb stress changes [*Catalli et al.*, 2013] at Basel. The distinct behavior of the largest events, which rupture preferentially backward to the injection source agrees with independent observations from direct rupture imaging of $M_L \geq 3.2$ events at Basel [*Folesky et al.*, 2015]. These events also occur close to the boundary of the stimulated volume. The findings of this study corroborate the model of *Shapiro et al.* [2011] on the maximal expectable magnitude which is based on the assumption that the potential rupture surface needs to be located mainly inside the stimulated reservoir.

Acknowledgments
We thank the sponsors of the PHASE consortium for supporting the research presented in this paper. We are especially grateful to GeoExplorers Ltd. for providing the seismic waveform data. Data, including seismic waveforms for the EGF pairs, used in this study can be obtained upon request from the corresponding author at jonas.folesky@geophysik.fu-berlin.de. We greatly appreciate the detailed and constructive comments from Martin Mai, an anonymous reviewer, and the Editors who helped us to significantly increase the quality of the paper.

References

Abercrombie, R. E. (2015), Investigating uncertainties in empirical Green's function analysis of earthquake source parameters, *J. Geophys. Res. Solid Earth*, *120*(6), 4263–4277, doi:10.1002/2015JB011984.

Ben-Menahem, A. (1961), Radiation of seismic surface- waves from finite moving sources, *Bull. Seismol. Soc. Am.*, *51*, 401–435, doi:10.1029/91JB01936.

Boatwright, J. (1980), A spectral theory for circular seismic sources: Simple estimates of source dimension, dynamic stress drop, and radiated seismic energy, *Bull. Seismol. Soc. Am.*, *70*(1), 1–27.

Boatwright, J. (2007), The persistence of directivity in small earthquakes, *Bull. Seismol. Soc. Am.*, *97*(6), 1850–1861, doi:10.1785/0120050228.

Boatwright, J., and D. M. Boore (1982), Analysis of the ground accelerations radiated by the 1980 Livermore Valley earthquakes for directivity and dynamic source characteristics, *Bull. Seismol. Soc. Am.*, *72*(6A), 1843–1865.

Brune, J. N. (1970), Tectonic stress and the spectra of seismic shear waves from earthquakes, *J. Geophys. Res.*, *75*(26), 4997–5009, doi:10.1029/JB075i026p04997.

Catalli, F., M. Meier, and S. Wiemer (2013), The role of Coulomb stress changes for injection-induced seismicity: The Basel enhanced geothermal system, *Geophys. Res. Lett.*, *40*(72–77), doi:10.1029/2012GL054.147.

Deichmann, N., and D. Giardini (2009), Earthquakes induced by the stimulation of an enhanced geothermal system below Basel (Switzerland), *Seismol. Res. Lett.*, *80*(5), 784–798, doi:10.1785/gssrl.80.5.784.

Dinske, C., and S. Shapiro (2010), Interpretation of microseismicity induced by timpe-dependent injection pressure, *SEG Expanded Abstr.*, *29*, 2125–2129, doi:10.1190/1.3513.264.

Dreger, D., R. M. Nadeau, and A. Chung (2007), Repeating earthquake finite source models: Strong asperities revealed on the San Andreas Fault, *Geophys. Res. Lett.*, *34*(23), L23302, doi:10.1029/2007GL031353.

Dyer, B., U. Schanz, T. Spillmann, F. Ladner, and M. Häring (2010), Application of microseismic multiplet analysis to the Basel geothermal reservoir stimulation events, *Geophys. Prospect.*, *58*(5), 791–807, doi:10.1111/j.1365-2478.2010.00902.x.

Elst, N. J., and B. E. Shaw (2015), Larger aftershocks happen farther away: Nonseparability of magnitude and spatial distributions of aftershocks, *Geophys. Res. Lett.*, *42*(14), 5771–5778, doi:10.1002/2015GL064734.

Eshelby, J. D. (1957), The determination of the elastic field of an ellipsoidal inclusion, and related problems, *Proc. R. Soc. London, Ser. A*, *241*, 376–396, doi:10.1098/rspa.1957.0133.

Folesky, J., J. Kummerow, and S. A. Shapiro (2015), Microseismic rupture propagation imaging, *Geophysics*, *80*(6), WC107–WC115, doi:10.1190/geo2014-0572.1.

Frankel, A., and H. Kanamori (1983), Determination of rupture duration and stress drop for earthquakes in Southern California, *Bull. Seismol. Soc. Am.*, *73*(6A), 1527–1551.

Frankel, A., J. Fletcher, F. Vernon, L. Haar, J. Berger, T. Hanks, and J. Brune (1986), Rupture characteristics and tomographic source imaging of ML 3 earthquakes near Anza, Southern California, *J. Geophys. Res.*, *91*(B12), 12,633–12,650, doi:10.1029/JB091iB12p12633.

Goertz-Allmann, B. P., and S. Wiemer (2012), Geomechanical modeling of induced seismicity source parameters and implications for seismic hazard assessment, *Geophysics*, *78*(1), KS25–KS39, doi:10.1190/geo2012-0102.1.

Goertz-Allmann, B. P., A. Goertz, and S. Wiemer (2011), Stress drop variations of induced earthquakes at the Basel geothermal site, *Geophys. Res. Lett.*, *38*(9), doi:10.1029/2011GL047498.

Häring, M. O., U. Schanz, F. Ladner, and B. C. Dyer (2008), Characterisation of the Basel 1 enhanced geothermal system, *Geothermics*, *37*(5), 469–495, doi:10.1016/j.geothermics.2008.06.002.

Harrington, R. M., and E. E. Brodsky (2009), Source duration scales with magnitude differently for earthquakes on the San Andreas Fault and on secondary faults in Parkfield, California, *Bull. Seismol. Soc. Am.*, *99*(4), 2323–2334, doi:10.1785/0120080216.

Haskell, N. (1964), Total energy and energy spectral density of elastic wave radiation from propagating faults, *Bull. Seismol. Soc. Am.*, *54*(6A), 1811–1841.

Jost, M. L., T. Büßelberg, O. Jost, and H.-P. Harjes (1998), Source parameters of injection-induced microearthquakes at 9 km depth at the KTB Deep Drilling site, Germany, *Bull. Seismol. Soc. Am.*, *88*(3), 815–832.

Kanamori, H., and D. L. Anderson (1975), Theoretical basis of some empirical relations in seismology, *Bull. Seismol. Soc. Am.*, *65*, 1073–1095.

Kane, D. L., P. M. Shearer, B. P. Goertz-Allmann, and F. L. Vernon (2013), Rupture directivity of small earthquakes at Parkfield, *J. Geophys. Res. Solid Earth*, *118*(1), 212–221, doi:10.1029/2012JB009675.

Kaneko, Y., and P. M. Shearer (2014), Seismic source spectra and estimated stress drop derived from cohesive-zone models of circular subshear rupture, *Geophys. J. Int.*, *197*(2), 1002–1015, doi:10.1093/gji/ggu030.

Kaneko, Y., and P. M. Shearer (2015), Variability of seismic source spectra, estimated stress drop, and radiated energy, derived from cohesive-zone models of symmetrical and asymmetrical circular and elliptical ruptures, *J. Geophys. Res. Solid Earth*, *120*(2), 1053–1079, doi:10.1002/2014JB011642.

Knopoff, L. (1958), Energy release in earthquakes, *Geophys. J. Int.*, *1*(1), 44–52, doi:10.1111/j.1365-246X.1958.tb00033.x.
Kraft, T., and N. Deichmann (2014), High-precision relocation and focal mechanism of the injection-induced seismicity at the Basel EGS, *Geothermics*, *52*, 59–73, doi:10.1016/j.geothermics.2014.05.014.
Kummerow, J., S. Shapiro, H. Asanuma, and M. Häring (2011), *Application of an Arrival Time and Cross Correlation Value-Based Location Algorithm to the Basel 1 Microseismic Data*, Expanded Abstracts, EAGE 73nd annual meeting and technical exhibition, Vienna.
Kummerow, J., S. Shapiro, H. Asanuma, and M. Häring (2014), *Observation and Signatures of Injection-Induced Repeating Earthquake Sequences*, Expanded Abstracts, EAGE 76th annual meeting and technical exhibition, Vienna.
Kwiatek, G., et al. (2011), Source parameters of picoseismicity recorded at Mponeng deep gold mine, South Africa: Implications for scaling relations, *Bull. Seismol. Soc. Am.*, *101*(6), 2592–2608, doi:10.1785/0120110094.
Li, Y., C. Doll, and M. N. Toksöz (1995), Source characterization and fault plane determination for MbLg = 1.2 to 4.4 earthquakes in the Charlevoix Seismic Zone, Quebec, Canada, *Bull. Seismol. Soc. Am.*, *85*(6), 1604–1621.
Lomax, A., J. Virieux, P. Volant, and C. Berge-Thierry (2000), Probabilistic earthquake location in 3D and layered models, in *Advances in seismic event location*, pp. 101–134, Springer, Kluwer, Amsterdam., doi:10.1007/978-94-015-9536-0_5
Madariaga, R. (1976), Dynamics of an expanding circular fault, *Bull. Seismol. Soc. Am.*, *66*(3), 639–666.
Majer, E. L., R. Baria, M. Stark, S. Oates, J. Bommer, B. Smith, and H. Asanuma (2007), Induced seismicity associated with enhanced geothermal systems, *Geothermics*, *36*(3), 185–222, doi:10.1016/j.geothermics.2007.03.003.
McGuire, J. J., L. Zhao, and T. H. Jordan (2002), Predominance of unilateral rupture for a global catalog of large earthquakes, *Bull. Seismol. Soc. Am.*, *92*(8), 3309–3317, doi:10.1785/0120010293.
Mori, J. (1993), Fault plane determinations for three small earthquakes along the San Jacinto fault, California: Search for cross faults, *J. Geophys. Res.*, *98*(B10), 17,711–17,722, doi:10.1029/93JB01229.
Mueller, C. S. (1985), Source pulse enhancement by deconvolution of an empirical Green's function, *Geophys. Res. Lett.*, *12*, 33–36, doi:10.1029/GL012i001p00033.
Reshetnikov, A., J. Kummerow, H. Asanuma, M. Häring, and S. A. Shapiro (2015), Microseismic reflection imaging and its application to the Basel geothermal reservoir, *Geophysics*, *80*(6), WC39–WC49, doi:10.1190/geo2014-0593.1.
Saenger, E. H., N. Gold, and S. A. Shapiro (2000), Modeling the propagation of elastic waves using a modified finite-difference grid, *Wave Motion*, *31*(1), 77–92, doi:10.1016/S0165-2125(99)00023-2.
Savage, J. C. (1965), The effect of rupture velocity upon seismic first motions, *Bull. Seism. Soc. Am.*, *55*, 263–275.
Shapiro, S. A., O. S. Krüger, C. Dinske, and C. Langenbruch (2011), Magnitudes of induced earthquakes and geometric scales of fluid-stimulated rock volumes, *Geophysics*, *76*(6), WC55–WC63, doi:10.1190/geo2010-0349.1.
Taira, T., D. S. Dreger, and R. M. Nadeau (2015), Rupture process for micro-earthquakes inferred from borehole seismic recordings, *Int. J. Earth Sci.*, *104*(6), 1499–1510, doi:10.1007/s00531-015-1217-8.
Vallée, M. (2004), Stabilizing the empirical Green function analysis: Development of the projected Landweber method, *Bull. Seismol. Soc. Am.*, *94*(2), 394–409, doi:10.1785/0120030017.
Velasco, A. A., C. J. Ammon, and T. Lay (1994), Recent large earthquakes near Cape Mendocino and in the Gorda plate: Broadband source time functions, fault orientations, and rupture complexities, *J. Geophys. Res.*, *99*, 711–728, doi:10.1029/93JB02390.
Yamada, T., J. J. Mori, S. Ide, H. Kawakata, Y. Iio, and H. Ogasawara (2005), Radiation efficiency and apparent stress of small earthquakes in a South African gold mine, *J. Geophys. Res.*, *110*, B01305, doi:10.1029/2004JB003221.

Chapter 5

Estimating Rupture Directions from Local Earthquake Data Using the IPOC Observatory in Northern Chile

- Local seismicity in the rupture area of the 2014 M_W 8.1 Iquique event is analyzed for rupture directivity using a P wave polarization-based stacking approach.
- Applicability of the technique at this site for events of minimum magnitude of $M_L \approx 5$ is demonstrated.
- Unilateral rupture behavior is found for 60 $M_L \geq 5$ events. The directivity shows a preferred orientation toward east, southeast, and south.

This article has been published in Seismological Research Letters:
Folesky, J., Kummerow, J., Asch, G., Schurr, B., Sippl, C., Tilmann, F., & Shapiro, S. A. (2018). Estimating rupture directions from local earthquake data using the IPOC observatory in Northern Chile. Seismological Research Letters, https://doi.org/10.1785/0220170202

Chapter 6

Patterns of Rupture Directivity of Subduction Zone Earthquakes in Northern Chile

- Comprehensive study on rupture directivity of seismicity at the rupture region of the 2014 M_W 8.1 Iquique earthquake.
- Directivity is computed for 351 events with $2.6 \leq M_L \leq 5.3$ applying an empirical Green's function approach.
- The results display a strongly pronounced preference of rupture directivity parallel to the plate convergence direction (down-dip).
- The observed preferred rupture directivity is attributed to the bimaterial effect between the two media at the subduction interface.

This article has been accepted for publication in Journal of Geophysical Research - Solid Earth and is currently in production, https://doi.org/10.1029/2018JB016331

Patterns of Rupture Directivity of Subduction Zone Earthquakes in Northern Chile

Jonas Folesky[1], **Jörn Kummerow**[1], **Serge A. Shapiro**[1]

[1]Freie Universität Berlin, Department of Geophysics, Berlin, Germany

Abstract

We perform a systematic directivity analysis of local seismic events west off the coast of northern Chile. An empirical Green's function technique is applied to a selection of events from a time period from 2008 to 2016 in the vicinity of the rupture area of the M_W 8.1 Iquique megathrust earthquake in 2014. We compute rupture directivity for 293 events of magnitudes between M_L 2.6 and M_L 5.3. We find a strong preference of rupture orientations sub-parallel to the convergence vector of the Nazca plate relative to the South-American plate. The preferred rupture direction is down-dip. We speculate that the reason for the dominating rupture direction could be a lateral limitation of available rupture directions by the repeating earthquake-like nature of the observed events combined with a material contrast at the subduction interface which, according to the bimaterial effect, favors the down-dip rupture direction.

Plain Language Summary

We perform a systematic analysis of the direction of the rupture process of earthquakes in northern Chile. To assess the direction of the earthquake ruptures we use a technique called empirical Green's function analysis. Here, a pair of collocated, highly similar earthquakes is used to approximate and then remove the influence of the travel path of the earthquake waves between source and station. Thus, only the signature of the rupture process of the larger event remains, for which we can identify the direction of rupture. We analyze events in a time period from 2008 to 2016 in the vicinity of the rupture area of the large M_W 8.1 Iquique earthquake in 2014 in northern Chile. We compute rupture directivity for events of magnitudes between M_L 2.6 and M_L 5.3. We find a strong preference of rupture directions which are oriented sub-parallel to the direction of the plate movement between the Nazca plate and the South-American plate. The preferred rupture direction is directed toward east. We speculate that the reason for the dominating rupture direction could be a limitation of available rupture directions by the special nature of the here analyzed events combined with a material contrast between the two plates.

Corresponding author: Jonas Folesky, jonas.folesky@geopyhsik.fu-berlin.de

1 Introduction

It is widely accepted that directivity of seismic events persists at multiple scales [*Boatwright*, 2007] and thus should be considered when detailed source characteristics are derived from spectral properties [e.g., *Kaneko and Shearer*, 2014, 2015].
Large earthquakes seem to show preferably unilateral rupture behavior [*McGuire et al.*, 2002] whereas rupture properties of smaller earthquakes are much less frequently analyzed. Rupture propagation imaging for small and medium events ($2 \lesssim M \lesssim 5$) is more difficult to realize due to sparse seismic networks, i.e., limited azimuthal coverage, or limited resolution relative to the source dimensions. Some studies for medium sized and small events exist, for example *Boatwright* [2007] or *Kane et al.* [2013]. Older studies usually dealt with rupture properties of single earthquakes [*Li et al.*, 1995; *Jost et al.*, 1998], and only recently larger sets of events were examined for complexities or directivity [*Lengliné and Got*, 2011; *Kane et al.*, 2013; *Calderoni et al.*, 2015; *Ross and Ben-Zion*, 2016; *Abercrombie et al.*, 2017]. Recent studies also analyzed microseismic events [*Dreger et al.*, 2007; *Taira et al.*, 2015; *Folesky et al.*, 2015, 2016] in an effort to connect with the scales from physical rupture modeling in the laboratory and numerical modeling [e.g., *Lapusta et al.*, 2000; *Kaneko and Shearer*, 2014, 2015].
A second interesting issue are the conditions under which a preferred directivity may occur. It is current understanding that rupture initiation, propagation, and termination are complex phenomena which are affected by multiple properties such as the material contrast of the juxtaposed rock types at the two sides of a fault [*Weertman*, 1980; *Ben-Zion*, 2001]. Also, among other aspects, stress state [e.g., *Ampuero and Ben-Zion*, 2008] and perturbations of the stress field, e.g. by pore pressure changes due to fluid injection were proposed to affect rupture directivity [*Shapiro et al.*, 2011; *Folesky et al.*, 2016].
The scope of this study is to contribute to the prevailing debate on what controls the directivity of earthquakes. We investigate rupture directivity of multiple small to medium (M_L 2.6-M_L 5.3) events in the northern Chile subduction zone, which were recorded by the Integrated Plate boundary Observatory Chile. On 2014 April 1 the M_W 8.1 Iquique megathrust earthquake occurred in the southern Peru - northern Chile seismic gap [e.g., *Hayes et al.*, 2014; *Schurr et al.*, 2014]. This event was preceded by a large number of foreshocks and followed by numerous aftershocks, as e.g. the M_W 7.6 aftershock on 2014 April 3, resulting in a high seismicity rate for this region. Multiple large events ($M_L \geq 5$) from this seismic sequence were found to display strong unilateral directivity [*Folesky et al.*, 2018] including the megathrust and its largest foreshock and aftershock [*Schurr et al.*, 2014; *Meng et al.*, 2015; *Folesky et al.*, 2018].
The data set also constitutes a rich basis for the here presented comprehensive study on rupture directivity even for events of significantly smaller magnitude. In this manuscript we describe how we compute waveform similarity based empirical Green's function (EGF) pairs and then reconstruct the source time functions at all recording stations. Further, the amplitudes of these source time functions are analyzed for azimuthal variations corresponding to the directivity effect of unilateral ruptures. The procedure is tested with a synthetic event catalog in order to ensure the robustness of the approach for the given source-receiver geometry in northern Chile. The resulting catalog is finally analyzed for spatio-temporal dependencies of rupture direction and the existence of a preferred rupture directivity.

2 Data: The IPOC Network and Event Catalog

We focus our work on the region of the 2014 M_W 8.1 Iquique event and its foreshock and aftershock series; the spatial extent of the research area ranges from 19.0°S−21.0°S and 69.5°W−71.5°W. We use the seismic CX-net of the Integrated Plate boundary Observatory Chile (*IPOC* [2006], see Figure 1) which covers a large part of the back-azimuth window for events occurring in our research area. 100 Hz, three-component broadband waveform data were accessed via the European Integrated Data Archive web service of GFZ Potsdam

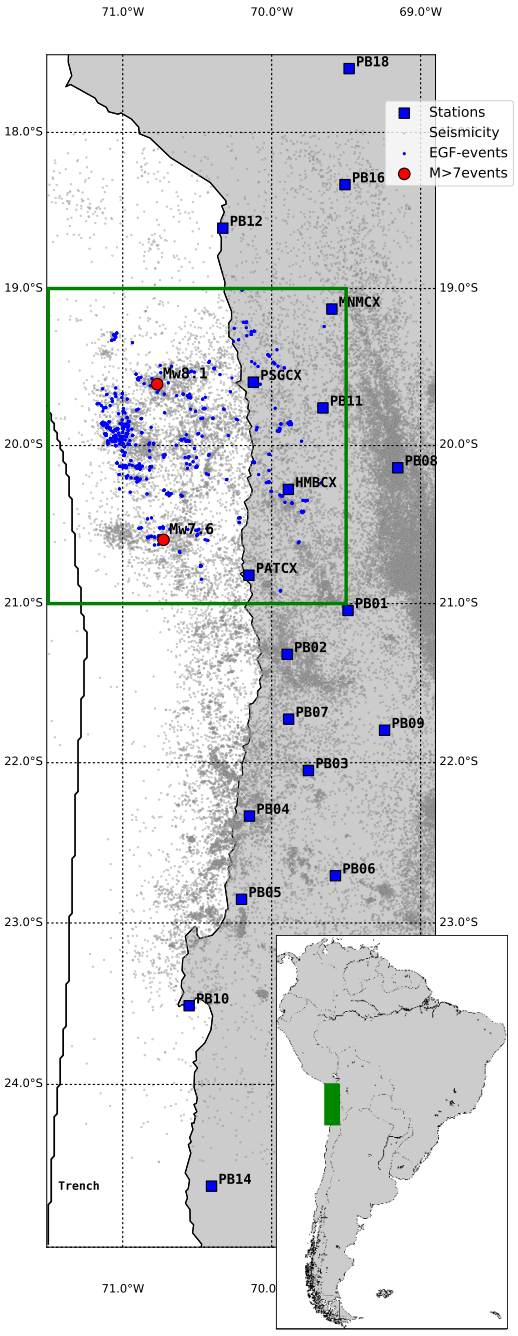

Figure 1. Northern Chile seismicity map view. The locations of IPOC stations are shown by blue squares. Earthquake locations from the event catalog by *Sippl et al.* [2018] are marked with gray dots. The study is limited to the area highlighted by the green square. The 730 EGF-pairs from this study are color-coded in blue. The location of the M_W8.1 Iquique event and its biggest aftershock are highlighted red.

[*Bianchi et al.*, 2015]. For origin times, locations, magnitudes, and take-off angles we use the extensive catalog of *Sippl et al.* [2018] that comprises more than 100.000 events in the northern Chile subduction zone forearc.
To identify suitable candidate earthquake pairs for our EGF analysis, we proceed as follows: We select 9071 events from the catalog, which are located in the target area of this study, and we use the waveforms obtained at the favorably situated station PB11 as templates for a search of similar events in the continuous seismic waveform data recorded between 2008 and 2016. We apply a bandpass filter between $1-4$ Hz and cut a 35 s time window which starts 5 s before the P pick and includes both P and a significant part of the S energy. For each filtered template waveform, we then run a cross correlation detector and identify a suitable EGF-partner for the template event, if the normalized cross correlation coefficient (CC) exceeds a value of $CC \geq 0.90$ and if the amplitude ratio is higher than 10 or lower than 0.1, corresponding to a magnitude difference of $\Delta M = 1$ between the template and detected event. The high cross correlation coefficient calculated for a time window that includes both P and S phases is a strict criterion to ensure that the inter-event distance is very small [e.g., *Menke*, 1999] and that the difference in travel paths is negligible. Application of these criteria results in a total of 730 candidate EGF-pairs, where the larger EGF-partners are within a range of M_L 2.6 to M_L 5.3. In the following we call these events EGF-pair if a main event has one associated EGF-event and EGF-family if there is one main event having more than one EGF-partner.

3 Method and Testing

An empirical Green's function technique based on spectral deconvolution [*Mueller*, 1985; *Li et al.*, 1995] is used to reconstruct the relative source time functions (RSTFs) of each event at all available stations. This is combined with a directivity analysis based on a model of theoretical variations of the RSTF amplitudes as a function of azimuth for an unilateral rupture [*Savage*, 1965]:

$$F = \frac{A}{K} = \frac{v_r}{1 - (v_r/c) \cdot cos(\phi - \phi_0) \cdot sin(\theta - \theta_0)}. \quad (1)$$

Here, F describes the expected amplitude A at a given station, scaled by an unknown constant K. v_r is the rupture velocity and c is the phase velocity, respectively. ϕ is the station azimuth relative to the hypocenter and θ is the ray take-off angle. ϕ_0 is the azimuthal orientation of the rupture direction and θ_0 describes the dip of the rupture plane.
The procedure is performed using three-component 100 Hz displacement waveforms, where only P phases are utilized which are cut out by a fixed 7.5 s time window, starting 1 s before the P pick. A 0.8-20 Hz bandpass filter is applied and the individually reconstructed RSTFs at each component are stacked to obtain an average RSTF for each station. This is repeated station-wise for the entire station network. We fit the amplitude variation model described by equation 1 to the amplitudes obtained from the station-wise reconstructed RSTFs in order to find the rupture direction of the event, that is, we solve for the parameters $\frac{v_r}{c}$ and ϕ_0 (for more details, see *Folesky et al.* [2016]). In the target area the vast majority of events occur at the plate interface [*Sippl et al.*, 2018] exhibiting similar thrust mechanisms [*Cesca et al.*, 2016] with one fault plane oriented in good agreement with the dipping angle of the subducting slab. We therefore fix the dip of the rupture plane to the subduction angle given in the slab 1.0 model [*Hayes et al.*, 2012]. In our case this is implemented by a fixed θ_0, which we use to correct the take-off angles in order to account correctly for the observation point directivity [*Kwiatek and Ben-Zion*, 2016]. This is necessary if stations do not lie on the rupture plane, but are vertically offset affecting the recorded waveforms as a consequence of the 3-D character of the directivity effect. With the fixed dip assumption the number of free parameters in the inversion is reduced to two. For further details and examples on the directivity estimation and the deconvolution approach used see *Folesky et al.* [2016] and sources therein.

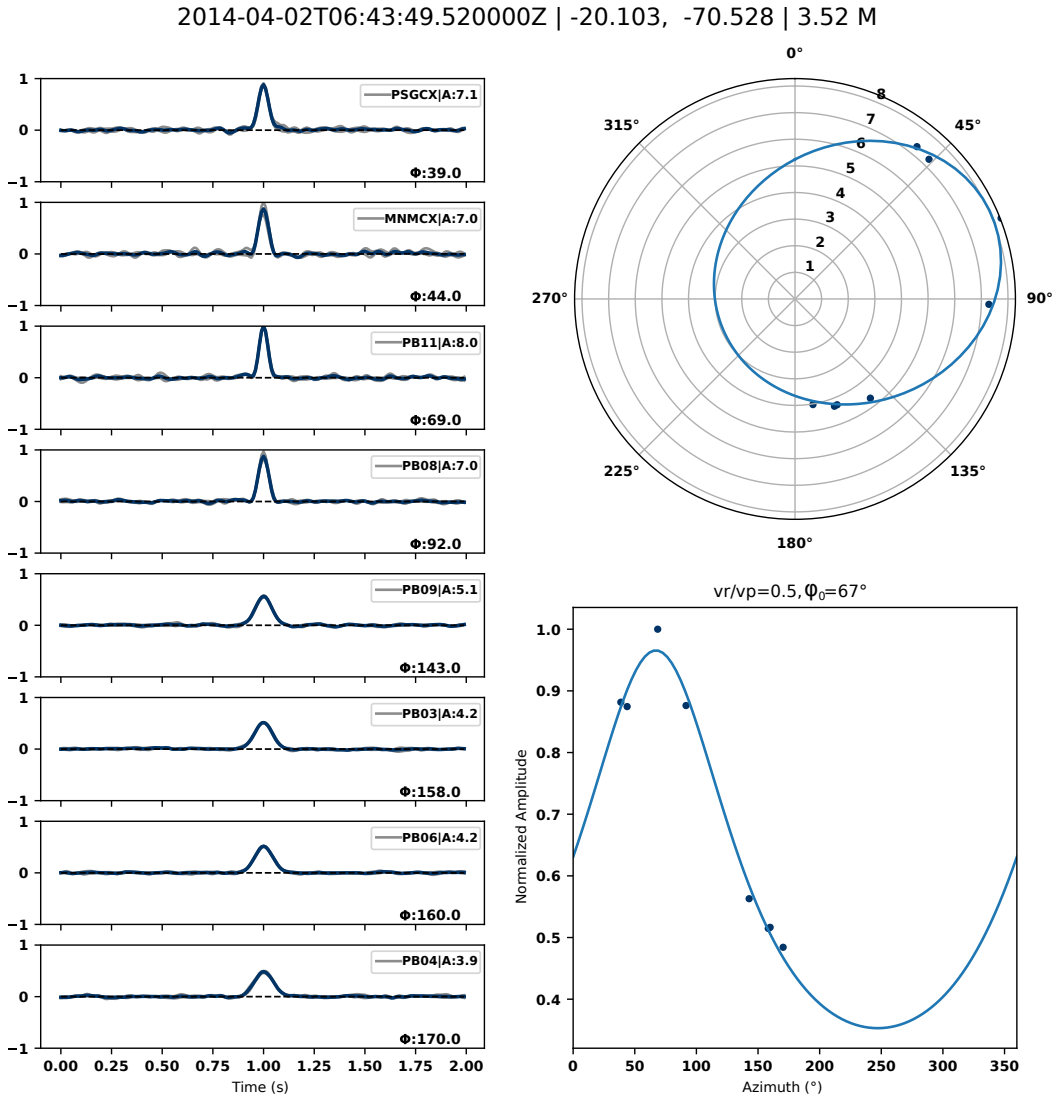

Figure 2. Rupture direction estimation for a synthetic EGF-pair. On the left azimuthally sorted RSTFs are shown, illustrating the step-wise change of amplitude and width of the pulse due to the modeled characteristics of the directivity effect. The legend states amplitude value of the RSTF, station name, and the station back-azimuth ϕ. On the right, the amplitude measurements of the RSTFs are plotted as black dots at the station back-azimuths. The best fitting unilateral rupture model is shown in rose diagram and sinusoidal form as curve in blue. The true rupture properties were $\frac{v_r}{v_p}$=0.5 and ϕ_0=60°N. Estimated values are $\frac{v_r}{v_p}$=0.5 and ϕ_0=67 °N.

The accuracy of the procedure is tested for the given data and the event-station-configuration in northern Chile by creating a synthetic data set. For this, the observed P phases of a randomly selected event out of our EGF-catalog are extracted and then convolved with a scaled Gaussian pulse. The width of the pulse is 0.2 s and the amplitude is set to 10, which corresponds to a magnitude difference of an EGF-pair with ΔM=1. Depending on the event station back-azimuth the pulse amplitude and width are varied as described by the model of *Savage* [1965] for an unilateral propagating rupture. The convolved traces are considered as the waveforms of the main event for the EGF-pair. Then, in a second step, the EGF analysis is performed in order to recompute the initially rupture modeled directions.
Figure 2 exemplarily shows azimuthally sorted source time functions of a simulated EGF-pair. Here, we model a horizontal rupture with an azimuthal direction of 60°N and a rupture velocity of $\frac{v_r}{v_p} = 0.5$. Additional noise was added, such that the seismograms of the smaller event partner have a S/N of 20 dB. We estimate a rupture velocity of $\frac{v_r}{v_p} = 0.5$ and a rupture direction toward 67°N, which is close to the modeled values. We repeat this test multiple times for different rupture directions and noise levels. The analysis shows that the statistical error is independent of the modeled rupture direction and increases with noise level. For events with a S/N of 20 dB for the EGF-event the error is about ±20° and increases to ±40° for a S/N of 10 dB. A detailed description and a summary for the synthetic tests are provided in the supplement.

4 Results

Figure 3 shows the RSTFs and the fit of a M_L3.3 event in the same format as in the previous section. The initial number of 730 suitable pairs is reduced by the data availability, i.e., number of stations, their azimuthal distribution, and the number of picks for each event. We require at least six well reconstructed RSTFs which corresponds to at least six records at six stations including picks. We consider a RSTF at a given station as well reconstructed if it shows a clear pulse-like shape at not less than two of the three components, which have to be of similar shape. Additionally, the stations must cover at least an azimuthal window of 90°. For the event pairs that fulfill these requirements the directivity is estimated and a total number of 293 solutions in agreement with the unilateral rupture model is found. These 293 rupture direction estimates still contain several redundancies, because some EGF-families consist of multiple events which results in multiple counts. In Figure 4 waveforms of such an EGF-family are displayed. For the main event (M_L 3.1) six suitable EGF-events (M_L 1.29-M_L 2.10) were identified. For each pair the directivity analysis was performed separately and the results are consistent. From 293 separately obtained results redundancies occur for 134 EGF-pairs which can be grouped into 48 EGF-families, that is, one main event having two or more EGF-events. Note that we do not find an EGF-family with one event being simultaneously the EGF-partner of a bigger main event and having a smaller EGF-partner itself.

We then use the redundancy of estimated rupture directions within an EGF-family to obtain an error estimate on the computed directions for the real data. Due to variations in magnitude and noise, data availability is slightly different for each EGF-pair within a family and the reconstructed RSTFs may show minor differences. We compute an average rupture direction for each EGF-family. Then, we plot the deviation of each single direction estimate to its corresponding family average. The result is shown in Figure 5. We find that the direction estimates within EGF-families are stable and show an average deviation of 14° while 95% of the computed values are smaller than 35°. We assume that the average error for the non EGF-family events is similar, and we take the value of $\Delta\phi_0$=35° as a conservative estimate of the fixed statistical error for entire data set. The error estimate is further evaluated by a bootstrap test for all events within the EGF-catalog. This test allows to resolve the robustness of the results for each event. The additional figures show directivity errors, the velocity distribution and velocity errors. They can be found in the

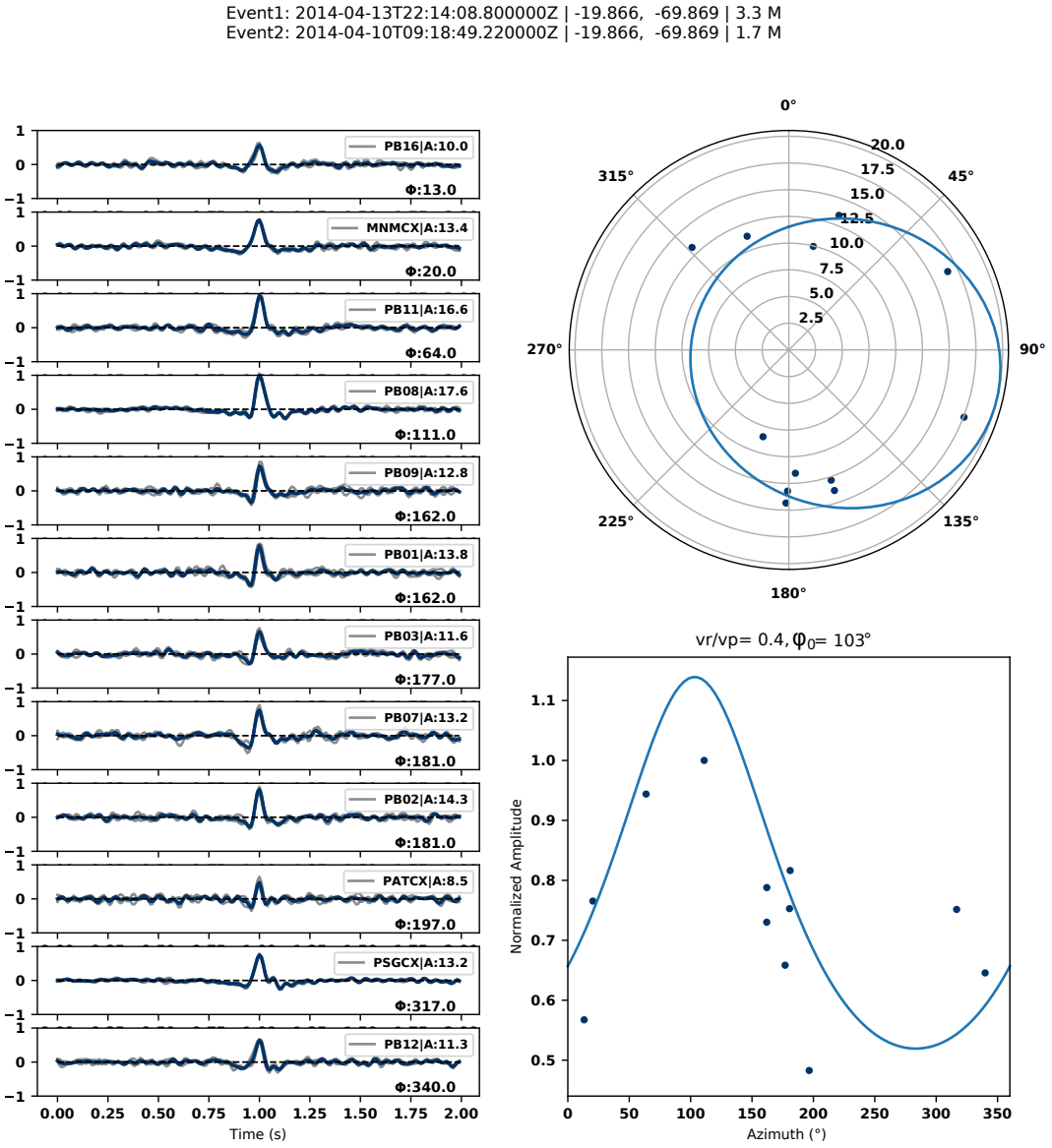

Figure 3. Rupture direction estimate for an EGF-pair consisting of a M_L3.3 and a M_L1.7 event. The RSTFs on the left are sorted for back-azimuth relative to the event location. The varying pulse amplitudes are measured and plotted to the right as black dots. An unilateral rupture model corresponding to equation 1 is fitted to the data, yielding the rupture direction of ϕ_0=103°N and a rupture velocity ratio of $\frac{v_r}{v_p} = 0.4$.

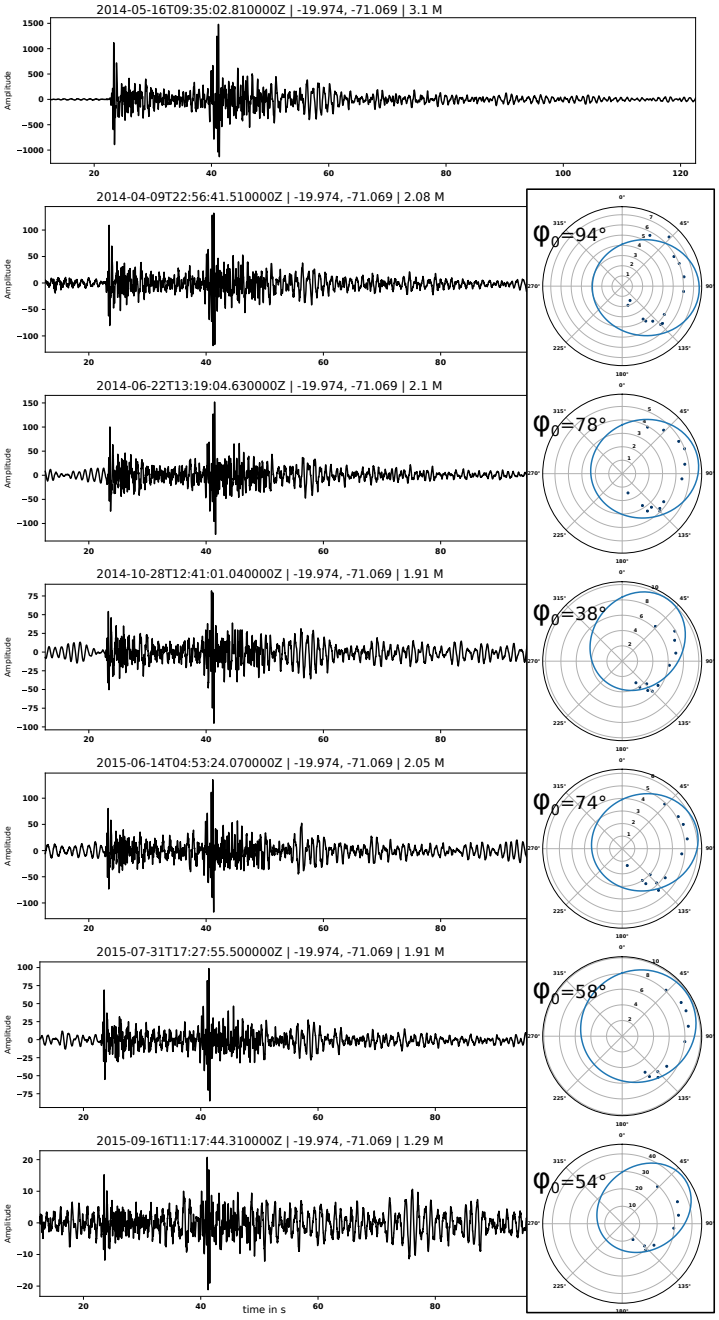

Figure 4. Exemplary EGF-family series. For the main event (M_L 3.1) six EGFs were identified. Displayed are the waveforms obtained at station PB11 for the main event at the top and the EGFs below. The waveforms are sorted by event occurrence date. They show extremely high waveform similarity with the main event. The individually performed rupture directivity results are displayed on the right (cf. Figures 2 & 3). The estimated rupture directions (ϕ_0) are consistent between different EGF-pairs, which is expected, because directivity is a property of the large event partner which is the same for all events. Variations in direction estimates occur mainly due to differing data availability for each event. A statistic on the average deviation of rupture directivity within EGF-families is computed and shown in Figure 5.

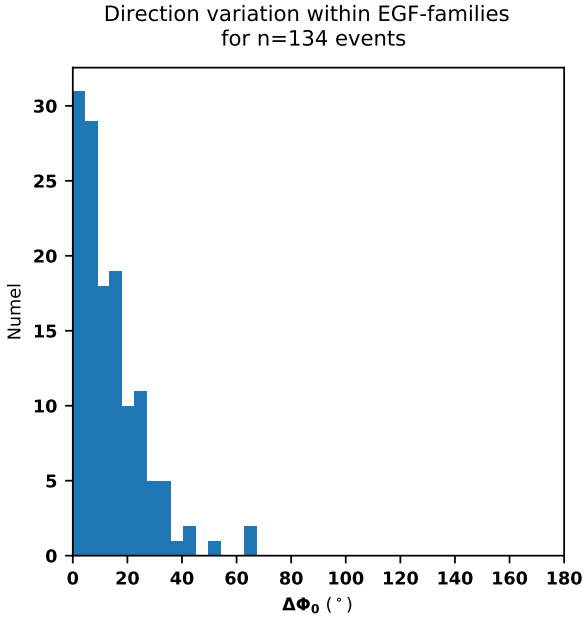

Figure 5. Deviation ($\Delta\phi_0$) between each single EGF-pair rupture direction estimate and its corresponding average EGF-family rupture direction estimate. Low values indicate similar direction estimates within EGF-families. The average deviation is $\Delta\phi_0$=14° while 95% of the computed values are smaller than 35°.

supporting information.

In a next step we remove the redundant direction counts from the overall results. In this way we finally obtain 207 independent rupture estimates which are displayed in Figure 6 in map and side views. The figure illustrates the distribution of rupture directions with a strong preference towards east (directions between 30°N−120°N from north). Although generally all rupture directions are found within the distribution, the dominance of the prevailing direction (∼80°N) is striking.

The majority of events occur at the plate interface. Some events at 71°W seem to be located at greater depth within the oceanic plate. Note, however, that depth resolution specifically for the offshore events is relatively poor [*Sippl et al.*, 2018]. According to their repeating-earthquake like nature (ensured by our waveform similarity-based selection criterion) these event are more likely to have occurred at the plate interface, as the required loading mechanism to produce such events is given there. It is also worth mentioning that we do not find any clear indication of a spatio-temporal dependency within the distribution of rupture directions. The average estimated rupture velocity is $\frac{v_r}{v_p} = 0.49$. For a standard $\frac{v_p}{v_s}$ ratio of 1.73 this translates to an average rupture velocity of about $\frac{v_r}{v_s} \approx 0.85$. Note that the synthetic tests show that the rupture velocity is less reliably recovered than the rupture direction. This is consistent with the observation of *Abercrombie et al.* [2017] who estimate rupture properties in New Zealand. The result of $\frac{v_r}{v_s} \approx 0.85$ is a typical value for rupture velocity.

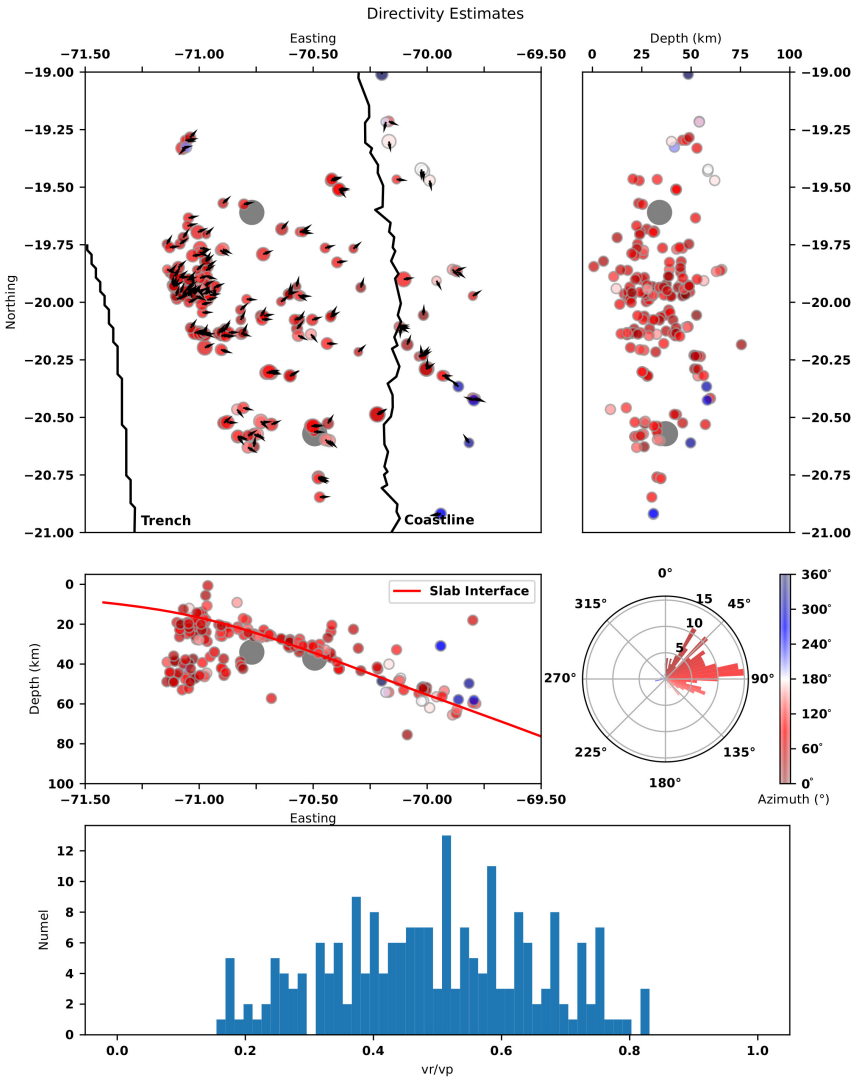

Figure 6. Rupture direction estimates for 207 events from the study area that is highlighted in Figure 1. Top and depth views show the locations of events where we index the rupture direction by a small arrow and a color according to the legend at the bottom right. Reddish colors index eastward directed ruptures, blueish colors show westward directivity. The gray circles are the hypocenters of the mainshock and its largest aftershock, plotted for orientation. The red line is the slab interface after *Hayes et al.* [2012]. The majority of events are oriented eastwards in the direction between 30°N and 120°N. The statistical error for a single direction estimate is $\Delta\phi_0$=35° (see section Results). The bottom panel shows the rupture velocity ratio $\frac{v_r}{v_p}$. The average velocity ratio is $\frac{v_r}{v_p} = 0.49 \pm 0.16$.

5 Discussion

The observation of a dominant rupture direction at a specific site is not a unique phenomenon. For example *Rubin and Gillard* [2000] observed preferred directionality of micro-earthquakes at the central San Andreas fault based on measurements of the P phase pulse width. In contrast, *Harris and Day* [2005] did not find evidence for a preferred rupture direction based on the rupture processes of Parkfield earthquakes which occurred between 1934 to 2004 and had magnitudes of M>4. Their results where, however, based on only relatively few events and their conclusions were subject of an intense debate [*Harris and Day*, 2005; *Ben-Zion*, 2006a,b]. More recent studies like *Lengliné and Got* [2011] found evidence for rupture directivity in repeater sequences, and *Kane et al.* [2013] found preferred oriented directivity for M>3 events at Parkfield, California.

For the San Andreas fault zone, it therefore seems that a preferred direction exists, although not exclusively. To explain the phenomenon of a preferred rupture direction the upper mentioned studies refer to the results of *Weertman* [1980] who found that earthquakes with slip between dissimilar materials produce dynamic changes of normal stress that depend among others on slip direction and material properties of the materials on the two sides of the fault. According to *Weertman* [1980] a dynamic reduction of normal stress occurs if the rupture direction is in concordance with the slip direction of the more compliant solid. This leads to a preferred direction of rupture propagation, called the bimaterial effect. The solutions are valid for sub-Rayleigh rupture velocities and become reversed for super-shear velocities. Also, if slip direction or materials are reversed, a dynamic increase of normal stress on the fault is derived. The nature of ruptures at earthquake faults is of course more complicated than a simple juxtaposition of materials, and the findings of *Weertman* [1980] were further developed by, e.g. *Ben-Zion* [2001]; *Shi and Brune* [2005], and *Ampuero and Ben-Zion* [2008], who studied systematically the asymmetry of macroscopic rupture and crack growth. Using numerical simulations *Ampuero and Ben-Zion* [2008] found that with strong velocity-weakening friction, pulse-like ruptures show macroscopic asymmetry manifested by significantly larger propagation distance in the preferred direction, corresponding to the bimaterial effect. Additionally, *Shi and Brune* [2005] found that the effect does not only occur in strike-slip regimes like the San Andreas fault system but is also observable in thrust regimes. The bimaterial effect has also been observed at other locations, e.g. in southern California [*Ross and Ben-Zion*, 2016] and in Italy [*Calderoni et al.*, 2015].

In case of the northern Chilean subduction zone we find a strong preference of rupture directions towards east, i.e., the great majority of events which we analyzed rupture in the down-dip direction. According to a wide angle seismic study by *Patzwahl et al.* [1999] there exists a velocity contrast at the interface between overlying crust and underlying oceanic plate. Their 2 D cross sections show P wave velocity distributions down to about 40 km depth. At the plate interface the velocity of the underlying plate appears to be about 5-10% smaller than the overlying continental crust. According to the bimaterial effect [*Weertman*, 1980] the preferred rupture direction should consequently be the direction of slip of the more compliant medium, i.e. the down-dip direction.

While this is a plausible explanation of the observed preferred directivity, it cannot explain the remarkable dominance of rupture directions that we found. As described, we expect events on the slab interface to exhibit the statistical preference to rupture downward due to the bimaterial effect, but heterogeneity in structure and stress field should also play an important role [*Ampuero and Ben-Zion*, 2008] and widen the range of estimated direction azimuth values. This is indeed observed for larger events at this site. For example the 2014 8.1 M_W megathrust event and its biggest aftershock (locations in Figure 1) which were located at the plate interface both ruptured to a significant part in the down-dip direction [*Schurr et al.*, 2014; *Meng et al.*, 2015]. In contrast, the great 6.7 M_W foreshock of the main event was situated in the overlying continental crust [*Schurr et al.*, 2014], i.e., it was not affected by the bimaterial effect which was acting at the interface seismicity. According to

Meng et al. [2015] this event ruptured northward showing no indication for a down-dip component. In addition *Folesky et al.* [2018] estimated rupture directivity for 146 $M_L \geq 5$ events in the same research area as this study. They used a P wave polarization based rupture tracking approach and found that generally all rupture directions were present, however, the majority of events ruptured in down-dip direction, and a significant amount of events showed a southward directed rupture component. Generally their resulting distribution of rupture directivity is more heterogeneous than the one of this work. A possible explanation for this effect is the difference in the databases. In contrast to *Folesky et al.* [2018], the here presented results are based on a catalog of smaller sized EGF-pairs. We find many of the features that are reported explicitly for repeating events (c.f. *Nadeau and Johnson* [1998]; *Igarashi et al.* [2003]; *Matsuzawa et al.* [2004]) in our data set as well, as e.g., the very high waveform similarity and thus collocation of the events. Also, we find the great majority of EGF-event locations not within the rupture area of the great M_W 8.1 or M_W 7.6 events, but on the up-dip end of their approximate slip area. We observe long lasting sequences of reoccurring EGFs (what we call EGF-families, compare Figure 4), which can be active over many years as well as clusters of EGF-pairs consisting of only two partners. Following the argumentation of *Igarashi et al.* [2003] repeating earthquakes nucleate in the area surrounding the slip zone of the large earthquakes. In contrast to the main rupture zone this area is only weakly coupled and multiple small asperities are distributed on it, i.e., strongly coupled asperities are contained in an aseismically creeping zone. Depending on the shape of these postulated asperities the rupture area for a given repeater is therefore predefined and may only marginally exceed the size of the asperity.

In a detailed study with highly accurate event locations at a creeping section of the San Andeas fault *Rubin et al.* [1999] show that many repeating events are situated at elongated streaks which only show an extent in slip direction. We observe a similar pattern in many clusters of EGF events and EGF-families in our data set. Therefore it appears reasonable to assume that the asperities have an elongated form in direction of the slip direction. If the strength of the asperity is exceeded, a nucleating rupture would consequently have the choice to either rupture up-dip or down-dip over the area of the asperity, as the asperity is of less spatial extent in the orthogonal directions. According to the bimaterial effect the preferred rupture direction should then be the down-dip direction, which is what we observe for the given data set. The plate convergence direction in our research area is about 76°N [*Angermann et al.*, 1999], which corresponds well to the preferred directivity (∼80°N) found in this study.

Note that we find results for 293 out of 730 suitable event pairs (≈40%). This means that events with unilateral rupture behavior constitute a large part of the total amount of events from the candidate catalog, whereas the remaining events most likely may have different rupture types. Also, the findings are not necessarily representative for non repeating earthquake-like events.

6 Conclusions

We have estimated rupture directivity of local seismic events in northern Chile based on an empirical Green's function approach. The database for the analysis is a catalog of 730 EGF-pairs, that show high waveform similarity, collocation, and a minimum magnitude difference of ΔM=1 for each event pair. We applied an EGF approach to compute relative source time functions for these events and we fitted an unilateral rupture model to the measured amplitudes of these relative source time functions. We found rupture direction estimates for 293 events. By correcting the number of solutions for events with multiple EGF-partners in the catalog, we obtained 207 independent rupture direction estimates. The results show a strong preference (∼80°N) of rupture directivity toward east. This corresponds well to the orientation of the convergence vector between Nazca plate and South-American plate (ϕ=76°N for northern Chile). We propose that the reason for the dominating down-dip rupture direction, sub-parallel to the plate convergence, could be a

lateral limitation of available rupture directions for these events. This would correspond to the concept of repeating earthquakes being confined to an elongated asperity which is situated within an area of aseismic creep. As a result of the bimaterial effect, and based on the material contrast at the plate interface and the slip directions of the plates these laterally confined rupture surfaces should display a preferred down-dip rupture direction for such events. Note that such a sharp peak of orientation may only be found because of the a priori selection criteria of the events. Larger events in the region, which are not classified as or even similar to repeaters, show a less strong pronounced but also clear tendency to rupture in down-dip direction. We do not find evidence for spatio-temporal dependency of the rupture orientation in our results. Also, no notable influence on the rupture directivity by the main event, for example, due to stress perturbation could be found.

Acknowledgments

JF was funded by the German Science foundation, DFG, project number SH 55/15-1. We thank the developers and communities of the utilized open source resources (Python 3.5.1 (python.org), IPython 4.2.0 [*Pérez and Granger*, 2007], NumPy [*Walt et al.*, 2011], Matplotlib [*Hunter*, 2007], and ObsPy [*Beyreuther et al.*, 2010].) and we thank all institutions involved in operating the IPOC network. We thank C.Sippl for preparation and help with the event catalog. We are also grateful to the editor and two anonymous reviewers for their constructive comments on the manuscript. The EGF-pair catalog from this study is available from the supporting information to this article.

References

Abercrombie, R. E., P. Poli, and S. Bannister (2017), Earthquake Directivity, Orientation, and Stress Drop within the Subducting Plate at the Hikurangi Margin, New Zealand, *Journal of Geophysical Research: Solid Earth*, *122*(12).

Ampuero, J.-P., and Y. Ben-Zion (2008), Cracks, pulses and macroscopic asymmetry of dynamic rupture on a bimaterial interface with velocity-weakening friction, *Geophysical Journal International*, *173*(2), 674–692.

Angermann, D., J. Klotz, and C. Reigber (1999), Space-geodetic estimation of the Nazca-South America Euler vector, *Earth and Planetary Science Letters*, *171*(3), 329–334.

Ben-Zion, Y. (2001), Dynamic ruptures in recent models of earthquake faults, *Journal of the Mechanics and Physics of Solids*, *49*(9), 2209–2244.

Ben-Zion, Y. (2006a), Comment on " Material contrast does not predict earthquake rupture propagation direction" by R.A. Harris and S.M. Day, *Geophysical research letters*, *33*(13).

Ben-Zion, Y. (2006b), Comment on "The wrinkle-like slip pulse is not important in earthquake dynamic" by D.J. Andrews and R.A. Harris, *Geophysical Research Letters*, *33*(6).

Beyreuther, M., R. Barsch, L. Krischer, T. Megies, Y. Behr, and J. Wassermann (2010), ObsPy: A Python toolbox for seismology, *Seismological Research Letters*, *81*(3), 530–533.

Bianchi, M., P. L. Evans, A. Heinloo, and J. Quinteros (2015), Webdc3 Web Interface, gFZ Data Services, doi: 10.5880/GFZ.2.4/2016.001.

Boatwright, J. (2007), The persistence of directivity in small earthquakes, *Bulletin of the Seismological Society of America*, *97*(6), 1850–1861.

Calderoni, G., A. Rovelli, Y. Ben-Zion, and R. Di Giovambattista (2015), Along-strike rupture directivity of earthquakes of the 2009 L'Aquila, central Italy, seismic sequence, *Geophysical Journal International*, *203*(1), 399–415.

Cesca, S., F. Grigoli, S. Heimann, T. Dahm, M. Kriegerowski, M. Sobiesiak, C. Tassara, and M. Olcay (2016), The Mw 8.1 2014 Iquique, Chile, seismic sequence: a tale of foreshocks and aftershocks, *Geophysical Journal International*, *204*(3), 1766–1780.

Dreger, D., R. M. Nadeau, and A. Chung (2007), Repeating earthquake finite source models: Strong asperities revealed on the San Andreas Fault, *Geophysical Research Letters*, *34*(23).

Folesky, J., J. Kummerow, and S. A. Shapiro (2015), Microseismic rupture propagation imaging, *Geophysics*, *80*(6), WC107–WC115.

Folesky, J., J. Kummerow, S. A. Shapiro, M. Häring, and H. Asanuma (2016), Rupture directivity of fluid-induced microseismic events: Observations from an enhanced geothermal system, *Journal of Geophysical Research: Solid Earth*, *121*(11), 8034–8047.

Folesky, J., J. Kummerow, G. Asch, B. Schurr, C. Sippl, F. Tilmann, and S. A. Shapiro (2018), Estimating Rupture Directions from Local Earthquake Data Using the IPOC Observatory in Northern Chile, *Seismological Research Letters*, doi:10.1785/0220170202.

Harris, R. A., and S. M. Day (2005), Material contrast does not predict earthquake rupture propagation direction, *Geophysical research letters*, *32*(23).

Hayes, G. P., D. J. Wald, and R. L. Johnson (2012), Slab1. 0: A three-dimensional model of global subduction zone geometries, *Journal of Geophysical Research: Solid Earth*, *117*(B1).

Hayes, G. P., M. W. Herman, W. D. Barnhart, K. P. Furlong, S. Riquelme, H. M. Benz, E. Bergman, S. Barrientos, P. S. Earle, and S. Samsonov (2014), Continuing megathrust earthquake potential in Chile after the 2014 Iquique earthquake, *Nature*, *512*(7514), 295.

Hunter, J. D. (2007), Matplotlib: A 2D graphics environment, *Computing In Science & Engineering*, *9*(3), 90–95.

Igarashi, T., T. Matsuzawa, and A. Hasegawa (2003), Repeating earthquakes and interplate aseismic slip in the northeastern Japan subduction zone, *Journal of Geophysical Research: Solid Earth*, *108*(B5).

IPOC (2006), IPOC Seismic Network. Integrated Plate boundary Observatory Chile - IPOC, GFZ German Research Centre for Geosciences; Institut des Sciences de lUnivers-Centre National de la Recherche CNRS-INSU, Seismic Network, doi: 10.14470/PK615318.

Jost, M. L., T. Büßelberg, O. Jost, and H.-P. Harjes (1998), Source parameters of injection-induced microearthquakes at 9 km depth at the KTB Deep Drilling site, Germany, *Bulletin of the Seismological Society of America*, *88*(3), 815–832.

Kane, D. L., P. M. Shearer, B. P. Goertz-Allmann, and F. L. Vernon (2013), Rupture directivity of small earthquakes at Parkfield, *Journal of Geophysical Research: Solid Earth*, *118*(1), 212–221.

Kaneko, Y., and P. M. Shearer (2014), Seismic source spectra and estimated stress drop derived from cohesive-zone models of circular subshear rupture, *Geophysical Journal International*, *197*(2), 1002–1015, doi:10.1093/gji/ggu030.

Kaneko, Y., and P. M. Shearer (2015), Variability of seismic source spectra, estimated stress drop, and radiated energy, derived from cohesive-zone models of symmetrical and asymmetrical circular and elliptical ruptures, *Journal of Geophysical Research B: Solid Earth*, *120*(2), 1053–1079, doi:10.1002/2014JB011642.

Kwiatek, G., and Y. Ben-Zion (2016), Theoretical limits on detection and analysis of small earthquakes, *Journal of Geophysical Research: Solid Earth*, *121*(8), 5898–5916.

Lapusta, N., J. R. Rice, Y. Ben-Zion, and G. Zheng (2000), Elastodynamic analysis for slow tectonic loading with spontaneous rupture episodes on faults with rate-and state-dependent friction, *Journal of Geophysical Research: Solid Earth*, *105*(B10), 23,765–23,789.

Lengliné, O., and J.-L. Got (2011), Rupture directivity of microearthquake sequences near Parkfield, California, *Geophysical Research Letters*, *38*(8).

Li, Y., C. Doll, and M. N. Toksöz (1995), Source characterization and fault plane determination for MbLg = 1.2 to 4.4 earthquakes in the Charlevoix Seismic Zone, Quebec, Canada, *Bulletin of the Seismological Society of America*, *85*(6), 1604–1621.

Lomax, Anthony and Virieux, Jean and Volant, Philippe and Berge-Thierry, Catherine (2000), Probabilistic earthquake location in 3D and layered models, *Advances in seismic event location, Springer*, 101–134.

Matsuzawa, T., N. Uchida, T. Igarashi, T. Okada, and A. Hasegawa (2004), Repeating earthquakes and quasi-static slip on the plate boundary east off northern Honshu, Japan, *Earth, planets and space*, *56*(8), 803–811.

McGuire, J. J., L. Zhao, and T. H. Jordan (2002), Predominance of unilateral rupture for a global catalog of large earthquakes, *Bulletin of the Seismological Society of America*, *92*(8), 3309–3317.

Meng, L., H. Huang, R. Bürgmann, J. P. Ampuero, and A. Strader (2015), Dual megathrust slip behaviors of the 2014 Iquique earthquake sequence, *Earth and Planetary Science Letters*, *411*, 177–187.

Menke, W. (1999), Using waveform similarity to constrain earthquake locations, *Bulletin of the Seismological Society of America*, *89*(4), 1143–1146.

Mueller, C. S. (1985), Source pulse enhancementt by deconvolution of an empirical Green's function, *Geophys. Res. Lett.*, *12*, 33–36.

Nadeau, R. M., and L. R. Johnson (1998), Seismological studies at Parkfield VI: Moment release rates and estimates of source parameters for small repeating earthquakes, *Bulletin of the Seismological Society of America*, *88*(3), 790–814.

Patzwahl, R., J. Mechie, A. Schulze, and P. Giese (1999), Two-dimensional velocity models of the nazca plate subduction zone between 19.5 s and 25 s from wide-angle seismic measurements during the cinca95 project, *Journal of Geophysical Research: Solid Earth*, *104*(B4), 7293–7317.

Pérez, F., and B. E. Granger (2007), Ipython: a system for interactive scientific computing, *Computing in Science & Engineering*, *9*(3).

Ross, Z. E., and Y. Ben-Zion (2016), Toward reliable automated estimates of earthquake source properties from body wave spectra, *Journal of Geophysical Research: Solid Earth*, *121*(6), 4390–4407.

Rubin, A. M., and D. Gillard (2000), Aftershock asymmetry/rupture directivity among central San Andreas fault microearthquakes, *Journal of Geophysical Research: Solid Earth*, *105*(B8), 19,095–19,109.

Rubin, A. M., D. Gillard, and J.-L. Got (1999), Streaks of microearthquakes along creeping faults, *Nature*, *400*(6745), 635.

Savage, J. C. (1965), The effect of rupture velocity upon seismic first motions, *Bull. Seism. Soc. Am.*, *55*, 263–275.

Schurr, B., G. Asch, S. Hainzl, J. Bedford, A. Hoechner, M. Palo, R. Wang, M. Moreno, M. Bartsch, Y. Zhang, et al. (2014), Gradual unlocking of plate boundary controlled initiation of the 2014 Iquique earthquake, *Nature*, *512*(7514), 299.

Shapiro, S. A., O. S. Krüger, C. Dinske, and C. Langenbruch (2011), Magnitudes of induced earthquakes and geometric scales of fluid-stimulated rock volumes, *Geophysics*, *76*(6), WC55–WC63.

Shi, B., and J. N. Brune (2005), Characteristics of near-fault ground motions by dynamic thrust faulting: two-dimensional lattice particle approaches, *Bulletin of the Seismological Society of America*, *95*(6), 2525–2533.

Sippl, C., B. Schurr, G. Asch, and J. Kummerow (2018), Seismicity structure of the Northern Chile forearc from >100,000 double-difference relocated hypocenters, *Journal of Geophysical Research: Solid Earth*, *123*, doi:doi:10.1002/2017JB015384.

Taira, T., D. S. Dreger, and R. M. Nadeau (2015), Rupture process for micro-earthquakes inferred from borehole seismic recordings, *International Journal of Earth Sciences*, *104*(6), 1499–1510, doi:10.1007/s00531-015-1217-8.

Walt, S. v. d., S. C. Colbert, and G. Varoquaux (2011), The NumPy array: a structure for efficient numerical computation, *Computing in Science & Engineering*, *13*(2), 22–30.

Weertman, J. (1980), Unstable slippage across a fault that separates elastic media of different elastic constants, *Journal of Geophysical Research: Solid Earth*, *85*(B3), 1455–1461.

Supporting Information for "Patterns of Rupture Directivity of Subduction Zone Earthquakes in Northern Chile"

Jonas Folesky,[1]Jörn Kummerow,[1]Serge A. Shapiro,[1]

[1]Freie Universität Berlin, Department of Geophysics, Berlin, Germany

We test the robustness of our fitting routine by simulating different ensembles of events of different rupture direction. We randomly draw 126 events from our target event catalog. Each event is treated as follows. The originally observed P phases obtained at each station are extracted and they are convolved with a scaled Gaussian pulse. The width of the pulse is 0.2 s and the amplitude is set to 10, which corresponds to a magnitude difference of an EGF-pair of ΔM=1. Depending on the event station back-azimuth the pulse amplitude and width is varied as described by the model of Savage (BSSA, 1965) for an unilateral horizontal propagating rupture. The convolved traces are considered as the waveforms of the main event for the EGF-pair. Then, in a second step, the EGF analysis is performed in order to recompute the rupture directions that where initially modeled.
To obtain a representative estimate of the properties of the resulting direction distribution we use the original stations, event location, and the real data availability (i.e., for events with seismograms obtained at 8 stations we simulated EGF-records for exactly those 8 stations as shown in Figure 2 main manuscript). The test is performed repeatedly for different amounts of white noise, that were added to the seismograms of both the smaller and the larger event. The noise level is chosen such, that for the smaller event a signal-to-noise ratio (S/N) of 10 dB, 20 dB, 40 dB, and infinity (no added noise) is achieved after adding the noise. Here S/N is computed as the ratio of the peak amplitude of the signal to the standard deviation of the added noise in dB. In addition to the variation of noise we compute four different sets of modeled rupture directions for each noise level. The results are displayed in the Figures S 1 - 4. For all event sets very reasonable rupture direction estimates are found and also the $\frac{v_r}{v_p}$ ratios are recovered well. Because the errors are comparable for all four directions for a given noise level, there seems to be no network geometry-based bias. Also, low station numbers are in principle not critical if a reasonable large azimuthal window is covered by the active stations. We therefore define a minimum azimuth coverage of 90° as an additional quality criterion. The average $\frac{v_r}{v_p}$ ratio is biased weakly in direction of smaller values than originally modeled, for the directions 60° and 90° this is more significant than for -60° and 180°. Due to the relatively large uncertainty a significant amount of events shows a rupture velocity $\frac{v_r}{v_p} \geq 0.6$ which would (most likely) erroneously indicate super-shear rupture velocities. Hence, especially the $\frac{v_r}{v_p}$ ratio should be interpreted as a property of the ensemble, rather than for single events. The overall results are summarized in supplementary Table 1. Generally, we find that rupture orientation is stable and accuracy decreases primarily with increasing noise level. Directions are more reliably recovered than rupture velocity, which is consistent with EGF-based directivity estimates from New Zealand by Abercrombie et al.(JGR,2017).

In a separate file we supply the catalog of EGF-pairs (730) which were selected as described in the data section of the main article. We provide hypocenter, magnitude and take-off angles for each event. In the catalog the larger partner is always followed by its corresponding EGF-event. The list contains the utilized take-off angles, which are listed after the respective station codes. They were obtained from the authors of Sippl et al. 2018 via personal communication. The take-off angles are approximate values because they are taken from an intermediate step of the localization procedure. Sippl et al. 2018 used a

Corresponding author: Jonas Folesky, jonas.folesky@geopyhsik.fu-berlin.de

direction	10 dB	20 dB	40 dB	inf
60°	50° ±45°	61° ±19°	59° ±8°	59° ±4°
90°	90° ±35°	91° ±26°	90° ±5°	89° ±12°
180°	174° ±32°	175° ±19°	178° ±5°	179° ±7°
-60°	-60° ±48°	-62° ±19°	-61° ±10°	-60° ±7°

$\frac{v_r}{v_p}$	10 dB	20 dB	40 dB	inf
60°	0.31 ±0.16	0.39 ±0.07	0.47 ±0.04	0.49±0.03
90°	0.30 ±0.11	0.36 ±0.11	0.47 ±0.03	0.48±0.06
180°	0.41 ±0.12	0.44 ±0.06	0.49 ±0.01	0.50±0.03
-60°	0.46 ±0.23	0.49 ±0.14	0.53 ±0.11	0.54±0.10

Table S 1. Overview of the rupture directions (ϕ_0) and velocities ($\frac{v_r}{v_p}$) and the corresponding standard deviations for the four ensembles of modeled EGF-pairs. We modeled four rupture directions with a rupture velocity of $\frac{v_r}{v_p}$=0.5, and for each direction four varying noise levels. For each combination we display the resulting mean and use the standard deviation of the ensemble as error. Details are shown in the supplement Figures S 1 - 4. For S/N=40 dB and S/N=inf the results are very good, and isolated error values greater than 5° are produced by outliers. For realistic noise levels (S/N 20 dB and 40 dB) the error is tolerable. Even for relatively strong noise (S/N 10 dB) the modeled rupture directions are recovered. Not that even if noise levels are high, the difference between true and estimated rupture direction remains small in all cases. Compared to the initially modeled rupture velocity of $\frac{v_r}{v_p}$=0.5 almost all estimates tend to be underestimated, demonstrating that velocity is less well constrained than direction.

multi-step localization procedure whose last step is the double-difference localization (see reference therein), which produced the event locations that they published in the cited catalog, but no take-off angles. The prior step is a NonLinLoc (Lomax et al., (ASEL,2000)) localization which outputs ray take-off angles. For our analysis it was necessary to work with more stations than we had picks provided by Sippl et al. 2018. For those stations, where no picks were provided we therefore added additional manual picks and computed the corresponding take-off angles. For this we approximated the take-off angles by interpolation of the catalog based take-off angles for a given event. Where this was not possible we used full catalog based averaged take-off angles which were computed for depth bins over the entire catalog, i.e., we averaged all takeoff-angles for all events of a given depth and specific event-station distance. The interpolation of those averaged values produced a lookup curve which provided an average take-off angle for every possible event-station distance.

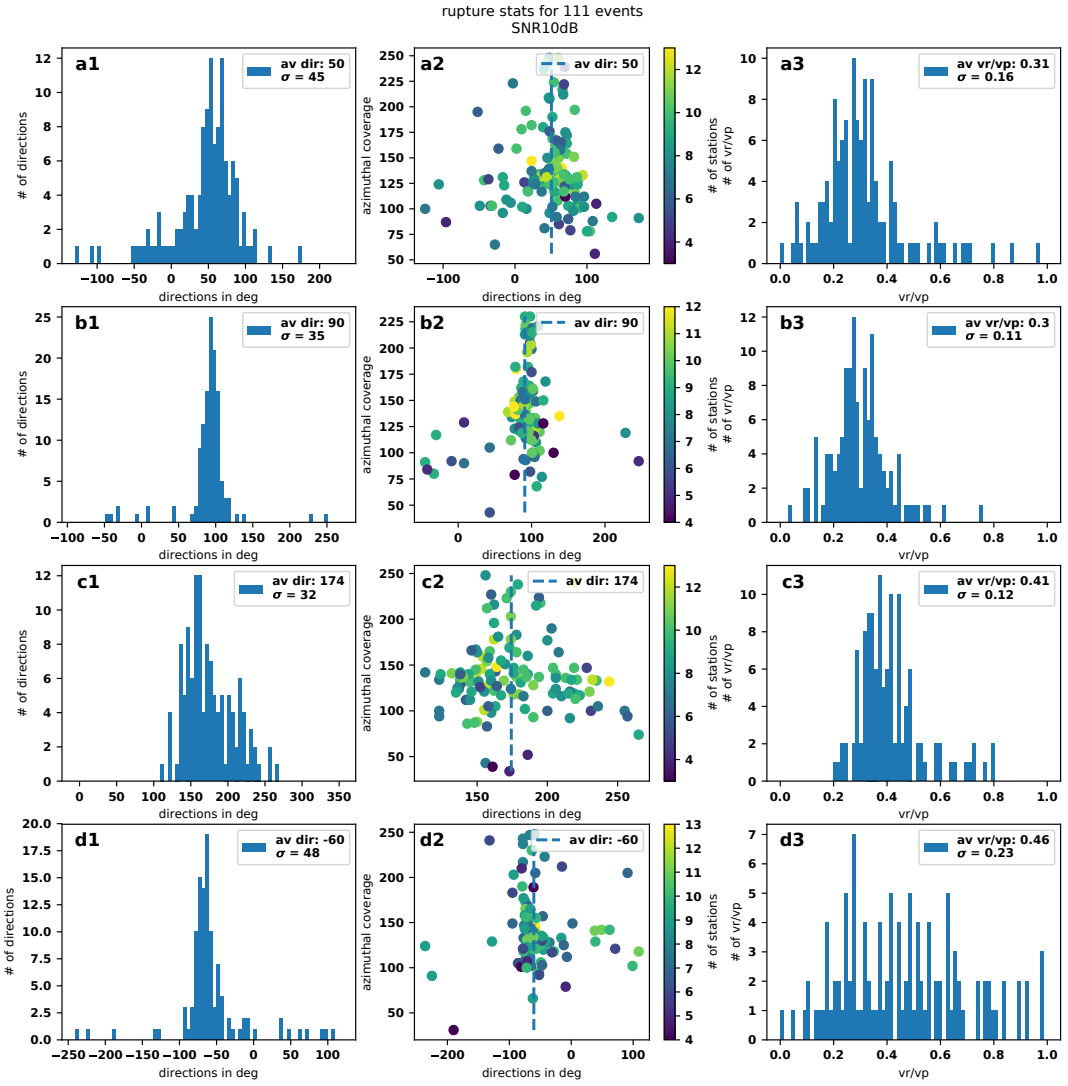

Figure S 1. Statistical rupture properties for four ensembles (a-d) of 111 events with four different rupture directions (60°,90°,180°,-60°), respectively. All ensembles consist of modeled EGF-pairs with synthetic noise resulting in a S/N of 10 dB and rupture velocity of $\frac{v_r}{v_p}$=0.5. Displayed are the results of the fitting procedure for each ensemble: the average direction (row 1), the average direction against azimuthal coverage and station number (row 2), and the average estimated $\frac{v_r}{v_p}$ rupture velocity (row 3). Despite the high noise level the average estimated rupture direction deviates from the initially modeled value by maximal 10° (a1), however standard deviation is high. This is also true for the rupture velocity ratios.

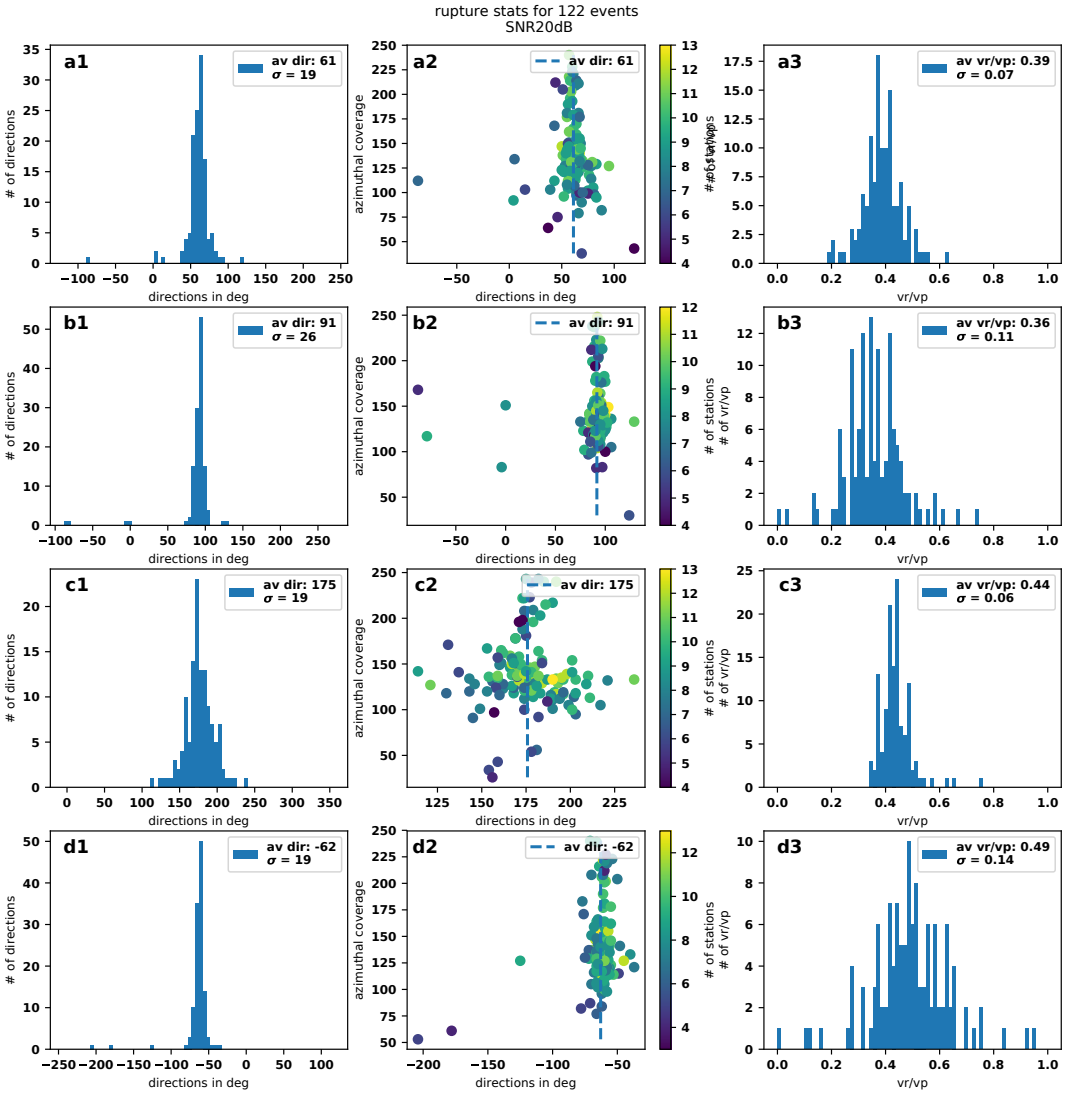

Figure S 2. Rupture properties for four ensembles (a-d) of 122 events with different modeled rupture directions 60°,90°,180°,-60°, respectively. All ensembles share the same rupture velocity of $\frac{v_r}{v_p}$=0.5 and consist of modeled EGF-pairs with synthetic noise resulting in a S/N of 20 dB. The Figure is structured similar to Figure S 1. Note that although the initially modeled values are recovered well in average , the uncertainty especially for the $\frac{v_r}{v_p}$ ratio is high.

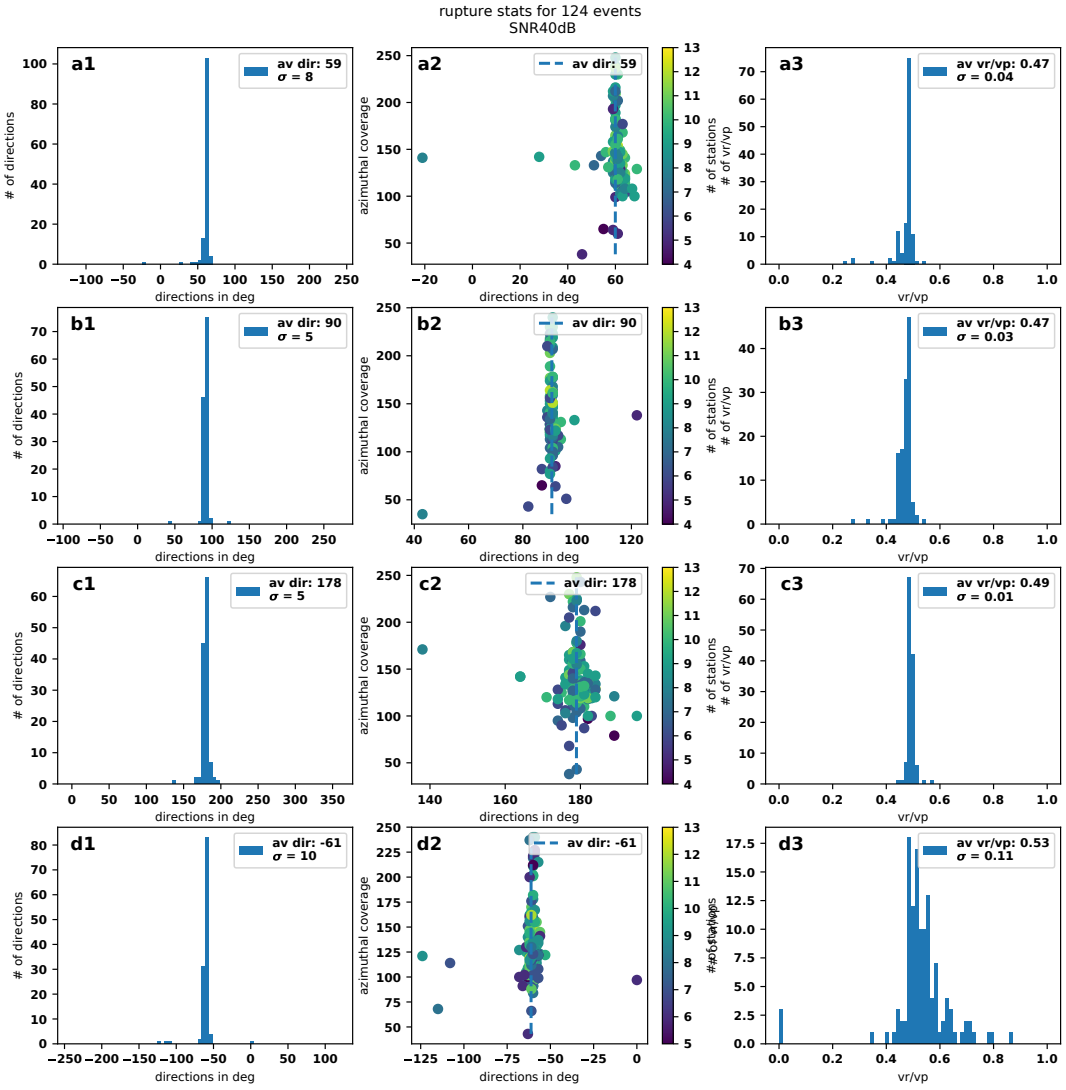

Figure S 3. Statistical rupture properties for four ensembles (a-d) of 124 events with four different rupture directions (60°,90°,180°,-60°), respectively. All ensembles consist of modeled EGF-pairs with synthetic noise resulting in a S/N of 40 dB and rupture velocity of $\frac{v_r}{v_p}$=0.5. The Figure is structured similar to Figure S 1. Note that the initially modeled results are recovered almost precisely, with very few exceptions.

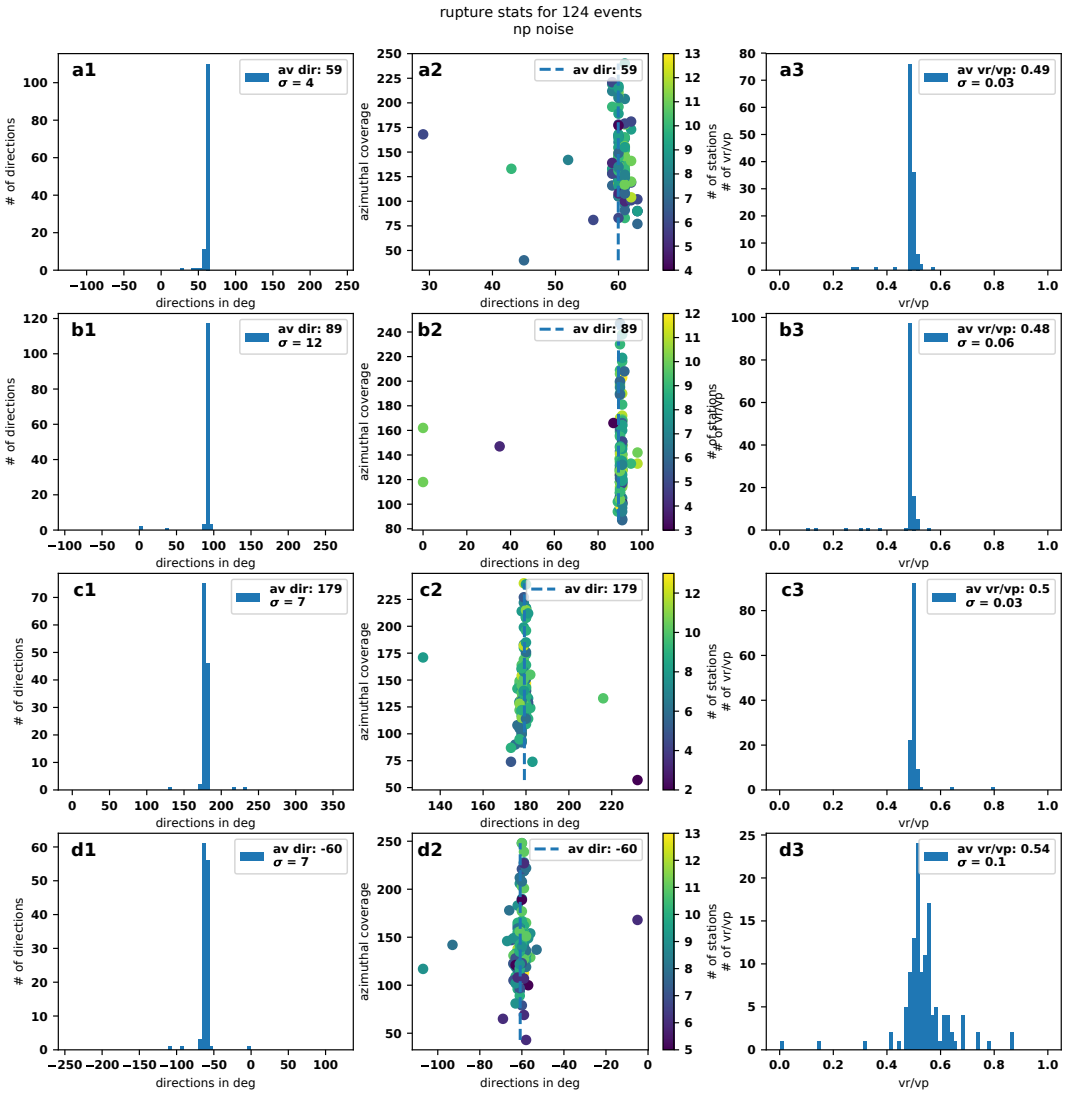

Figure S 4. Statistical rupture properties for four ensembles (a-d) of 124 events with four different rupture directions (60°,90°,180°,-60°), respectively. All ensembles consist of modeled EGF-pairs with no synthetic noise added and rupture velocity of $\frac{v_r}{v_p}$=0.5. The Figure is structured similar to Figure S 1. Note that the initially modeled results are recovered almost precisely.

We further evaluate the individual errors for each event using a bootstrap approach. This means for each event, we recompute the EGF's, the directivity and rupture velocities for 1000 realizations. In each realization, we discard two randomly selected stations, except for the few events where only six stations are available. In this case we discard only one station. Average directions and velocities are computed for each of the 293 events for which we find solutions (in the main manuscript). Due to the reduced data availability they slightly differ from the directions and velocity ratios obtained using all available data. In addition we can then computed the standard deviations of both quantities. The results are shown in the Figures S 5–S 8. The errors of both quantities show no pronounced spatial correlation which means that no apparent influence of location or network geometry on the results is visible. While the rupture directivity shows a pronounced peak towards the east (down-dip) the velocity ratio is distributed around a mean value of $\frac{v_r}{v_p}$=0.5 and its spatial distribution shows no significant trend. The error distribution of both quantities are similar. A correlation of both errors for single events is apparent, i.e. a small error in direction goes along with a small error in velocity. Overall the analysis shows that the direction and velocity ratio estimates from this study are stable without significant influence of event location or station availability or geometry.

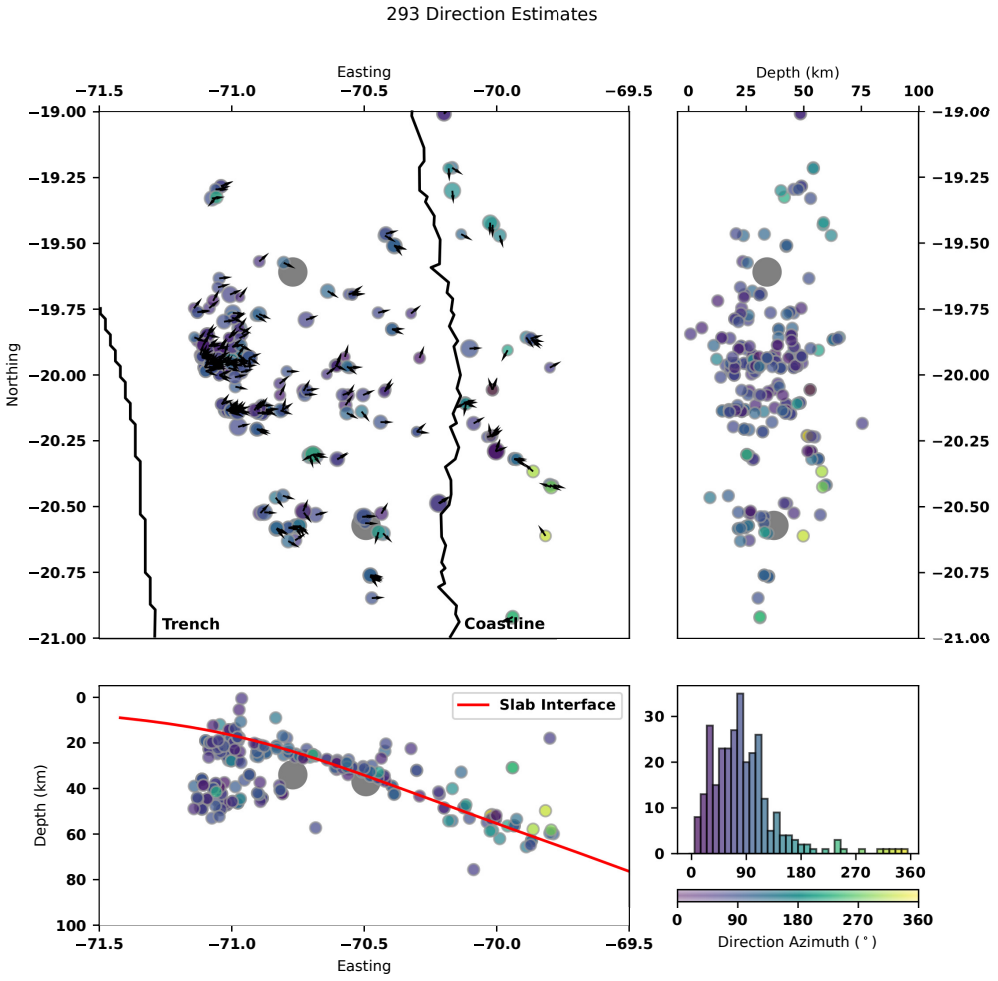

Figure S 5. Average rupture directions obtained from a bootstrap test with 1000 runs for each individual event. Note that we show results for all 293 direction estimates in contrast to Figure 6 of the main article, where redundant solutions are removed. The average directions from the bootstrap tests only differ very slightly from the original results where all amplitudes are used for the direction estimate, i.e. the bootstrap test shows the robustness of our method for the data set.

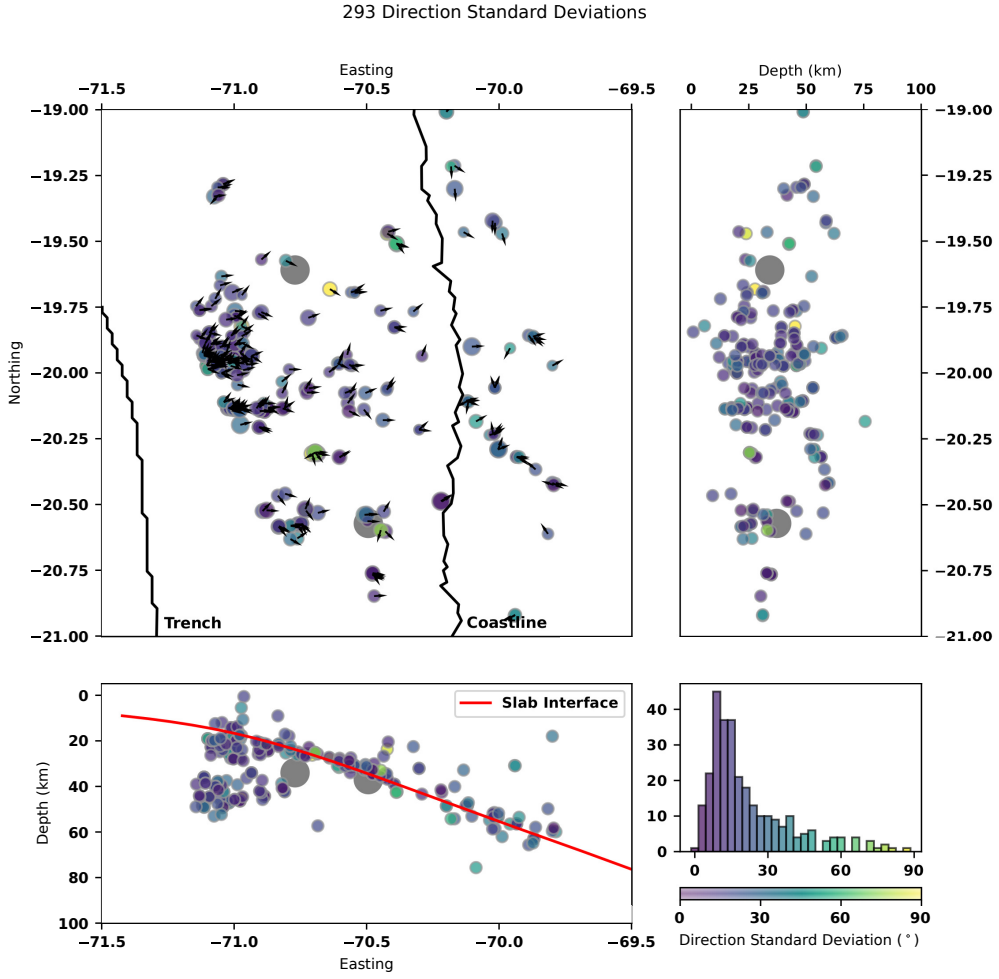

Figure S 6. Standard deviation of rupture directions in Figure S 5. No spatial trend is found and for most events the errors are smaller than the fixed error obtained in the main manuscript (35°). Note especially that directivity estimates which deviate from the preferred average trend (east) from Figure S 5 do not exhibit with high standard deviations.

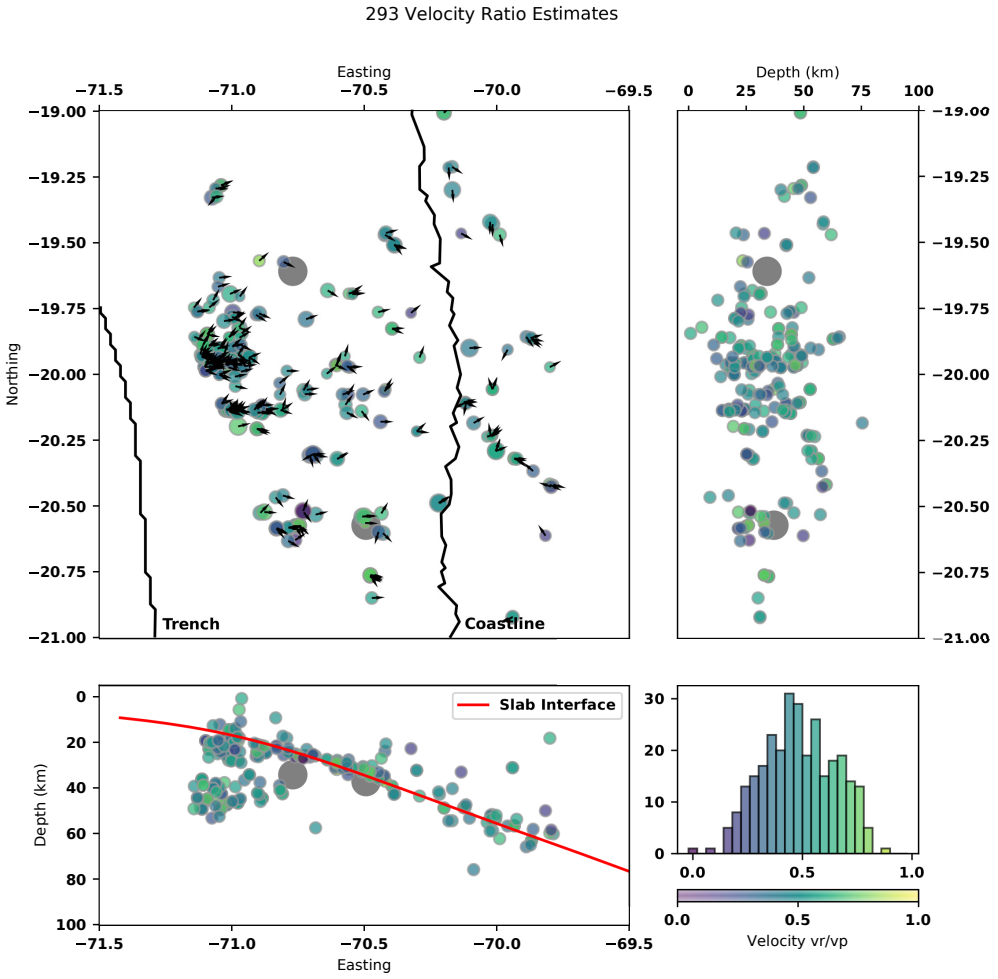

Figure S 7. Rupture velocity ratio obtained from a bootstrap test with 1000 runs for each individual event. The obtained distribution of average velocity ratios is highly similar to the distribution of velocity ratios obtained with the full available data (Figure 6 main article). The mean of the averaged velocity ratio distribution is 0.5 which translates into a rupture speed of $v_r = 0.8v_s$. No direct correlation of rupture velocity ratios and rupture directions (Figure S 5) is apparent.

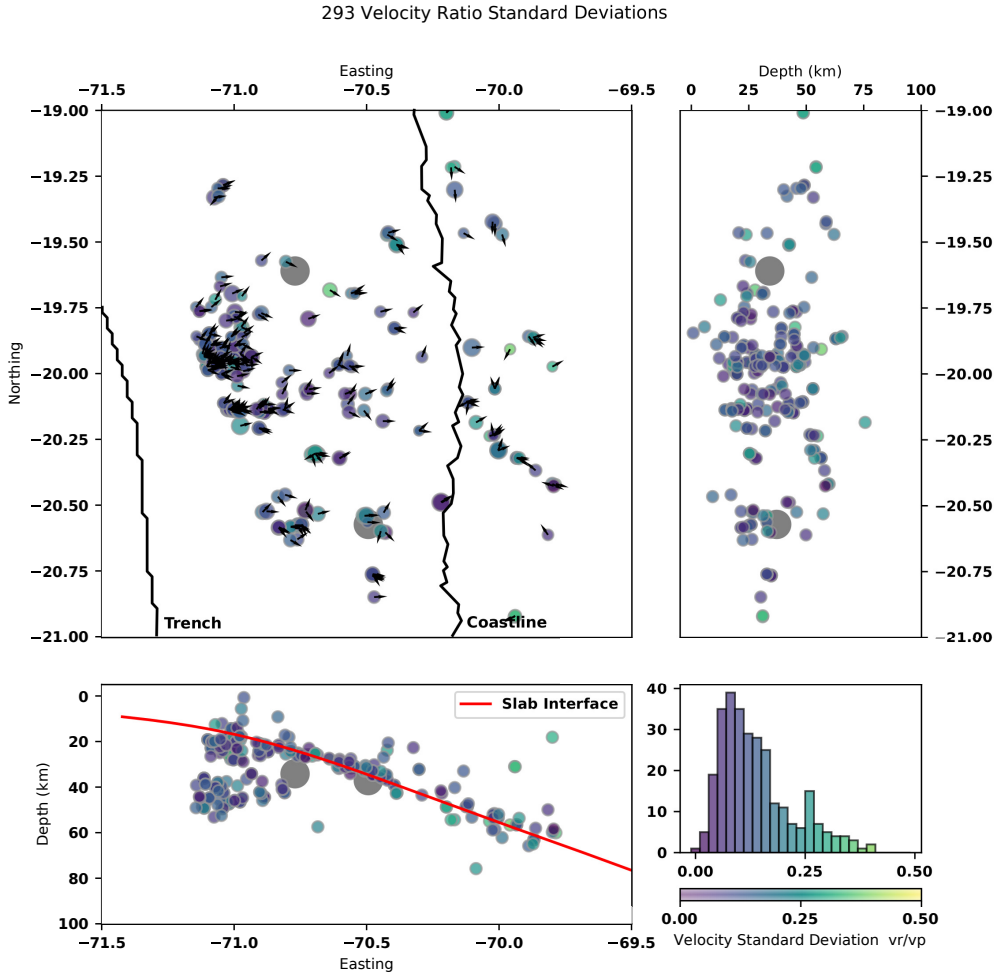

Figure S 8. Standard deviations for rupture velocity ratios from bootstrap test. No spatial dependency is visible within the spatial distribution of errors. However, errors correlate with errors for the direction estimates in Figure S 6. Also, the overall shapes of the error distributions for velocity ratios and direction estimates is similar.

EGF table

In this file we supply the catalog of 730 EGF-pairs which the basis of the analysis in this article. We provide hypocenter, magnitude and take-off angles for each event. In the event list the larger partner is always followed by its corresponding EGF-event. The list contains the utilized take-off angles, which are listed after the respective station codes. Here, $90 \geq \theta > 0$ is vertical up, $\theta = 0$ is horizontal, $0 > \theta \geq -90$ is vertical down.

Chapter 7

Conclusions and Outlook

In the presented thesis, I analyzed rupture directivity of seismicity at two very different locations: a geothermal reservoir and a subduction zone. With explicit examples, I showed that, from tiny events with M≈1 to huge megathrust earthquakes with M≈8, seismic sources may show strong directivity and rupture complexities. I also demonstrated that the rupture processes can be visualized, using a combination of different rupture propagation imaging approaches. For this, the three analysis techniques back projection imaging, empirical Green's function analysis, and P wave polarization stacking were outlined, refined, and applied. In both data sets, I used a combination of techniques to extract rupture properties and find substantiated properties of the ensemble of event ruptures, which was important for further interpretation. Today, there still exists a limited amount of studies which deal with the estimation of in situ rupture parameters and their spatio-temporal distribution at georeservoirs, as it is done here.

In the case study at the Basel-1 EGS, it was possible to image the largest events, using the back projection technique. Although the technique usually takes advantage of waveform coherency at a distant array, I demonstrated that for an azimuthally well-distributed station network imaging is also possible if the radiated seismic energy and the rupture extent in relation to event receiver distance are sufficiently large. This is the case for the four largest events at that site. For smaller magnitude events, the empirical Green's function approach produced clear results for many events down to a minimum magnitude of M≈1. The two studies utilized two independent imaging approaches and produced complementary results, providing a clear observation of a magnitude-dependent rupture directivity for the Basel-1 EGS. Due to the small number of M>3 events at the Basel-1 EGS, the application of the two complementary techniques was an important step to increase the evaluable magnitude range. Thereby the number of analyzable events was increased and the results of both studies were mutually substantiated.

The same is true for the analysis of seismicity in the region of the 2014 M_W8.1 Iquique

in northern Chile. Here, the P wave polarization stacking was applicable for M≥5 events because only these events possibly had sufficiently large enough rupture areas to be trackable at the given site. The observed distribution of rupture directivity shows a preference of the direction of rupture toward east, which is the down-dip directions along the subducting plate. Additionally, by using the empirical Green's function technique at the same data set, I was able to analyze events of smaller magnitudes. Similar to the findings from the previous Basel studies, I found that the results for both studies were complementary. For the EGF-deduced rupture directions, the distribution is much sharper, but the preferred direction is again the down-dip direction, albeit it is oriented slightly different toward east-northeast. One explanation for this observation is a bimaterial effect acting at the plate interface that produces a preferred rupture direction.

The four studies from Chapter 3–6 clearly indicate that the process of the earthquake rupture may be complex for a large range of event sizes. Hence, source parameter studies should consider the influence of rupture directivity if the respective accuracy is intended. Simultaneously, with the appropriate technique and carefully adjusted imaging parameters, rupture features can be imaged at various magnitude scales if the conditions allow for the necessary resolution. This not only provides the tools to possibly enhance the quality of estimated source parameters such as corner frequency and stress-drop but also provides a basis for a more profound analysis of the cause or the absence of a preferred rupture orientation.

For a thorough interpretation of the physical parameters, which may determine rupture behavior, it will be necessary to analyze more high-quality data sets in similar and also in substantially different environments in order to build a better data base. In combination with results from numerical studies and analog modeling studies at laboratory scale the picture will become increasingly clearer. One can hypothesize that if a better understanding of the origin of a certain rupture behavior is achieved, it could eventually become possible to derive in situ properties at the event source such as material velocity contrast or stress state directly or indirectly from the rupture properties. However, this is still a long way ahead, since the direct link between the behavior of a given rupture and the in situ stress and material properties is an ongoing research area with many unknowns.

One way to advance into this direction and contribute to this subject is to further enhance the imaging techniques. Especially the P wave polarization stacking, as it was used in this thesis, would benefit from a more explicitly incorporated correction for the directivity effect, which could be used as a refinement parameter for an iterative imaging approach. The technique suffers from the fact that stations in rupture direction observe a diminished rupture length while for stations in opposite direction, the duration of rupture appears enhanced. When the time sample wise stacking is performed, these variations may lead to increasingly inaccurate stacks based on the sample mismatch.

This could be accounted for by an iterative imaging approach where a first estimate of rupture direction and speed could be used to resample the records for each station to obtain a new sample base which then could be used in a second imaging step to increase coherency.

An additional issue is the incorporation of the 3-D character of the directivity effect in reservoirs where the depth of the event is comparable with the event station distance. In contrast to teleseismic imaging approaches where the imaging problems are treatable effectively as 2-D scenarios, the decreased distance of observer stations brings formerly negligible effects into play. In this work, this is only partly considered when using the empirical Green's function based directivity analysis where I considered the observation point directivity. Hence, it still needs further elaboration to be incorporated into all three rupture imaging approaches in future works.

Bibliography

Abercrombie, R. E. (2015). Investigating uncertainties in empirical Green's function analysis of earthquake source parameters. *Journal of Geophysical Research: Solid Earth*, 120(6):4263–4277. 2015JB011984.

Aki, K. and Richards, P. G. (2002). *Quantitative seismology*. University Science Books, 2nd edition. 37–59.

Allmann, B. P. and Shearer, P. M. (2007). A High-Frequency Secondary Event During the 2004 Parkfield Earthquake. *Science*, 318(5854):1279–1283.

Ampuero, J.-P. and Ben-Zion, Y. (2008). Cracks, pulses and macroscopic asymmetry of dynamic rupture on a bimaterial interface with velocity-weakening friction. *Geophysical Journal International*, 173(2):674–692.

Angermann, D., Klotz, J., and Reigber, C. (1999). Space-geodetic estimation of the Nazca-South America Euler vector. *Earth and Planetary Science Letters*, 171(3):329–334.

Asanuma, H., Nozaki, H., Niitsuma, H., and Wyborn, D. (2005). Interpretation of microseismic events with larger magnitude collected at Cooper Basin, Australia. *Geothermal Resources Council Transactions*, 29:87–91.

Bayer, B., Kind, R., Hoffmann, M., Yuan, X., and Meier, T. (2012). Tracking unilateral earthquake rupture by P-wave polarization analysis. *Geophysical Journal International*, 188(3):1141–1153.

Ben-Menahem, A. (1961). Radiation of seismic surface-waves from finite moving sources. *Bulletin of the Seismological Society of America*, 51(3):401–435.

Ben-Menahem, A. (1962). Radiation of seismic body waves from a finite moving source in the earth. *Journal of Geophysical Research*, 67(1):345–350.

Ben-Zion, Y. (2001). Dynamic ruptures in recent models of earthquake faults. *Journal of the Mechanics and Physics of Solids*, 49(9):2209–2244.

Ben-Zion, Y. (2006a). Comment on " Material contrast does not predict earthquake rupture propagation direction" by R.A. Harris and S.M. Day. *Geophysical research letters*, 33(13).

Ben-Zion, Y. (2006b). Comment on "The wrinkle-like slip pulse is not important in earthquake dynamic" by D.J. Andrews and R.A. Harris. *Geophysical Research Letters*, 33(6).

Beyreuther, M., Barsch, R., Krischer, L., Megies, T., Behr, Y., and Wassermann, J. (2010). ObsPy: A Python toolbox for seismology. *Seismological Research Letters*, 81(3):530–533.

Bianchi, M., Evans, P. L., Heinloo, A., and Quinteros, J. (2015). Webdc3 Web Interface. GFZ Data Services, doi: 10.5880/GFZ.2.4/2016.001.

Bilek, S., Lay, T., and Ruff, L. (2004). Radiated seismic energy and earthquake source duration variations from teleseismic source time functions for shallow subduction zone thrust earthquakes. *Journal of Geophysical Research: Solid Earth*, 109(B9).

Boatwright, J. (1980). A spectral theory for circular seismic sources; Simple estimates of source dimension, dynamic stress drop, and radiated seismic energy. *Bulletin of the Seismological Society of America*, 70(1):1–27.

Boatwright, J. (2007). The persistence of directivity in small earthquakes. *Bulletin of the Seismological Society of America*, 97(6):1850–1861.

Boatwright, J. and Boore, D. M. (1982). Analysis of the ground accelerations radiated by the 1980 Livermore Valley earthquakes for directivity and dynamic source characteristics. *Bulletin of the Seismological Society of America*, 72(6A):1843–1865.

Brune, J. N. (1970). Tectonic stress and the spectra of seismic shear waves from earthquakes. *Journal of Geophysical Research*, 75(26):4997.

Bürgmann, R. (2014). Warning signs of the Iquique earthquake. *Nature*, 512(7514):258.

Burridge, R. and Knopoff, L. (1964). Body force equivalents for seismic dislocations. *Bulletin of the Seismological Society of America*, 54(6A):1875–1888.

Calderoni, G., Rovelli, A., Ben-Zion, Y., and Di Giovambattista, R. (2015). Along-strike rupture directivity of earthquakes of the 2009 L'Aquila, central Italy, seismic sequence. *Geophysical Journal International*, 203(1):399–415.

Calderoni, G., Rovelli, A., and Di Giovambattista, R. (2017). Rupture directivity of the strongest 2016–2017 central italy earthquakes. *Journal of Geophysical Research: Solid Earth*, 122(11):9118–9131.

Catalli, F., Meier, M., and Wiemer, S. (2013). The role of Coulomb stress changes for injection-induced seismicity: The Basel enhanced geothermal system. *Geophysical Research Letters*, 40(72-77):doi: 10.1029/2012GL054147.

Cesca, S., Grigoli, F., Heimann, S., Dahm, T., Kriegerowski, M., Sobiesiak, M., Tassara, C., and Olcay, M. (2016). The Mw 8.1 2014 Iquique, Chile, seismic sequence: a tale of foreshocks and aftershocks. *Geophysical Journal International*, 204(3):1766–1780.

Comte, D. and Pardo, M. (1991). Reappraisal of great historical earthquakes in the northern Chile and southern Peru seismic gaps. *Natural Hazards*, 4(1):23–44.

Deichmann, N. and Giardini, D. (2009). Earthquakes induced by the stimulation of an enhanced geothermal system below Basel (Switzerland). *Seismological Research Letters*, 80(5):784–798.

Dinske, C. and Shapiro, S. (2010). Interpretation of microseismicity induced by timpe-dependent injection pressure. *SEG Expanded Abstracts*, 29:2125–2129, doi:10.1190/1.3513264.

Dreger, D., Nadeau, R. M., and Chung, A. (2007). Repeating earthquake finite source models: Strong asperities revealed on the San Andreas Fault. *Geophysical Research Letters*, 34(23).

Dyer, B., Schanz, U., Spillmann, T., Ladner, F., and Häring, M. (2010). Application of microseismic multiplet analysis to the Basel geothermal reservoir stimulation events. *Geophysical Prospecting*, 58(5):791–807.

Ellsworth, W. (1992). Imaging fault rupture without inversion. *Seismological Research Letters*, 63:73.

Elst, N. J. and Shaw, B. E. (2015). Larger aftershocks happen farther away: Nonseparability of magnitude and spatial distributions of aftershocks. *Geophysical Research Letters*, 42(14):5771–5778.

Eshelby, J. D. (1957). The Determination of the Elastic Field of an Ellipsoidal Inclusion, and Related Problems. In *Proceedings of the Royal Society of London A: Mathematical, Physical and Engineering Sciences*, volume 241, pages 376–396. The Royal Society.

Folesky, J., Kummerow, J., Asch, G., Schurr, B., Sippl, C., Tilmann, F., and Shapiro, S. A. (2018a). Estimating Rupture Directions from Local Earthquake Data Using the IPOC Observatory in Northern Chile. *Seismological Research Letters*.

Folesky, J., Kummerow, J., and Shapiro, S. (2013). Rupture Propagation Imaging at Microseismic Scale. In *75th EAGE Conference & Exhibition incorporating SPE EUROPEC 2013*.

Folesky, J., Kummerow, J., and Shapiro, S. (2018b). Estimating rupture directivity of local earthquake data in central Italy using P-wave polarity stacking. In *EGU General Assembly Conference Abstracts*, volume 20, page 8747.

Folesky, J., Kummerow, J., and Shapiro, S. A. (2015). Microseismic rupture propagation imaging. *Geophysics*, 80(6):WC107–WC115.

Folesky, J., Kummerow, J., Shapiro, S. A., Häring, M., and Asanuma, H. (2016). Rupture directivity of fluid-induced microseismic events: Observations from an enhanced geothermal system. *Journal of Geophysical Research: Solid Earth*, 121(11):8034–8047.

Frankel, A., Fletcher, J., Vernon, F., Haar, L., Berger, J., Hanks, T., and Brune, J. (1986). Rupture characteristics and tomographic source imaging of ML 3 earthquakes near Anza, southern California. *Journal of Geophysical Research: Solid Earth (1978–2012)*, 91(B12):12633–12650.

Frankel, A. and Kanamori, H. (1983). Determination of rupture duration and stress drop for earthquakes in Southern California. *Bulletin of the Seismological Society of America*, 73(6A):1527–1551.

Goertz-Allmann, B. P., Edwards, B., Bethmann, F., Deichmann, N., Clinton, J., Fäh, D., and Giardini, D. (2011a). A new empirical magnitude scaling relation for Switzerland. *Bulletin of the Seismological Society of America*, 101(6):3088–3095.

Goertz-Allmann, B. P., Goertz, A., and Wiemer, S. (2011b). Stress drop variations of induced earthquakes at the Basel geothermal site. *Geophysical Research Letters*, 38(9).

Goertz-Allmann, B. P. and Wiemer, S. (2012). Geomechanical modeling of induced seismicity source parameters and implications for seismic hazard assessment. *Geophysics*, 78(1):KS25–KS39.

Häring, M. O., Schanz, U., Ladner, F., and Dyer, B. C. (2008). Characterisation of the Basel 1 enhanced geothermal system. *Geothermics*, 37(5):469–495.

Harrington, R. M. and Brodsky, E. E. (2009). Source duration scales with magnitude differently for earthquakes on the San Andreas Fault and on secondary faults in Parkfield, California. *Bulletin of the Seismological Society of America*, 99(4):2323–2334.

Harris, R. A. and Day, S. M. (2005). Material contrast does not predict earthquake rupture propagation direction. *Geophysical research letters*, 32(23).

Haskell, N. (1964). Total energy and energy spectral density of elastic wave radiation from propagating faults. *Bulletin of the Seismological Society of America*, 54(6A):1811–1841.

Haskell, N. (1966). Total energy and energy spectral density of elastic wave radiation from propagating faults. Part ii. a statistical source model. *Bulletin of the Seismological Society of America*, 56(1):125–140.

Hayes, G. P., Herman, M. W., Barnhart, W. D., Furlong, K. P., Riquelme, S., Benz, H. M., Bergman, E., Barrientos, S., Earle, P. S., and Samsonov, S. (2014). Continuing megathrust earthquake potential in Chile after the 2014 Iquique earthquake. *Nature*, 512(7514):295.

Hayes, G. P., Wald, D. J., and Johnson, R. L. (2012). Slab1. 0: A three-dimensional model of global subduction zone geometries. *Journal of Geophysical Research: Solid Earth*, 117(B1).

Hunter, J. D. (2007). Matplotlib: A 2D graphics environment. *Computing In Science & Engineering*, 9(3):90–95.

Hutchings, L. and Viegas, G. (2012). Application of empirical green's functions in earthquake source, wave propagation and strong ground motion studies. In *Earthquake Research and Analysis-New Frontiers in Seismology*. InTech.

Igarashi, T., Matsuzawa, T., and Hasegawa, A. (2003). Repeating earthquakes and interplate aseismic slip in the northeastern Japan subduction zone. *Journal of Geophysical Research: Solid Earth*, 108(B5).

IPOC (2006). IPOC Seismic Network. Integrated Plate boundary Observatory Chile - IPOC, GFZ German Research Centre for Geosciences; Institut des Sciences de l'Univers-Centre National de la Recherche CNRS-INSU, Seismic Network. doi: 10.14470/PK615318.

Ishii, M., Shearer, P. M., Houston, H., and Vidale, J. E. (2005). Extent, duration and speed of the 2004 Sumatra-Andaman earthquake imaged by the Hi-Net array. *Nature*, 435(7044):933.

Ishii, M., Shearer, P. M., Houston, H., and Vidale, J. E. (2007). Telseseismic P wave imaging of the 26 December 2004 Sumatra-Andaman and 28 March 2005 Sumatra earthquake ruptures using the Hi-net array. *Journal of Geophysical Research: Solid Earth*, 112(B11).

Jost, M. L., Büßelberg, T., Jost, O., and Harjes, H.-P. (1998). Source parameters of injection-induced microearthquakes at 9 km depth at the KTB Deep Drilling site, Germany. *Bulletin of the Seismological Society of America*, 88(3):815–832.

Jurkevics, A. (1988). Polarization analysis of three-component array data. *Bulletin of the Seismological Society of America*, 78(5):1725–1743.

Kanamori, H. and Anderson, D. L. (1975). Theoretical basis of some empirical relations in seismology. *Bulletin of the Seismological Society of America*, 65:1073–1095.

Kane, D. L., Shearer, P. M., Goertz-Allmann, B. P., and Vernon, F. L. (2013). Rupture directivity of small earthquakes at Parkfield. *Journal of Geophysical Research: Solid Earth*, 118(1):212–221.

Kaneko, Y. and Shearer, P. M. (2014). Seismic source spectra and estimated stress drop derived from cohesive-zone models of circular subshear rupture. *Geophysical Journal International*, 197(2):1002–1015.

Kaneko, Y. and Shearer, P. M. (2015). Variability of seismic source spectra, estimated stress drop, and radiated energy, derived from cohesive-zone models of symmetrical and asymmetrical circular and elliptical ruptures. *Journal of Geophysical Research B: Solid Earth*, 120(2):1053–1079.

Kao, H. and Shan, S.-J. (2007). Rapid identification of earthquake rupture plane using Source-Scanning Algorithm. *Geophysical Journal International*, 168:1011–1020.

Kato, A. and Nakagawa, S. (2014). Multiple slow-slip events during a foreshock sequence of the 2014 Iquique, Chile Mw 8.1 earthquake. *Geophysical Research Letters*, 41(15):5420–5427.

Kiser, E. and Ishii, M. (2011). The 2010 Mw 8.8 Chile earthquake: Triggering on multiple segments and frequency-dependent rupture behavior. *Geophysical Research Letters*, 38(7).

Kiser, E. and Ishii, M. (2012). The March 11, 2011 Tohoku-oki earthquake and cascading failure of the plate interface. *Geophysical Research Letters*, 39(7).

Kiser, E., Ishii, M., Langmuir, C., Shearer, P., and Hirose, H. (2011). Insights into the mechanism of intermediate-depth earthquakes from source properties as imaged by back projection of multiple seismic phases. *Journal of Geophysical Research: Solid Earth*, 116(B6).

Knopoff, L. (1958). Energy release in earthquakes. *Geophysical Journal International*, 1(1):44–52.

Kraft, T. and Deichmann, N. (2014). High-precision relocation and focal mechanism of the injection-induced seismicity at the Basel EGS. *Geothermics*, 52:59–73.

Krüger, F. and Ohrnberger, M. (2005). Spatio-temporal source characteristics of the 26 December 2004 Sumatra earthquake as imaged by teleseismic broadband arrays. *Geophysical research letters*, 32(24).

Kummerow, J., Dinske, C., Asanuma, H., and Häring, M. (2014). Observation and Signatures of Injection-Induced Repeating Earthquake Sequences. Expanded Abstracts, EAGE 76th annual meeting and technical exhibition.

Kummerow, J., Shapiro, S., Asanuma, H., and Häring, M. (2011). Application of an Arrival Time and Cross Correlation Value-Based Location Algorithm to the Basel 1 Microseismic Data. Expanded Abstracts, EAGE 73nd annual meeting and technical exhibition, Vienna.

Kwiatek, G. and Ben-Zion, Y. (2016). Theoretical limits on detection and analysis of small earthquakes. *Journal of Geophysical Research: Solid Earth*, 121(8):5898–5916.

Kwiatek, G., Plenkers, K., Dresen, G., Group, J. R., et al. (2011). Source parameters of picoseismicity recorded at Mponeng deep gold mine, South Africa: implications for scaling relations. *Bulletin of the Seismological Society of America*, 101(6):2592–2608.

Lapusta, N., Rice, J. R., Ben-Zion, Y., and Zheng, G. (2000). Elastodynamic analysis for slow tectonic loading with spontaneous rupture episodes on faults with rate-and state-dependent friction. *Journal of Geophysical Research: Solid Earth*, 105(B10):23765–23789.

Lengliné, O. and Got, J.-L. (2011). Rupture directivity of microearthquake sequences near Parkfield, California. *Geophysical Research Letters*, 38(8).

Li, Y., Doll, C., and Toksöz, M. N. (1995). Source characterization and fault plane determination for MbLg = 1.2 to 4.4 earthquakes in the Charlevoix Seismic Zone, Quebec, Canada. *Bulletin of the Seismological Society of America*, 85(6):1604–1621.

Lomax, A., Virieux, J., Volant, P., and Berge-Thierry, C. (2000). Probabilistic earthquake location in 3D and layered models. In *Advances in seismic event location*, pages 101–134. Springer.

Madariaga, R. (1976). Dynamics of an expanding circular fault. *Bulletin of the Seismological Society of America*, 66(3):639–666.

Madariaga, R. (2007). 4.02 - Seismic Source Theory. In Schubert, G., editor, *Treatise on Geophysics*, pages 59 – 82. Elsevier, Amsterdam.

Majer, E. L., Baria, R., Stark, M., Oates, S., Bommer, J., Smith, B., and Asanuma, H. (2007). Induced seismicity associated with enhanced geothermal systems. *Geothermics*, 36(3):185–222.

Maruyama, T. (1963). On the Force Equivalent of Dynamic Elastic Elastic Dislocation with Reference to the Earthquake Mechanism. *Bull. Earthq. Res. Inst.*, 41:467–488.

Matsuzawa, T., Uchida, N., Igarashi, T., Okada, T., and Hasegawa, A. (2004). Repeating earthquakes and quasi-static slip on the plate boundary east off northern Honshu, Japan. *Earth, planets and space*, 56(8):803–811.

McGuire, J. J., Zhao, L., and Jordan, T. H. (2002). Predominance of unilateral rupture for a global catalog of large earthquakes. *Bulletin of the Seismological Society of America*, 92(8):3309–3317.

Meng, L., Ampuero, J.-P., Sladen, A., and Rendon, H. (2012). High-resolution backprojection at regional distance: Application to the Haiti M7.0 earthquake and comparisons with finite source studies. *Journal of Geophysical Research: Solid Earth*, 117(B4).

Meng, L., Huang, H., Bürgmann, R., Ampuero, J. P., and Strader, A. (2015). Dual megathrust slip behaviors of the 2014 Iquique earthquake sequence. *Earth and Planetary Science Letters*, 411:177–187.

Mori, J. (1993). Fault plane determinations for three small earthquakes along the San Jacinto fault, California: Search for cross faults. *Journal of Geophysical Research: Solid Earth (1978–2012)*, 98(B10):17711–17722.

Mueller, C. S. (1985). Source pulse enhancementt by deconvolution of an empirical Green's function. *Geophys. Res. Lett.*, 12:33–36.

Mukuhira, Y., Asanuma, H., Niitsuma, H., and Häring, M. O. (2013). Characteristics of large-magnitude microseismic events recorded during and after stimulation of a geothermal reservoir at Basel, Switzerland. *Geothermics*, 45:1–17.

Nadeau, R. M. and Johnson, L. R. (1998). Seismological studies at Parkfield VI: Moment release rates and estimates of source parameters for small repeating earthquakes. *Bulletin of the Seismological Society of America*, 88(3):790–814.

Park, S. and Ishii, M. (2015). Inversion for rupture properties based upon 3-D directivity effect and application to deep earthquakes in the Sea of Okhotsk region. *Geophysical Journal International*, 203(2):1011–1025.

Patzwahl, R., Mechie, J., Schulze, A., and Giese, P. (1999). Two-dimensional velocity models of the nazca plate subduction zone between 19.5 s and 25 s from wide-angle seismic measurements during the cinca95 project. *Journal of Geophysical Research: Solid Earth*, 104(B4):7293–7317.

Pérez, F. and Granger, B. E. (2007). Ipython: a system for interactive scientific computing. *Computing in Science & Engineering*, 9(3).

Rentsch, S., Buske, S., Lüth, S., and Shapiro, S. (2006). Fast location of seismicity: A migration-type approach with application to hydraulic-fracturing data. *Geophysics*, 72(1):S33–S40.

Reshetnikov, A., Kummerow, J., Asanuma, H., Häring, M., and Shapiro, S. A. (2015). Microseismic reflection imaging and its application to the Basel geothermal reservoir. *Geophysics*, 80(6):WC39–WC49.

Rubin, A. M. and Gillard, D. (2000). Aftershock asymmetry/rupture directivity among central San Andreas fault microearthquakes. *Journal of Geophysical Research: Solid Earth*, 105(B8):19095–19109.

Ruiz, S., Metois, M., Fuenzalida, A., Ruiz, J., Leyton, F., Grandin, R., Vigny, C., Madariaga, R., and Campos, J. (2014). Intense foreshocks and a slow slip event preceded the 2014 Iquique Mw 8.1 earthquake. *Science*, 345(6201):1165–1169.

Saenger, E. H., Gold, N., and Shapiro, S. A. (2000). Modeling the propagation of elastic waves using a modified finite-difference grid. *Wave motion*, 31(1):77–92.

Savage, J. C. (1965). The effect of rupture velocity upon seismic first motions. *Bull. Seism. Soc. Am.*, 55:263–275.

Schurr, B., Asch, G., Hainzl, S., Bedford, J., Hoechner, A., Palo, M., Wang, R., Moreno, M., Bartsch, M., Zhang, Y., et al. (2014). Gradual unlocking of plate boundary controlled initiation of the 2014 Iquique earthquake. *Nature*, 512(7514):299.

Shapiro, S. A., Krüger, O. S., Dinske, C., and Langenbruch, C. (2011). Magnitudes of induced earthquakes and geometric scales of fluid-stimulated rock volumes. *Geophysics*, 76(6):WC55–WC63.

Shi, B. and Brune, J. N. (2005). Characteristics of near-fault ground motions by dynamic thrust faulting: two-dimensional lattice particle approaches. *Bulletin of the Seismological Society of America*, 95(6):2525–2533.

Sippl, C. and Schurr, B. (2017). Anatomy of a subduction zone - seismicity structure of the northern Chilean forearc from >100,000 double-difference relocated earthquake hypocenters. In *EGU General Assembly Conference Abstracts*, volume 19 of *EGU General Assembly Conference Abstracts*, page 5466.

Sippl, C., Schurr, B., Asch, G., and Kummerow, J. (2018). Seismicity structure of the Northern Chile forearc from >100,000 double-difference relocated hypocenters. *Journal of Geophysical Research: Solid Earth*, 123.

Socquet, A., Valdes, J. P., Jara, J., Cotton, F., Walpersdorf, A., Cotte, N., Specht, S., Ortega-Culaciati, F., Carrizo, D., and Norabuena, E. (2017). An 8 month slow slip event triggers progressive nucleation of the 2014 Chile megathrust. *Geophysical Research Letters*, 44(9):4046–4053.

Spudich, P. and Cranswick, E. (1984). Direct observation of rupture propagation during the 1979 imperial valley earthquake using a short baseline accelerometer array. *Bulletin of the Seismological Society of America*, 74(6):2083–2114.

Taira, T., Dreger, D. S., and Nadeau, R. M. (2015). Rupture process for micro-earthquakes inferred from borehole seismic recordings. *International Journal of Earth Sciences*, 104(6):1499–1510.

Tinti, E., Scognamiglio, L., Michelini, A., and Cocco, M. (2016). Slip heterogeneity and directivity of the ML 6.0, 2016, Amatrice earthquake estimated with rapid finite-fault inversion. *Geophysical Research Letters*, 43(20).

Vallée, M. (2004). Stabilizing the Empirical Green Function Analysis: Development of the Projected Landweber Method. *Bulletin of the Seismological Society of America*, 94(2):394–409.

Velasco, A. A., Ammon, C. J., and Lay, T. (1994). Recent large earthquakes near Cape Mendocino and in the Gorda plate: Broadband source time functions, fault orientations, and rupture complexities. *Journal of Geophysical Research: Solid Earth*, 99(B1):711–728.

Walker, K. T. and Shearer, P. M. (2009). Illuminating the near-sonic rupture velocities of the intracontinental Kokoxili Mw 7.8 and Denali fault Mw 7.9 strike-slip earthquakes with global P wave back projection imaging. *Journal of Geophysical Research: Solid Earth*, 114(B2).

Walt, S. v. d., Colbert, S. C., and Varoquaux, G. (2011). The NumPy array: a structure for efficient numerical computation. *Computing in Science & Engineering*, 13(2):22–30.

Weertman, J. (1980). Unstable slippage across a fault that separates elastic media of different elastic constants. *Journal of Geophysical Research: Solid Earth*, 85(B3):1455–1461.

Yamada, T., Mori, J. J., Ide, S., Kawakata, H., Iio, Y., and Ogasawara, H. (2005). Radiation efficiency and apparent stress of small earthquakes in a South African gold mine. *Journal of Geophysical Research: Solid Earth*, 110(B1).

Publications and Conference Abstracts

Folesky, J., Kummerow, J., and Shapiro, S. A. (2015). Microseismic rupture propagation imaging. *Geophysics*, 80(6):WC107–WC115.

Folesky, J., Kummerow, J., Shapiro, S. A., Häring, M., and Asanuma, H. (2016). Rupture directivity of fluid-induced microseismic events: Observations from an enhanced geothermal system. *Journal of Geophysical Research: Solid Earth*, 121(11):8034–8047.

Folesky, J., Kummerow, J., Asch, G., Schurr, B., Sippl, C., Tilmann, F., and Shapiro, S. A. (2018). Estimating Rupture Directions from Local Earthquake Data Using the IPOC Observatory in Northern Chile. *Seismological Research Letters*

Folesky, J., Kummerow, J., and Shapiro, S. (2013). Rupture Propagation Imaging on Microseismic Scale. In *DGG 73. Jahrestagung*, volume 73, pages 291–292, MI–2.004.

Folesky, J., Kummerow, J., and Shapiro, S. (2013). Rupture Propagation Imaging at Microseismic Scale. In *75th EAGE Conference & Exhibition incorporating SPE EUROPEC 2013*.

Folesky, J., Kummerow, J., and Shapiro, S. A. (2014). Rupture Propagation Imaging of Fluid Induced Events at the Basel EGS Project. In *EGU General Assembly Conference Abstracts*, volume 16.

Folesky, J., Kummerow, J., and Shapiro, S. (2014). Rupture Propagation Imaging on Microseismic Scale at the Basel EGS Site. In *DGG 74. Jahrestagung*, volume 74, pages 239, SO–8.0043.

Folesky, J., Kummerow, J., Shapiro, S., Häring, M., and Asanuma, H. (2014). Rupture Propagation Imaging at Microseismic Scale at the Basel EGS Project. In *76th EAGE Conference and Exhibition 2014*.

Folesky, J. and Kummerow, J. (2015). Source Characterization of Microseismic Events using Empirical Green's Functions at the Basel EGS Project. In *EGU General Assembly Conference Abstracts*, volume 17.

Folesky, J. and Kummerow, J. (2015). Source properties of induced microseismic events at the Basel EGS site from Empirical Green's Functions. In *DGG 75. Jahrestagung*, volume 75, pages 316, SO–5.03.

Folesky, J., Kummerow, J., Shapiro, S. A., Häring, M., and Asanuma, H. (2016). Rupture Complexities of Fluid Induced Microseismic Events at the Basel EGS Project. In *EGU General Assembly Conference Abstracts*, volume 18, page 5907.

Folesky, J., Kummerow, J., Shapiro, S., Haering, M., and Asanuma, H. (2016). Rupture Complexities of Fluid Induced Microseismic Events. In *78th EAGE Conference and Exhibition 2016*.

Folesky, J., Kummerow, J., Timann, F., and Shapiro, S. (2017). Estimating Rupture Directivity of Aftershocks of the 2014 Mw8.1 Iquique Earthquake, Northern Chile. In *EGU General Assembly Conference Abstracts*, volume 19, page 15415.

Folesky, J., Kummerow, J., Tilmann, F., and Shapiro, S. A. (2017). Rupture Directivity of Aftershocks of the 2014 Mw8.1 Iquique Earthquake, Northern Chile, using P wave Polarization Analysis. In *DGG 77. Jahrestagung*, volume 77, pages 381, SO.B–107.

Dinske, C., Mueller, M., Voigr, M., Wehner, D., **Folesky, J.**, Kummerow, J., and Shapiro, S. (2018). Rupture Processes and Magnitude Statistics of the 2014 M5.5 Earthquake Sequence Below a Gold Mine in Orkney, South Africa. In *EGU General Assembly Conference Abstracts*, volume 20, page 7211.

Folesky, J., Kummerow, J., and Shapiro, S. (2018). Estimating rupture directivity of local earthquake data in central Italy using P-wave polarity stacking. In *EGU General Assembly Conference Abstracts*, volume 20, page 8747.

Acknowledgements

Danksagung

Einen großen Dank an Prof. S. A. Shapiro für die Begutachtung dieser Arbeit, für die Unterstützung dieses Themas, für die Freiräume und das entgegengbrachte Vertrauen.

Vielen Dank an Prof. F. Tilmann für die unkomplizierte Übernahme des Zweitgutachtens.

Ein besonderer Dank gilt Dr. Jörn Kummerow, der nicht nur Koautor der enthaltenen Publikationen ist, sondern durch seine wissenschafltichen Beiträge und Anleitung viel der hier geleisteten Arbeit überhaupt ermöglicht hat. Danke für dein Engagement und deine Betreuung.

Vielen Dank Wasja, für eine hervorragende Studienzeit und Kumpanei. Danke für deine Tipps, Tricks und Ticks.

Vielen Dank Antonia, Lisa und Rens für die angenehme Gesellschaft der letzen Jahre.

Vielen Dank auch an Stine, Carsten, Olli, Karsten, Cornelius, Aurelian, Nepomuk, Slava, Julio, Florian, Henry, und Ivan für die gemeinsame Zeiten als Kollegen und Kommilitonen.

Ein besonderer Dank geht an meine Eltern und Großeltern und an meine guten Freunde, die das Leben lebenswert machen.

Und schließlich danke ich meiner Jeanne für ihre Unterstützung und Wertschätzung und für die Zukunft.